

---

**Supplementary information**

---

**A wearable cardiac ultrasound imager**

---

In the format provided by the  
authors and unedited

1 **Supplementary Information for**

2  
3  
4 **A wearable cardiac ultrasound imager**

5  
6 Hongjie Hu<sup>1\*</sup>, Hao Huang<sup>1\*</sup>, Mohan Li<sup>2\*</sup>, Xiaoxiang Gao<sup>1\*</sup>, Lu Yin<sup>1</sup>, Ruixiang Qi<sup>3</sup>, Ray S. Wu<sup>1</sup>,  
7 Xiangjun Chen<sup>4</sup>, Yuxiang Ma<sup>1,5</sup>, Keren Shi<sup>4,6</sup>, Chenghai Li<sup>7</sup>, Timothy M. Maus<sup>8</sup>, Brady Huang<sup>9</sup>,  
8 Chengchangfeng Lu<sup>2</sup>, Muyang Lin<sup>1</sup>, Sai Zhou<sup>4</sup>, Zhiyuan Lou<sup>1</sup>, Yue Gu<sup>4,10</sup>, Yimu Chen<sup>1</sup>, Yusheng  
9 Lei<sup>1,11</sup>, Xinyu Wang<sup>1</sup>, Ruotao Wang<sup>1</sup>, Wentong Yue<sup>1</sup>, Xinyi Yang<sup>4</sup>, Yizhou Bian<sup>1</sup>, Jing Mu<sup>4</sup>,  
10 Geonho Park<sup>1</sup>, Shu Xiang<sup>12</sup>, Shengqiang Cai<sup>4,7</sup>, Paul W. Corey<sup>13</sup>, Joseph Wang<sup>1,4</sup>, Sheng  
11 Xu<sup>1,2,4,9,14#</sup>

12  
13 <sup>1</sup>Department of Nanoengineering, University of California San Diego, La Jolla, CA 92093, USA.

14 <sup>2</sup>Department of Electrical and Computer Engineering, University of California San Diego, La Jolla,  
15 CA 92093, USA.

16 <sup>3</sup>Department of Computer Science and Engineering, University of California San Diego, La Jolla,  
17 CA 92093, USA.

18 <sup>4</sup>Materials Science and Engineering Program, University of California San Diego, La Jolla, CA  
19 92093, USA.

20 <sup>5</sup>Department of Mechanical Engineering, Massachusetts Institute of Technology, Cambridge, MA  
21 02139, USA.

22 <sup>6</sup>Materials science and engineering program, University of California Riverside, Riverside, CA  
23 92521, USA.

24 <sup>7</sup>Department of Mechanical and Aerospace Engineering, University of California San Diego, La  
25 Jolla, CA 92093, USA.

26 <sup>8</sup>Department of Anesthesiology, UC San Diego Health-Sulpizio Cardiovascular Center, La Jolla,  
27 CA 92037, USA.

28 <sup>9</sup>Department of Radiology, School of Medicine, University of California San Diego, La Jolla, CA  
29 92103, USA.

30 <sup>10</sup>Department of Neurosurgery, Yale University, New Haven, CT 06520, USA.

31 <sup>11</sup>Department of Chemical Engineering, Stanford University, Stanford, CA 94305, USA.

32 <sup>12</sup>Softsonics, Inc., San Diego, CA 92122, USA.

33 <sup>13</sup>Department of Anesthesiology, Sharp Memorial Hospital, San Diego 92123, CA, USA.

34 <sup>14</sup>Department of Bioengineering, University of California San Diego, La Jolla 92093, CA, USA.

35 \*These authors contributed equally to this work.

36 #Email: shengxu@ucsd.edu

37

38	Content	
39		
40	<b>Supplementary Discussion 1: Significance of the wearable imager</b>	6
41	1.1 End-systolic volume (ESV), end-diastolic volume (EDV), heart rate, stroke volume, cardiac	
42	output, and ejection fraction	6
43	1.2 Cardiac functions and common pathologies	6
44	1.3 B-mode and M-mode images	9
45	1.4 Unique innovation of the wearable imager	9
46	1.5 Bandwidth improvement of the wearable imager	12
47	<b>Supplementary Discussion 2: Why wearable and why ultrasound?</b>	13
48	2.1 Why wearable?	13
49	2.2 General requirements of imaging the heart	15
50	2.3 Magnetic resonance imaging	16
51	2.4 X-ray computed tomography	16
52	2.5 Emission tomography	17
53	2.6 Optical coherence tomography	17
54	2.7 Why ultrasound?	17
55	2.8 Comparability of the wearable ultrasound to clinical ultrasound	18
56	<b>Supplementary Discussion 3: Configuration of the array</b>	20
57	3.1 The configuration of the array in this study	20
58	3.2 The Mills cross array	21
59	3.3 The 1.5D/1.75D array	21
60	<b>Supplementary Discussion 4: Possible sources of electromagnetic interference</b>	22
61	<b>Supplementary Discussion 5: Measurement variations of imaging metrics</b>	22
62	<b>Supplementary Discussion 6: Imaging procedures</b>	23
63	6.1 Imaging from different views	24
64	6.2 Phase correction on nonplanar surfaces	25
65	6.3 Validation for long-term use	28
66	6.4 Simultaneous measurements of M-mode images and electrocardiogram	28
67	<b>Supplementary Discussion 7: Stress echocardiography</b>	29

68	7.1	Significance	29
69	7.2	Limitations of existing procedures	29
70	7.3	Echocardiography by the wearable imager	30
71		<b>Supplementary Discussion 8: Acoustic coupling of wearable imager</b>	31
72		<b>Supplementary Discussion 9: Continuous cardiac performance monitoring</b>	32
73	9.1	Monitoring ejection fraction, cardiac output, and stroke volume simultaneously	32
74	9.2	Monitoring the left ventricular volume by 3D imaging	34
75	9.3	Monitoring the left ventricular volume by 2D imaging	35
76	9.4	Monitoring the left ventricular volume by model estimations	35
77	9.5	Anatomical considerations of imaging posture	41
78		<b>Supplementary Discussion 10: Detailed left ventricle working processes</b>	43
79		<b>Supplementary Discussion 11: Neural network for continuous ultrasound imaging</b>	44
80	11.1	Developing the deep learning model	44
81	11.2	Detailed analysis of the neural network	45
82		<b>Supplementary Fig. 1   Characterization of the transducer array.</b>	50
83		<b>Supplementary Fig. 2   Fabrication processes of the wearable imager.</b>	52
84		<b>Supplementary Fig. 3   Images showing the fabrication resolution of the liquid metal</b>	
85		<b>composite electrodes.</b>	54
86		<b>Supplementary Fig. 4   Mechanical testing of the liquid metal composite electrodes.</b>	55
87		<b>Supplementary Fig. 5   Results of lap shear strength tests.</b>	56
88		<b>Supplementary Fig. 6   Optical images of the multilayered liquid metal composite electrodes.</b>	
89			57
90		<b>Supplementary Fig. 7   The thickness of the SEBS substrate and the printed liquid metal</b>	
91		<b>composite.</b>	58
92		<b>Supplementary Fig. 8   Characterization of noise levels after applying different strategies</b>	
93		<b>sequentially.</b>	59
94		<b>Supplementary Fig. 9   Stress-strain curve of the entire device.</b>	60
95		<b>Supplementary Fig. 10   Biaxial mechanical testing of the entire device.</b>	61
96		<b>Supplementary Fig. 11   The structure of the phantom for device characterizations.</b>	62

97	<b>Supplementary Fig. 12   Characterization of resolutions and acoustic fields with different</b>	
98	<b>transmission methods and angles.</b>	63
99	<b>Supplementary Fig. 13   The mechanism of wide-beam compounding B-mode imaging.</b>	65
100	<b>Supplementary Fig. 14   Signal-to-noise ratio as a function of step size and number of steering</b>	
101	<b>angles of the wide-beam compounding imaging.</b>	66
102	<b>Supplementary Fig. 15   The flow chart of receive beamforming.</b>	67
103	<b>Supplementary Fig. 16   Gray scale B-mode images of phantoms and selected windows for</b>	
104	<b>calculating the dynamic range.</b>	68
105	<b>Supplementary Fig. 17   Detailed comparison of the imaging metrics between the wearable</b>	
106	<b>and the commercial imagers.</b>	69
107	<b>Supplementary Fig. 18   Schematic experimental setups of resolution tests.</b>	70
108	<b>Supplementary Fig. 19   Processes of evaluating the surface curvature for phase correction.</b>	
109		72
110	<b>Supplementary Fig. 20   B-mode images collected with different couplants.</b>	74
111	<b>Supplementary Fig. 21   Quantitatively evaluation of different coupling conditions.</b>	75
112	<b>Supplementary Fig. 22   Optical images of attaching the wearable imager to the chest for</b>	
113	<b>long-term.</b>	76
114	<b>Supplementary Fig. 23   Continuous surface temperature and heart rate monitoring for 1</b>	
115	<b>hour.</b>	77
116	<b>Supplementary Fig. 24   Images of the parasternal long axis view from 10 subjects using a</b>	
117	<b>recycled device.</b>	78
118	<b>Supplementary Fig. 25   The structure of the FCN-32 neural network.</b>	79
119	<b>Supplementary Fig. 26   The comparison of the intersection over union among different</b>	
120	<b>models used in this study.</b>	81
121	<b>Supplementary Fig. 27   The types and results of data augmentation.</b>	83
122	<b>Supplementary Fig. 28   Imaging from apical four chamber view with different positions.</b>	84
123	<b>Supplementary Fig. 29   Validation of the image imputation algorithm.</b>	86
124	<b>Supplementary Fig. 30   B-mode images of the abdominal area and liver from the wearable</b>	
125	<b>and the commercial imagers.</b>	87
126	<b>Supplementary Fig. 31   B-mode images of biopsy tests on a commercial phantom (CIRS 052).</b>	
127		88

128	<b>Supplementary Fig. 32   B-mode images of cardiac anatomies tested by an experienced cardiac sonographer.</b>	89
129		
130	<b>Supplementary Fig. 33   Photograph and schematics of the imaging system.</b>	90
131	<b>Supplementary Fig. 34   Configuration of a Mills cross array.</b>	92
132	<b>Supplementary Table 1   Summary of existing imaging methods for the heart.</b>	93
133	<b>Supplementary Table 2   Comparison between the bonding strength of the liquid metal electrode, pure SEBS, and commercial adhesives.</b>	94
134		
135	<b>Supplementary Table 3   Model parameters and code availability.</b>	95
136	<b>Supplementary Table 4   Sample sizes for all models.</b>	96
137	<b>Supplementary Table 5   Mean Intersection over Union among different models.</b>	97
138	<b>Supplementary Video 1. Cardiac long and short axis views imaged by an orthogonal array.</b>	98
139		
140	<b>Supplementary Video 2. Cardiac apical four- and two- chamber views imaged by an orthogonal array.</b>	98
141		
142	<b>Supplementary Video 3. Continuous cardiac imaging during rest, exercise, and recovery.</b>	98
143	<b>Supplementary Video 4. Left ventricle segmentation results by FCN-32.</b>	98
144	<b>Supplementary Video 5. Imaging guided biopsy on a phantom by an orthogonal array.</b>	98
145	<b>References</b>	99
146		

147 **Supplementary Discussion 1: Significance of the wearable imager**

148

149 1.1 End-systolic volume (ESV), end-diastolic volume (EDV), heart rate, stroke volume, cardiac  
150 output, and ejection fraction

151 Normal cardiac function is essential for maintaining systemic tissue perfusion throughout the  
152 body<sup>1</sup>. Cardiovascular diseases, especially in the elderly, impose a huge burden in terms of  
153 mortality, morbidity, disability, and healthcare costs<sup>2</sup>. More than a million patients are admitted  
154 annually to U.S. hospitals with acute heart failure alone, together with a high median percentage  
155 of intensive care unit admission of 10%<sup>68</sup> and a high in-hospital mortality rate of around 4% to  
156 7%<sup>69</sup>. Also, cardiovascular failure is one of the leading causes of death in intensive care units<sup>70</sup>  
157 and nearly one-quarter of all deaths in intensive care units are attributed to it.

158

159 Accurate assessment of subtle changes in cardiac functions is essential for health management  
160 and disease prevention for healthy people, as well as diagnosis of pathogenesis and interventions  
161 for patients. The signals we can use to evaluate the cardiac functions include the ESV, EDV, heart  
162 rate, as well as their derivative signals such as stroke volume, cardiac output, and ejection fraction.  
163 ESV and EDV can be obtained by processing the apical four-chamber view B-mode images using  
164 a deep learning model. The heart rate can be observed based on the period of contraction in M-  
165 mode images. Based on these values, those derivative signals can be calculated by:

166

$$167 \quad \textit{Stroke volume} = \textit{EDV} - \textit{ESV} \quad (10)$$

168

$$169 \quad \textit{Cardiac output} = \textit{Stroke volume} * \textit{Heart rate} \quad (11)$$

170

$$171 \quad \textit{Ejection fraction} = \frac{\textit{Stroke volume}}{\textit{EDV}} \quad (12)$$

172

173 Stroke volume indicates the absolute blood volume the left ventricle can pump out in a single  
174 stroke. The cardiac output indicates the absolute blood volume the left ventricle can pump out  
175 every minute. Ejection fraction indicates the relative fraction of the blood in the left ventricle that  
176 the heart can pump out in a single stroke. Altogether, these indices provide insight into the  
177 capability of the heart to deliver blood to tissues throughout the body.

178

179 1.2 Cardiac functions and common pathologies

180 Cells in the human body all require a steady supply of oxygen and nutrient for their  
181 metabolism. The cellular metabolic rates are not static, but rather are subject to constant  
182 fluctuations. Thus, the heart must not only be able to produce a cardiac output meeting the  
183 metabolic demands of the body at a given time but also do so efficiently, such that enough  
184 headroom is maintained to accommodate any heightened metabolic rates that can occur due to

185 circumstances such as strenuous exercise. The existence of a nonzero end-systolic volume itself  
186 also serves a similar purpose as a buffer<sup>37</sup>. Thus, the occurrence of heart failure is marked either  
187 by an inability of the heart to provide a cardiac output meeting the metabolic demands of the body,  
188 and/or a compromised efficiency in function and consequent lack of headroom<sup>38</sup>.

189

190 There are two forms of heart failure: systolic and diastolic. As the names suggest, systolic  
191 heart failure results from the heart's lack of ability to pump blood during systole, while diastolic  
192 heart failure results from the heart's lack of ability to fill with blood during diastole.

193

194 During systole, the goal of the left ventricle is to eject as much of its blood volume as possible.  
195 The ability of the left ventricle to do so can be viewed as a function of three factors: (a) the  
196 contractility of the myocardium, (b) the afterload in the left ventricle, and (c) the structural integrity  
197 of the left ventricle<sup>38</sup>.

198 (a) The contractility acts as the driving force for blood flow out of the left ventricle and  
199 through the aortic valve. If the contractility is compromised, the left ventricle's capacity  
200 to eject blood will be reduced. This can occur due to conditions such as dilated  
201 cardiomyopathy or ischemic heart disease, which cause the myocardium to contract  
202 weakly. Alternatively, it can be a result of pathologies such as arrhythmia, in which the  
203 myocardium activates asynchronously rather than produces a single, strong impulse during  
204 systole.

205

206 (b) Afterload is the amount of resistance encountered by the left ventricle as it attempts to  
207 contract. The more resistance the left ventricle encounters, the more difficult it will be to  
208 eject blood. This can result from conditions such as aortic stenosis, where the aortic valve  
209 does not open fully and restricts the blood flow, or hypertension, in which there is elevated  
210 pressure in the left ventricle resisting contraction.

211

212 (c) The structural integrity of the left ventricle is a prerequisite for its functions. For example,  
213 a mitral valve defect that results in an improper seal between the left ventricle and left  
214 atrium can cause blood to backflow into the left atrium during systole, instead of flowing  
215 through the aortic valve towards the rest of the body.

216

217 During diastole, the goal of the left ventricle is to fill with as much blood as possible. This  
218 ensures that there is enough blood available to be pumped out afterwards, during systole. Similar  
219 to systole, the diastolic function can also be broken down into three contributing factors<sup>38</sup>: (a) the  
220 distensibility of the left ventricle, (b) external compression, and (c) structural factors.

221

222 (a) In diastole, the distensibility of the left ventricle serves as the driving force, allowing it to  
223 expand and be filled with blood. A stiffer or thicker myocardium loses its ability to expand,



224 resulting in decreased distensibility. For example, the protein deposits caused by  
225 amyloidosis can lead to this effect. Hypertrophy can also be caused by chronic  
226 hypertension as a result of the heart working against high afterloads<sup>71</sup>. Gradual loss of  
227 distensibility is also a natural result of aging<sup>72</sup>.

228  
229 (b) External compression acts as the resistive force against the distensibility of the left  
230 ventricle. External compression restricts the volume of blood that can be filled, leading to  
231 diastolic heart failure. External compression is introduced from regions external to the left  
232 ventricle, such as the pericardium in constrictive pericarditis and cardiac tamponade. It  
233 can even come from the right ventricle, as is the case in cor pulmonale, in which right  
234 ventricular failure has excessive volume. This dilation of the right ventricle creates an  
235 external compression acting on the left ventricle.

236  
237 (c) Structural factors can also affect diastole, in the form of obstructions to filling.  
238 Obstructions prevent the left ventricle from filling optimally during diastole, leading to a  
239 reduction of the end-diastolic volume. For example, mitral stenosis can prevent the mitral  
240 valve from opening optimally, reducing blood flow into the left ventricle from the left  
241 atrium. A left atrial myxoma located in the way of the mitral valve could also cause a  
242 similar effect.

243  
244 Additionally, diastolic heart failure can also result from systolic heart failure. When the  
245 ejection fraction decreases due to systolic heart failure, causing an initial drop in stroke volume  
246 and cardiac output, the heart may compensate by increasing the end-diastolic volume with higher  
247 filling pressure through neurohormonal pathways that increase the vascular tone and intravascular  
248 volume<sup>37,38</sup>. This invokes the Frank-Starling relationship<sup>73</sup> by creating a higher pre-load, allowing  
249 the stroke volume to return back to normal levels while the ejection fraction remains low. Because  
250 diastolic filling must occur with elevated pressure if the cardiac output is to be maintained, diastolic  
251 heart failure can happen in this situation. As with nearly all human physiology, this is one of many  
252 examples showing how the final indices that we observe are often the result of a long cascade of  
253 interactions.

254  
255 As such, the numerical indices (i.e., ESV, EDV, heart rate, stroke volume, cardiac output, and  
256 ejection fraction) by themselves can only point us towards whether systolic/diastolic heart failure  
257 has occurred, or possibly both have occurred. For example, in systolic heart failure, one cannot  
258 determine whether it stems from a lack of contractility, increased afterload, or loss of structural  
259 integrity, based on the numbers alone. Therefore, while these indices may not provide a specific  
260 diagnosis, they serve as highly efficient quantitative indicators for the early detection of a broad  
261 range of cardiovascular diseases. The ability to continuously monitor these indices opens the  
262 opportunity for more comprehensive examinations to be performed in a timely manner.

263

### 264 1.3 B-mode and M-mode images

265 In this study, we demonstrate direct ultrasound B-mode and M-mode imaging of cardiac  
266 structures. This capability of the wearable imager is valuable in providing a more detailed  
267 diagnosis after an initial indication of cardiovascular diseases from the numerical indices. A vast  
268 number of factors contributing to heart failure can be identified visually just from imaging the  
269 heart continuously. For example, ischemia may result in the death of myocardial cells, producing  
270 effects such as fibrillation and hypokinesia/akinesia, which can be easily observed in continuously  
271 recorded images. Features related to the structural integrity of the heart and obstructions to filling  
272 may also be seen, such as valvular stenosis, valvular regurgitation, septal defects, and left atrial  
273 myxoma. Hypertrophic cardiomyopathy can result in an obvious thickening of the myocardium  
274 that can be seen on the ultrasound recording, while dilated cardiomyopathy results in a visible  
275 thinning of the myocardium and dilation of the left ventricle. Hypertrophic cardiomyopathy can  
276 also be differentiated from pathologies like amyloidosis due to the extreme brightness of the  
277 amyloid proteins relative to the myocardium on the ultrasound image. These are a few notable  
278 examples of the vast range of diseases that can be diagnosed conclusively through wearable  
279 imaging.

280

281 In this study, four standard B-mode ultrasound views of the heart were implemented:  
282 parasternal long axis, parasternal short axis, apical four-chamber, and apical two-chamber.  
283 Parasternal long and short axis views are orthogonal, so are apical four- and two-chamber views.  
284 Each of these views provides a different perspective of the heart, with its own viewing angle and  
285 set of structures, allowing for the most comprehensive heart investigations. In addition, imaging  
286 the heart from these standard views allows for a more accurate representation of cardiac structural  
287 dimensions. Imaging from other angles can also reveal internal structures, but the displayed  
288 dimensions may have deviations from what clinicians normally measure. From the four views, the  
289 symptoms related to major abnormalities in cardiac functions such as changes in myocardial  
290 thickness, can be easily and accurately observed. Furthermore, diseases and activities may increase  
291 the heart rate, leading to faster valvular velocities, which could be quantitatively estimated through  
292 a frame-by-frame observation method: the distance of the valve movement can be detected from  
293 frames in B-mode images. A faster valvular velocity leads to fewer frames to reach the same  
294 distance.

295

### 296 1.4 Unique innovation of the wearable imager

297 Emerging wearable electronics in recent years have gradually transformed ultrasound  
298 technologies from traditional large-scale equipment to miniaturized wearable devices. Wearable  
299 ultrasound devices have been demonstrated for other applications, including monitoring of blood  
300 pressure, blood flow, and tissue motions (Extended Data Table 1), continuous in-motion analytical  
301 B-mode imaging of deep tissues, a major aspiration for diagnostic ultrasound, has not been

302 achieved<sup>18,19,26,28,32,47,48,74-83</sup>. Recently continuous B-mode imaging on various tissues of the human  
303 body was reported based on a rigid ultrasound device<sup>25</sup>. The authors used a soft adhesive material  
304 to fix the rigid ultrasound device on the human body and acquired only snapshots of the heart when  
305 the subject was in-motion. Moreover, there was a lack of analysis of these acquired images. The  
306 data from wearable devices are only valuable when we can extract actionable information from  
307 them.

308  
309 In this work, the ultrasound device is soft and can collect high-quality cardiac images during  
310 exercise continuously. We reconstructed the B-mode images of phantoms and various tissues (e.g.,  
311 liver, abdominal aorta, inferior vena cava, and biopsy process, as seen in Supplementary Figs. 30  
312 and 31) with a particular focus on the heart. Because the heart has a complex and fast-moving  
313 anatomical structure, continuous cardiac imaging can provide new opportunities of understanding  
314 pathologies of many cardiovascular diseases. We showed bi-planar imaging from multiple  
315 standard views commonly used in transthoracic echocardiography examinations. We quantified  
316 the displacement of myocardium for the diagnosis of myocardial ischemia. We also used a deep  
317 learning model to extract key cardiac metrics such as stroke volume, ejection fraction, and cardiac  
318 output from the continuous images automatically. These contributions have never been made by  
319 any wearable devices. The novelty of this work is two-fold.

320  
321 (1) Innovation in device engineering, including array design, microfabrication, and  
322 transmitting strategy

323  
324 First, we used 32 elements in each row of transducers with a pitch of 0.4 mm (shorter than one  
325 ultrasound wavelength), which considerably enhanced the signal-to-noise ratio and weakened  
326 grating-lobes, leading to better spatial resolutions, stronger penetration capabilities, and less  
327 artifacts compared to existing wearable phased array images.

328  
329 Second, to achieve such a large size and small pitch of the array, new microfabrication  
330 techniques were required. We replaced the conventional serpentine-based copper electrodes with  
331 straight liquid metal electrodes that were inherently stretchable, and micropatterned the traces with  
332 screen printing and laser ablation, which significantly increased the pattern resolution, with a  
333 minimum width and kerf of 0.03 mm and 0.025 mm, respectively. Such a high pattern resolution  
334 enables stretchable electronics with high-density. Additionally, we replaced the manual alignment  
335 of hundreds of elements with a new automatic alignment method, which was more time-efficient  
336 and had a higher success rate. Moreover, we applied a room-temperature bonding method and  
337 made a dense backing layer to enhance the acoustic performance of each ultrasonic transducer in  
338 the array.

339

340 Third, for the packaging strategy, in previous work, we used a type of silicone elastomer  
341 (Ecoflex-0030) as the substrate and superstrate, which provided mechanical support and  
342 waterproof encapsulation to the device<sup>18,19</sup>. In this work, we used a triblock copolymer (SEBS)  
343 coated by liquid metal as the substrate and superstrate. This did not only provide mechanical  
344 support and waterproof encapsulation, but also serves as the ground electrode and the shielding  
345 layer to screen any interference from ambient electromagnetic waves that might otherwise induce  
346 imaging artifacts.

347  
348 Specifically, to apply the SEBS as the encapsulation material, we have tried a variety of  
349 polymers and many ways of coating liquid-metal. Liquid metal has a large surface tension and  
350 does not easily wet the polymer substrate. We solved this problem by mixing SEBS, dissolved in  
351 toluene solution, with liquid metal to form a composite electrode, which could readily wet and  
352 adhere to the SEBS substrate. Silicone elastomers did not work because they cannot be dissolved  
353 by common solvents so they failed to composite with the liquid metal. This new packaging strategy  
354 enables more functions and use cases and has never been realized in any reported wearable  
355 ultrasonic devices.

356  
357 Fourth, an advanced wide-beam compounding transmission method was introduced to  
358 wearable ultrasonic technologies for the first time. Compared with other traditional transmission  
359 approaches, such as single plane-wave and mono-focus, the wide-beam compounding method  
360 provides B-mode images with enhanced spatial resolutions, signal-to-noise ratios, and contrast-to-  
361 noise ratios<sup>27</sup>.

362  
363 Based on the above innovations in device engineering, we realized high-quality B-mode  
364 ultrasound imaging using a wearable ultrasonic patch. High-quality B-mode imaging-guided  
365 applications and techniques, such as Doppler-based imaging<sup>84</sup>, elastography<sup>85</sup>, 3D/4D imaging<sup>86</sup>,  
366 ultrafast/super-resolution imaging<sup>87,88</sup>, and ultrasound stimulation<sup>89</sup>, can all be possible on the  
367 wearable platform.

368  
369 (2) Continuous cardiac imaging during exercise and associated automatic data processing by  
370 deep learning

371  
372 Conventionally, cardiac imaging is carried out using bulky expensive equipment while the  
373 subject stays still. Existing wearable health devices allow monitoring the human body on the go  
374 but can only capture signals on the skin surface and generate signals in the form of data points and  
375 curves. Wearable imaging of central organs (e.g., the heart) remains a grand challenge in the field.  
376 Particularly, the heart is relatively difficult to image due to its complex and fast-moving anatomical  
377 structure and large depth from the skin.

378

379 In this study, we demonstrated continuous cardiac imaging with qualities comparable to those  
380 from a commercial ultrasound probe. The innovation of this application is two-fold.

381  
382 First, traditional stress echocardiography can only image the heart after exercise. Wearable  
383 cardiac imaging allows capturing the heart anatomy and performance before, during, and promptly  
384 after exercise continuously in real time. This technology enables evaluating cardiac abnormalities  
385 that are only present under stress, opening up new diagnostic possibilities with information that  
386 previously could not be acquired.

387  
388 Second, conventionally, measuring cardiac indices such as stroke volume, cardiac output, and  
389 ejection fraction usually requires cardiologists to contour the boundary of the left ventricle  
390 manually, which is very time-consuming and operator-dependent. They typically collect only one  
391 representative cardiac cycle to evaluate those parameters<sup>3</sup>, giving only discrete data. Although  
392 some research studies<sup>3,90</sup> and commercial systems<sup>91</sup> developed algorithms to derive these indices  
393 over multiple cardiac cycles, it still requires cardiologists to operate the imaging probe manually.  
394 Long-term continuous cardiac imaging by integrating the wearable ultrasound patch with deep-  
395 learning based image-processing can derive waveforms of these indices automatically, with an  
396 unprecedented high temporal resolution.

397  
398 In summary, the innovations in device engineering and automated image processing allow the  
399 wearable ultrasonic patch to perform long-term continuous cardiac imaging from multiple views  
400 during exercise. The output waveforms of cardiac indices such as cardiac output, stroke volume,  
401 and ejection fraction have never been achieved by existing wearables.

#### 402 403 1.5 Bandwidth improvement of the wearable imager

404 The 55% transducer bandwidth is not as high as that of the commercial P4-2v imager (~74%  
405 bandwidth). In contrast to the rigid ultrasound probe, which has a very thick backing layer to  
406 effectively attenuate the reverberation, the wearable ultrasonic patch cannot be assembled with  
407 such a thick backing layer because it would severely impair the mechanical compliance of the  
408 device, preventing it from intimately conforming and coupling to the human skin. Therefore, the  
409 current design of a thin yet dense backing layer is a compromise between reducing reverberation  
410 and maintaining outstanding mechanical compliance of the device.

411  
412 To quantify the efficacy of the thin yet dense backing layer in this study, we performed pulse-  
413 echo testing of an element without the backing layer. The frequency spectrum and its -6 dB  
414 bandwidth are derived (Supplementary Fig. 1). The results show that the backing layer in this study  
415 improved the bandwidth by almost 25%.

416

417 In future work, we will develop new composites for backing layers<sup>92,93</sup>. Specifically, we will  
418 incorporate glass bubbles and tungsten powders into the polyimide resin. By tuning the proportion  
419 of the three components, we can synthesize a composite with a small thickness, an appropriate  
420 acoustic impedance, and a high attenuation coefficient that is five times higher than the current  
421 material<sup>93</sup>. This new composite will allow the wearable ultrasound probe to have both high  
422 bandwidth and skin-like mechanical properties.

423

## 424 **Supplementary Discussion 2: Why wearable and why ultrasound?**

425

### 426 2.1 Why wearable?

427 Not all diseases have regular and sustained symptoms or pathologies. Continuous monitoring  
428 over a long period is essential for providing reliable and accurate diagnosis<sup>3,4</sup>. The insufficient  
429 sampling of signals would possibly miss transient but critical signals and thus provide less  
430 confidence to the diagnostic results. Thus, long-term monitoring is highly desired for those that  
431 are sporadic and barely predictable. However, conventional methods to continuously monitor the  
432 heart are invasive or semi-invasive, which are resource intensive and limit their use in bedside  
433 surveillance for critically ill or surgery patients<sup>94,95</sup>. Invasive methods may require anesthesia that  
434 could influence the measurement results<sup>96,97</sup>. Their invasive nature is also associated with risk of  
435 morbidity and mortality<sup>94</sup>. Emerging wearable technologies address these challenges by enabling  
436 long-term monitoring noninvasively.

437

438 Besides stress echocardiography demonstrated in this work, there are several other use cases  
439 that can benefit from wearable long-term monitoring.

440

441 Sinus arrhythmia produced by the irregular release of impulses from the sinoatrial node is one  
442 typical example<sup>98</sup>. Being prevalent among senior people<sup>99</sup>, arrhythmia is the root cause of a variety  
443 of other symptoms and diseases, such as blood clotting in the heart, hypotension that leads to  
444 dizziness, and sudden death. Sinus arrhythmia includes sinus tachycardia, bradycardia, and  
445 arrest<sup>100</sup>. Sinus arrhythmias may not have symptoms during the limited examination time because  
446 it could be sporadic and barely predictable in daily life<sup>101</sup>. Hence, prolonged tracking time can help  
447 record the timing and syndromes for a better diagnosis. Also, while it is simple to detect symptoms  
448 with a quick test, it is imprudent to instantly diagnose signs as illness and intervene immediately.  
449 This is because sinus rhythm is very sensitive to factors such as mood and respiration, and after a  
450 while the variations automatically revert to normal<sup>98</sup>. Existing approaches for monitoring  
451 arrhythmia are plagued by various problems. Auscultation of the heartbeat with a stethoscope is a  
452 general but nonspecific measurement, because abnormality like premature or abnormal beats do not  
453 always produce an audible pumping and may be missed and misdiagnosed<sup>102</sup>. An  
454 electrocardiogram could be more effective and accurate. It provides abundant information because  
455 different types of arrhythmias have different reflections on electrocardiograms. Doctors can tell

456 the type from an electrocardiogram directly and thus more quickly make a move. But motion  
457 artifacts introduced by body movement will distort electrocardiogram signals badly, which  
458 challenges signal accuracy in daily monitoring<sup>103</sup>. Additionally, the lack of structural information  
459 prevents electrocardiograms from providing a comprehensive diagnosis. Photoplethysmography  
460 fails to provide sufficient information for further diagnosing the type of arrhythmia<sup>104</sup>, because it  
461 can only monitor the heart rate. There are some studies on building mathematical models to  
462 correlate photoplethysmography waveforms to the arrhythmia type, but the result is not accurate  
463 enough<sup>105</sup>. Other invasive methods may be less commonly used<sup>106</sup>.

464  
465 Another example is paroxysmal atrial fibrillation, which intermittently occurs as a disorder of  
466 cardiac rhythm<sup>107</sup>. This disease also suffers from the same problem that limited examination time  
467 may not be enough for a thorough diagnosis, and this could introduce horrible results. Paroxysmal  
468 atrial fibrillation may develop into chronic atrial fibrillation, which occurs more frequently, a direct  
469 result of misdiagnosis. Moreover, a common error in clinical management of atrial fibrillation is  
470 to treat chronic sustained atrial fibrillation and paroxysmal atrial fibrillation similarly, despite  
471 some differences in management objectives<sup>107</sup>. Atrial fibrillation is often associated with a high  
472 risk of morbidity and mortality from heart failure, stroke, and thromboembolic complications<sup>107,108</sup>.  
473 Thus, the failure of detecting the early stage of paroxysmal atrial fibrillation is disastrous.

474  
475 Similarly, coronary heart disease may also be undetectable in a transient test. Coronary heart  
476 disease is caused by plaque built-up near the coronary arteries, which limits the blood supply<sup>109</sup>.  
477 Coronary heart disease often develops over decades and is frequently ignored because no  
478 symptoms are detected. However, the unnoticed coronary heart disease could lead to an acute heart  
479 attack due to the blockage of the artery, which is extremely lethal and results in a high mortality<sup>109</sup>.  
480 This heart attack caused by undetected coronary heart disease with no obvious symptoms may also  
481 be called a “silent heart attack”. Silent precursors to an imminent myocardial infarction can be  
482 detected by observing segmental wall motion abnormalities in ultrasound images.

483  
484 Finally, acute heart disease could barely be noticed when it is not occurring. Myocardial  
485 infarction is the lack of blood supply to the myocardium, which weakens cardiac activities<sup>110</sup>.  
486 Myocardial infarction has a high morbidity because many factors and triggers contribute to it, such  
487 as alcohol, physical exertion, and obesity. Myocardial infarction also has a high mortality. It cannot  
488 be effectively detected in current measuring procedures, because the short period of testing time  
489 cannot capture any signs of it unless it is occurring with symptoms.

490  
491 We can summarize that previous efforts of wearable devices for non-invasive heart monitoring  
492 are mainly categorized into three fields: electrical probe, electromagnetic probe, and mechanical  
493 probe<sup>51</sup>. Specifically, the electrocardiogram sensor for local-field potential recording for analyzing  
494 cardiac rhythm<sup>12,111</sup>; the electrical impedance tomography sensor based on internal electrical

495 conductivity mapping mainly for distinguishing systole and diastole phases<sup>16</sup>; the electromagnetic  
496 sensor that measures stroke volume by relating the resonant frequency response of the sensor to  
497 permittivity changes caused by blood volume<sup>112</sup>; the passive vibration sensor based on mechanical  
498 waves usually designed for monitoring the heart rate<sup>113</sup>. However, those signals either are indirect  
499 or suffer from low spatial resolutions, from which many clinically important cardiac  
500 characteristics, such as the volume of heart chambers, the myocardium structure, and the  
501 ventricular ejection function, cannot be visually and accurately evaluated<sup>114</sup>.

502

## 503 2.2 General requirements of imaging the heart

504 Echocardiography, as one of the most flexible diagnostic tools revealing the structural  
505 information of the heart, is widely adopted in hospitals<sup>115</sup>. However, current echocardiography  
506 focuses on short-term recordings of the heart to make a diagnosis, but transient symptoms or  
507 dysfunctions may not appear during the limited time of such recordings. Other methods based on  
508 imaging can barely provide reliable and thorough monitoring of cardiac functions, including  
509 magnetic resonance imaging<sup>116</sup>, computed tomography<sup>117</sup>, single-photon emission computed  
510 tomography<sup>118</sup>, positron emission tomography<sup>119</sup>, and optical coherence tomography<sup>120</sup>. Here we  
511 briefly outline the pros and cons of each method's working principles and the rationale behind  
512 selecting the ultrasound platform in this study (Supplementary Table 1). We desire a device that  
513 is wearable, can target the heart, and is capable of 2D or 3D imaging with a high spatial resolution  
514 and sufficient contrast. These requirements can be summed up in a single term: wearable heart  
515 imaging, which entails the following needs.

516

517 For a modality to be suitable in wearable devices, it must first be able to be packaged into a  
518 small, lightweight, and minimal form factor that is both comfortable and non-invasive. The device  
519 must ideally provide zero hindrance to the wearer, such that there is a negligible impact on their  
520 comfort or normal activities when wearing it. A sufficient penetration depth is required to target  
521 the heart non-invasively. Furthermore, the chosen modality must be robust, with no degradation  
522 in the image quality over time or large variances in image quality under different conditions  
523 encountered in daily life. Wearable devices are often desired to perform long-term monitoring, and  
524 to be frequently removed and reapplied to the wearer. Therefore, the device must also withstand  
525 the wear and tear of long-term use without a loss in image quality over time. Most importantly,  
526 the device must be safe for indefinite use—for example, the modality should not be based on  
527 ionizing radiation.

528

529 For a modality to target the heart, the major challenge to overcome is the high temporal  
530 resolution required. The heart may beat at rates of anywhere from 50 beats per minute at rest<sup>121</sup> to  
531 nearly 200 beats per minute during exercise<sup>122</sup>, and as such, requires a modality that can achieve  
532 temporal resolutions of at least 33 ms<sup>5,123</sup> to image continuously in real-time. Modalities that lack



533 sufficient temporal resolutions can result in the lack of critical diagnostic information, as well as  
534 degradation of image quality due to motion artifacts.

535

536 Lastly, to make a device useful for performing a wide range of general examinations, the  
537 modality must be able to image in 2D or 3D with high spatial resolutions and good contrast. Most  
538 of the work on wearable devices has primarily targeted measures such as pulse acquisition and  
539 blood oxygen levels. While these are helpful signals, they cannot compare to the immense  
540 diagnostic value that direct 2D or 3D imaging of the heart provides. Imaging provides a great  
541 wealth of information, but its quality is crucial to being able to make these diagnoses. Poor image  
542 quality may often obscure key indicators of diseases, lead to false positives, or make it difficult to  
543 distinguish between different conditions.

544

545 Therefore, to summarize, the ideal modality should be robust, safe for long-term use, easily  
546 scaled down to wearable and portable form factors, imaging in 2D or 3D with high spatial/temporal  
547 resolutions, having a sufficient penetration depth to target the heart non-invasively, having a  
548 sufficient contrast, and having a high signal-to-noise ratio. However, it should be noted that some  
549 of these requirements have trade-offs. For example, by nature, imaging at high spatial resolutions  
550 will tend to sacrifice the temporal resolution, due to the larger amount of data being acquired and  
551 processed. Therefore, we can only select the most suitable modality that is able to balance all  
552 factors while meeting sufficient requirements.

553

### 554 2.3 Magnetic resonance imaging

555 Magnetic resonance imaging works by using a powerful magnetic field to align the protons in  
556 the body's tissues with the field. Radiofrequency waves are then pulsed to disturb this alignment,  
557 followed by a subsequent release of secondary radio waves when the protons realign with the field.  
558 These signals are collected to form images<sup>124</sup>. Magnetic resonance imaging provides high tissue  
559 contrast and image quality in real-time with spatial and temporal resolutions in the range of 1.6  
560 mm and 13-50 ms<sup>5,125</sup>, respectively. In addition, it is non-ionizing because it uses a magnetic field  
561 and radiofrequency waves. However, magnetic resonance imaging has several obvious drawbacks  
562 that make it unsuitable for needs in this study. First, magnetic resonance imaging machines are  
563 extremely bulky and expensive and are not scalable to wearable form factors. Furthermore, the  
564 powerful magnetic field is an intrinsic requirement of the modality and can easily present a  
565 significant hazard in everyday life in addition to being incompatible with devices like pacemakers  
566 that are likely to be used by the target demographics in this study.

567

### 568 2.4 X-ray computed tomography

569 A computed tomography scanner consists of an X-ray source and a detector placed opposite  
570 of each other, which rotate around the subject to capture several images from multiple angles. The  
571 images are then used to reconstruct a 3D image of the subject<sup>126</sup>. Although computed tomography

572 is relatively low cost and provides high spatial resolutions of around 0.3 mm<sup>6</sup>, the scanner contains  
573 many moving parts. This type of moving design is not suitable for wearable devices, and the  
574 physical constraint puts a strict limitation on the temporal resolution (~66 ms<sup>6,127</sup>) that makes it  
575 unsuitable for real-time cardiac imaging. Furthermore, the ionizing X-ray radiation makes it  
576 fundamentally unsafe for long-term wearing.

577

## 578 2.5 Emission tomography

579 Single-photon emission computed tomography and positron emission tomography make use  
580 of radiotracers injected into the body that radioactively decay over time as they travel through the  
581 body following their designated molecular targets. These signals can then be collected using a  
582 gamma camera to quantify those molecular targets and metabolic events<sup>128-130</sup>. This allows  
583 gathering unique types of information such as myocardial perfusion and cell metabolic activities<sup>129</sup>.  
584 In addition, positron emission tomography's temporal resolution is too slow (>2000 ms<sup>131</sup>) for  
585 cardiac imaging, while single-photon emission computed tomography's poor image resolution  
586 (~10 mm<sup>132</sup>) makes it largely impractical for more general diagnostic imaging. There is also a very  
587 low signal-to-noise ratio in these modalities<sup>130</sup>. Subjects are exposed to low levels of ionizing  
588 gamma radiation, and the tracers must be replenished over time as they decay, making these  
589 modalities unsuitable for wearable devices.

590

## 591 2.6 Optical coherence tomography

592 Optical coherence tomography uses light scattering within the 700-900 nm wavelength range,  
593 also known as the "therapeutic window", to image the human tissue<sup>8</sup>. These wavelengths have low  
594 absorbance and high scattering in tissues on top of being non-ionizing, making them useful for  
595 imaging tissues. In constructing the image, the time delay cannot be used to determine the location  
596 of the scattered signals because the speed of light is too fast. Thus, interferometry is used instead,  
597 in which the primary beam of light is split in half to target the tissue and a mirror simultaneously.  
598 As the distance of the mirror is varied, constructive interference occurs with signals coming from  
599 different locations within the tissue, allowing the position of the signals to be distinguished. Due  
600 to the short optical wavelength, optical coherence tomography can achieve extremely high spatial  
601 resolutions of up to 1 μm<sup>8</sup>, and temporal resolutions of 2 ms<sup>8</sup>. In addition, dyes can be injected  
602 into the subject to add additional capabilities to optical coherence tomography. For example, the  
603 use of voltage-reactive dyes can make it possible to form activation and conduction velocity vector  
604 maps of the myocardium using optical coherence tomography<sup>8</sup>. Despite these advantages, optical  
605 coherence tomography is unsuitable due to the bulky optics required, and limited tissue penetration  
606 depth of 2-3 mm<sup>8</sup>.

607

## 608 2.7 Why ultrasound?

609 Lastly, we look at the rationale for selecting the ultrasound modality in this study.  
610 Piezoelectric transducers generate ultrasound waves throughout the tissue. The same transducers

611 can then collect the backscattered signals and construct an image based on their strength and time  
612 delay at each pixel<sup>27,133,134</sup>. This “all-in-one” capability of ultrasound allows the device to become  
613 extremely compact and easily scaled down to wearable form factors<sup>26</sup>. Ultrasound waves have low  
614 absorption and backscattering and thus can penetrate over decimeters in the integumentary and  
615 musculoskeletal systems of the human body. Ultrasound has been able to achieve temporal  
616 resolutions of less than 1 ms<sup>135</sup>. The spatial resolution of ultrasound increases with the frequency.  
617 However, this comes at the cost of penetration depth as higher frequencies are more strongly  
618 attenuated by tissues<sup>134,136</sup>. In general, most conventional diagnostic ultrasound devices use sound  
619 waves in the range of 2-18 MHz<sup>134</sup> and can achieve spatial resolutions in the range of 0.4-2 mm<sup>137</sup>.  
620 Additionally, even for long-term use, ultrasound has largely been considered fully safe as long as  
621 the power output is kept at the minimum levels needed<sup>138</sup>, below the safety threshold defined by  
622 FDA ( $I_{SPTA} \leq 720 \text{ mW/cm}^2$ ,  $I_{SPPA} \leq 190 \text{ W/cm}^2$ )<sup>139</sup>. The mechanical energy itself is not toxic to  
623 the body.

624

625 In the case of arrhythmia, a wearable device with live B-mode and M-mode images is perfect  
626 for several reasons. First, heart beats are directly recorded and visualized in echocardiography by  
627 the wearable device, resulting in a high accuracy in calculating heart rates from B-mode videos or  
628 M-mode images. Second, arrhythmia is very unpredictable and may only happen when the heart  
629 is under high loads. The wearable device supports uninterrupted long-time monitoring in daily life  
630 and can capture any irregularity in heart beats. Third, the abnormal cardiac structure causing  
631 arrhythmia can be easily detected in B-mode images, which visualize the root cause of the disease  
632 and inform better therapeutic decisions. For example, the gross dilations of the right atrium and  
633 right ventricle are considered as an important indicator of arrhythmia<sup>140</sup>.

634

635 The main drawback of ultrasound is that there is inherently a lot of noise in the signal, due to  
636 random scatterers in the tissue<sup>141</sup>. However, significant algorithmic progress has been made in this  
637 area to improve the image quality of modern ultrasound scanners. Especially given its versatile  
638 functions in clinical applications, ultrasound still remains extremely viable, as well as the best  
639 option as a wearable modality for imaging the heart.

640

641 As of the time of writing, there have been no other studies that have produced, specifically,  
642 wearable ultrasound heart imaging devices. A wearable device was made to target the heart<sup>142</sup>, but  
643 did not have imaging capability. Therefore, the wearable heart imaging capability introduced in  
644 this study addressed a critical unmet need.

645

## 646 2.8 Comparability of the wearable ultrasound to clinical ultrasound

647 Traditional ultrasound probes require either constant holding and/or repositioning of the probe  
648 each time before taking a measurement. The wearable imager reduces the user dependency down  
649 to a single placement of the probe at the start, after which no operator is necessary because the

650 patch remains adhered in place. Furthermore, in regions where sonographers are a scarce resource,  
651 such an advantage could allow a single sonographer to attend to multiple patients at a time, as they  
652 would not have to physically hold the probe for each patient.

653

654 In spite of these advancements, the wearable imager is not fully immune to user-dependency  
655 either. Because ultrasound cannot penetrate bone, an ultrasound probe must always be correctly  
656 positioned such that the region of interest is within the imaging window with a clear line of sight  
657 unobstructed by bones. This user-dependence can be further minimized by 3D imaging or 2D  
658 plane-steering, which is an effective way to eliminate the user-dependency.

659

660 The images from the wearable imager, while comparable to the commercial probes, are not at  
661 the same level as those taken by a cardiologist using a clinical machine. The models of the  
662 commercial probe and the driving system we used were P4-2v and Vantage 256 from Verasonics  
663 company, which is widely known for manufacturing cutting-edge research ultrasound systems.  
664 Nonetheless, the Verasonics system performance is still not as good as clinical ultrasound systems  
665 manufactured by General Electric or Philips, which excel in designing ultrasound transmitting and  
666 receiving modes and customizing image post-processing algorithms for each imaging target. We  
667 acquired cardiac images taken by an experienced cardiologist using a clinical machine in the  
668 hospital (Supplementary Fig. 32).

669

670 However, those clinical ultrasound systems have fixed adaptors and algorithms that cannot be  
671 adapted to driving the wearable imager in this study. Therefore, we used Verasonics, a  
672 programmable research platform, to drive the patch. In Figure 3a, we compared B-mode cardiac  
673 images tested by the wearable imager and the commercial P4-2v probe. Those two devices were  
674 controlled by the Verasonics Vantage 256 machine with the same transmitting mode and image  
675 post-processing algorithms. In this case, we could make a fair performance comparison between  
676 the wearable imager and the commercial P4-2v probe.

677

678 The size and cost of the back-end hardware can be readily reduced by replacing it with a  
679 printed circuit board used for the commercial portable ultrasound probe. We will work on  
680 prototyping a printed circuit board with pulsing, receiving, and data transmitting units and  
681 integrating it with the wearable ultrasound imager. The printed circuit board will have a  
682 miniaturized footprint. Additionally, the entire system can be powered by a lithium-polymer  
683 battery with a voltage of only 3.7 V. The voltage can be amplified up to 200 V by a voltage  
684 regulator. We will eventually prototype the printed circuit board in a compact and multilayered  
685 structure and make it flexible or even stretchable.

686

687 Furthermore, the mechanical index, spatial resolution, and contrast-to-noise ratio can be  
688 further improved by using single crystal piezoelectric materials, adding matching layer and lens,

689 increasing the number of elements, implementing harmonic imaging, and shrinking the pitch  
690 further to eliminate the artifacts. The near-field is excessively bright and can be improved by  
691 suppressing the ring-down with backing layer materials of high attenuation coefficients. The sector  
692 angle of the sonographic window is limited and can be improved by shrinking the array pitch so  
693 that the ultrasound beam can steer to a large angle without generating grating lobe-based artifacts.  
694 New algorithms will be explored to maintain a high frame rate while at an expanded sector angle.  
695 We could also fabricate a large wearable imager so that it covers multiple positions simultaneously.  
696 This large array will eliminate the need to repositioning when imaging different sites. To achieve  
697 that, we will have to develop a new wiring strategy to individually address each transducer element  
698 in the large array.

699

### 700 **Supplementary Discussion 3: Configuration of the array**

701

#### 702 3.1 The configuration of the array in this study

703 The device is composed of two orthogonal 1D arrays, which can be separated into two parts:  
704 four arms and a central area (Extended Data Fig. 1). Each arm consists of 13 elements, with each  
705 element containing a row of  $6 \times 1$  sub-elements. The  $6 \times 1$  sub-elements are shorted and controlled  
706 as one channel. We divided one element into  $6 \times 1$  sub-elements to considerably improve the  
707 stretchability of the device, which could conform more intimately to the curved human skin and  
708 provide a better interfacial coupling condition. The central area consists of 36 individually  
709 addressable sub-elements, whose activation can be configured through customized algorithms as  
710  $6 \times 1$  elements in either arm of the array. Because the array pitch is less than one wavelength of the  
711 ultrasound wave, the device can be considered as two phased arrays with 32 elements in each.

712

713 The 88 channels were physically plugged into the control system, but not all of them were  
714 activated all the time. The activating sequence was controlled by the customized algorithm to  
715 reconstruct two sectorial images sequentially. Specifically, the 32 elements in one direction of the  
716 orthogonal array transmit and receive ultrasound waves first. After a sectorial B-mode image has  
717 been reconstructed, the system deactivated this direction and switched to controlling the other  
718 direction of the orthogonal array to form the second image. Different from how traditional 2D  
719 matrix probes work, this method is limited to only one pair of cross planes (one along each phased  
720 array; Extended Data Fig. 1). The 2D matrix probe reconstructs a whole 3D image first, and then  
721 extracts any pairs of cross planes from the whole 3D image. In other words, this method captures  
722 extra unneeded data, which is more time-consuming, leading to a lower frame rate than the method  
723 in this study. Because these standard echocardiographic views are orthogonal to each other and the  
724 other cross planes in between are of less interest, our method optimizes the frame rate without  
725 losing key data.

726

727 However, the disadvantage is that our method cannot do 3D imaging nor capture all cross  
728 planes from a single probe position. To overcome these disadvantages, our future work will focus  
729 on developing a wearable 2D matrix probe that can achieve 3D imaging and thus extract any pairs  
730 of cross planes.

731

### 732 3.2 The Mills cross array

733 The configuration of Mills cross arrays<sup>143-146</sup> is almost the same as that of our orthogonal array  
734 (Supplementary Fig. 34): two linear or phased arrays in orthogonal orientations with the central  
735 elements shared by two arrays. The three major differences between them are (1) the Mills cross  
736 array was rigid and the orthogonal array is stretchable; (2) the Mills cross array can reconstruct  
737 both 2D and 3D images<sup>147</sup>, while our device can only conduct imaging in two 2D planes; (3) the  
738 manner of ultrasound transmission and receiving are different, as detailed in the following.

739

740 In the Mills cross array, one array serves for transmitting beamforming in the elevational  
741 direction and the other for receiving beamforming in the azimuthal direction (Supplementary Fig.  
742 34). In this way, a 2D image can be reconstructed with focusing in the elevational direction.  
743 However, this method has a major limitation: the effective aperture in the azimuthal plane is very  
744 small (determined by the shared center of the cross array). Such a small aperture diminishes the  
745 reflected signals that go to the receive array, resulting in a low signal-to-noise ratio, and degrades  
746 the lateral resolution in the azimuthal direction, causing low-quality of reconstructed images<sup>145</sup>.  
747 On the contrary, performing the transmit and receive beamforming using one common phased  
748 array will not have this problem due to its long effective aperture in the azimuth plane, yielding  
749 2D B-mode images with high qualities in this work.

750

### 751 3.3 The 1.5D/1.75D array

752 We did not create 1.5D or 1.75D arrays either because of three strong reasons. First, a 1.5D  
753 or 1.75D array will need more electrodes. Specifically, the 1.5D and 1.75D arrays would include  
754 104 and 260 additional electrodes compared to the current probe, respectively<sup>20</sup>. This design  
755 configuration would require fabricating more than 10 layers of electrodes, which would make the  
756 top electrode excessively thick and compromise the device's mechanical compliance. Second, it  
757 would significantly lower the imaging frame rate as it would involve an additional beamforming  
758 process in the elevational direction. The frame rate is crucial for cardiac imaging because of the  
759 highly dynamic cardiac movement. A low frame rate reduces the number of data points in the left  
760 ventricular volume waveform, causing aliasing of critical features in the waveform of cardiac  
761 cycles, such as diastasis and isovolumetric contraction (Fig. 5b right). The outcomes are inaccurate  
762 stroke volume, ejection fraction, and cardiac output. The frame rates for 1.5D or 1.75D arrays are  
763 typically  $<10$  Hz<sup>148-150</sup>, which could not support high-fidelity waveform extraction from the video.  
764 Third, it is highly likely that there will be a strong grating lobe in the elevational direction due to  
765 the transmitting beamforming implemented by a small number of elements, which can induce

766 artifacts into the images<sup>20</sup>. Therefore, this work focuses on achieving cardiac 2D B-mode images  
767 using 1D phased array.

768

769 There is no focusing effect in the elevational direction for the orthogonal array in this work,  
770 which may diverge ultrasonic energies transmitted to deep tissues. To mitigate this problem, we  
771 used an advanced compounding transmission approach and high transducer performance with a  
772 large electromechanical coupling coefficient in this work to maximize the transmission and  
773 reflection energies in the azimuth and axial directions. This strategy compensates for the energy  
774 loss due to the lack of the elevational focusing, resulting in bright and clear cardiac images even  
775 at a depth of 14 cm. To further improve the elevational resolution, we will replace the linear arrays  
776 with 1.75D or 2D array<sup>20</sup> in future studies.

777

#### 778 **Supplementary Discussion 4: Possible sources of electromagnetic interference**

779

780 The noise in the ultrasound signals had such an ultra-wide bandwidth that the most likely  
781 source was radio communication signals. The electromagnetic wave frequencies beyond the  
782 ultrasound signals (1-5 MHz) in this study could be removed by applying digital filters to the  
783 received signals. For electromagnetic wave frequencies within this range, e.g., the amplitude-  
784 modulated radio and short-wave radio, they could not be removed by digital filters but could be  
785 mitigated by adding a shielding layer. For the latter, we could attribute the noise to the following  
786 two possible sources:

787

788 (1) Electromagnetic noise received by the electrodes or transmission lines directly from the  
789 ambience<sup>151</sup>. Without the shielding layer, bare transmission lines and the electrodes can  
790 act as an antenna to receive those ambient electromagnetic waves.

791

792 (2) Electromagnetic noise coupled from the human body<sup>152</sup>. We observed an increasing noise  
793 amplitude when the device got close to the human body, indicating an electrical field  
794 approaching the human body. When electromagnetic waves pass by the human body, they  
795 will generate magnetically-induced electrical potential in the human body according to the  
796 Faraday's law of electromagnetic induction. In this case, the human body can be  
797 considered as a circuit that generates an additive electrical field to the ambient  
798 electromagnetic waves. Even though the conductivity of various parts of the human body  
799 is low compared with metal conductors, some parts of the human body can still form a  
800 loop and generate electrical potential. The potentials can be coupled to device signals as  
801 noise<sup>153</sup>.

802

#### 803 **Supplementary Discussion 5: Measurement variations of imaging metrics**

804

805 Taking the measurements of axial resolutions as examples, there were cases where the axial  
806 resolution of wearable probe was better than that of commercial probe due to the variation in  
807 measurements (position of the probe, rotation of the probe, etc.). Because the surface of the  
808 commercial probe is not flat, the degrees of freedom of the commercial probe will be five, as  
809 indicated by the red arrows in the Supplementary Fig. 18. The degrees of freedom of the wearable  
810 probe will be three, as indicated by the red arrows in the Supplementary Fig. 18. The variations  
811 can be introduced in many forms:

812

- 813 1) When the commercial probe is tilted in the side view (Supplementary Fig. 18a Side view),  
814 or the commercial and wearable probes are rotated in the top view (Supplementary Fig. 18  
815 Top views), the cross section of the filament is enlarged (from a circle to an ellipse). This  
816 will cause a longer radiofrequency signal, similar to the effect of reduced bandwidth. A  
817 longer radiofrequency signal will increase the size of the bright region generated by each  
818 filament target, causing a worse axial resolution.
- 819 2) When the commercial and wearable probes are moved laterally in the front view  
820 (Supplementary Fig. 18 Front views), or the commercial probe is tilted in the front view  
821 (Supplementary Fig. 18a Front view) the filament targets will be off-axis from the center.  
822 Then the ultrasound beam intersecting the targets will be more diverged compared to the  
823 center beam. The diverged beam has a greater tendency to collect more signals from  
824 neighboring targets. This will also lead to a seemingly longer radiofrequency signal. As a  
825 result, this kind of positioning will also increase the bright region generated by each  
826 filament target and hence worsen axial resolution.
- 827 3) When the commercial and wearable probe are moved laterally in the side view  
828 (Supplementary Fig. 18 Side views), the probes get closer to the phantom boundary. The  
829 closer the probes are to the boundary, the higher the signals from the boundary are. Then  
830 the background of the whole image gets brighter. And it is possible that the background  
831 plus the noise in the radiofrequency signal will give a background gray value greater than  
832 half of that of the deep filament targets (the deeper the target, the dimmer the pixels in the  
833 image). This will lead to a higher pixel count, which leads to longer physical distance  
834 (Equation 2, Methods), resulting in a worse axial resolution according to the discussion on  
835 characterization of the wearable imager in the Methods section.

836

837 To reduce the impact of measurement variations, we repeated the same test five times. The  
838 axial resolutions from each test are shown in Supplementary Fig. 18. Even though the wearable  
839 imager sometimes shows a better axial resolution, the mean axial resolution of the commercial  
840 imager is superior due to its higher bandwidth. The error bars for all measurements in Figs. 2d, 2e  
841 and Supplementary Fig. 17 show the standard deviation of the measurements.

842

843 **Supplementary Discussion 6: Imaging procedures**



844

## 845 6.1 Imaging from different views

846 Four standard positions/orientations were used to obtain the best B-mode images of the heart.  
847 The first position was on the left side of the sternum, between the second and fourth intercostal  
848 spaces. A linear array device was pointing to the right shoulder. From this position, the imager  
849 could inspect the parasternal long axis view of the left ventricle. By rotating the device 90 degrees  
850 counterclockwise at the same position, with the device pointing to the left shoulder, a parasternal  
851 short axial view of the left ventricle could be obtained. The second position was between the fourth  
852 and fifth intercostal spaces. With the linear array device pointing to the left shoulder, the four  
853 chambers of the heart could be observed from the apex in this view, also known as the apical four-  
854 chamber view. By rotating the device 90 degrees counterclockwise at the same position and aiming  
855 towards the right shoulder, the device revealed the left ventricle, left atrium, and mitral valve, i.e.,  
856 apical two-chamber view.

857

858 After the transducer received the response echoes that carry the location and anatomic  
859 information of the heart, the echoes were demodulated, decimated, and compressed  
860 logarithmically to eventually generate the B-mode image. A graphical user interface for real-time  
861 phased array imaging was made up of display windows and control panels for customized settings  
862 (Supplementary Fig. 33).

863

864 In the apical four-chamber view, all four chambers could be seen simultaneously, so that  
865 ventricular interdependence and septal wall abnormalities between the chambers (e.g., in cor  
866 pulmonale) could be assessed. We could also measure left and right atrial lengths and areas, as  
867 well as right ventricular diameter, length, and area.

868

869 Apical two-chamber view could be used to measure the left atrial length and area.

870

871 In the parasternal long axis view, detectable structures include the left atrium, left ventricle,  
872 mitral valve, aortic valve, interventricular septum, right ventricle, and left ventricular outflow  
873 tract<sup>154</sup>. The unique orientation of this view allows visualizing the full length of the mitral and  
874 aortic valve leaflets during their closure and excursion, which makes it especially useful for  
875 evaluating valvular functions. Measurements taken in the parasternal long axis view include the  
876 interventricular septum end-diastole thickness, the left ventricular internal diameter end-diastole  
877 (LVIDd), left ventricular internal diameter end-systole (LVIDs), and left ventricular posterior wall  
878 dimensions. Among the measurements, the LVIDd and LVIDs are especially valuable because  
879 they are correlated with the left ventricular volume. By increasing the imaging depth, the  
880 pericardial and pleural spaces can also be seen from this view.

881

882 The parasternal short axis view was particularly useful for evaluating the left ventricular wall  
883 motion. To do so, we adopted rings divided into a total of 17 segments to assist the mapping of  
884 local pathologies. The 17-segment model is a standard tool used in transthoracic echocardiography  
885 procedures. In the 17-segment model, the entire left ventricular wall is projected onto a 2D plane,  
886 forming a circular projection area made up of multiple concentrically nested rings with varied  
887 diameters. Each ring represents the myocardial wall from a different level of the left ventricle,  
888 corresponding to the decrease in the diameter of the left ventricular wall from base to apex (viewed  
889 from the parasternal short axis). The rings are further divided into a total of 17 segments, each of  
890 which receives its blood supply from a different coronary artery. Segmenting the left ventricular  
891 wall in this way provides a useful localization mapping that allows abnormal myocardial strain in  
892 any given segment, due to cardiac malfunctions such as ischemic heart diseases or myocardial  
893 infarction, to be traced back to its corresponding coronary artery of origin.

894  
895 In the short-axis plane, the circular cross-section of the left ventricle was captured (the basal,  
896 mid-cavity, and apical views/slices), and the contractility and distensibility were accessible as the  
897 motion of the walls was along the plane. The basal slice captures the ring with the largest diameter  
898 (segments 1-6). The mid-cavity slice captures a smaller diameter ring nested inside the basal view  
899 (segments 7-12). Likewise, the apical slice is nested inside the mid-cavity slice (segments 13-16).  
900 Segment 17 is the apex. Therefore, the relative changes in the cross-sectional diameter, along with  
901 the uniformity of wall motions, could be easily assessed. Using these assessments, we can identify  
902 the specific segment of the left ventricular wall as pathological.

903  
904 To quantitatively evaluate the segment displacement, we set a target area for each segment to  
905 facilitate further processing. We blurred the original images in the area to reduce the impact of  
906 speckles on the feature refinement, and then computed the edge information using a Canny  
907 operator based on the blurred image. By indexing the edge in the binary map, the myocardium  
908 displacement could be recorded. With these measurements, we could monitor the potential risk  
909 factors for myocardial infarction or akinesia, precisely localize ischemic heart diseases, and easily  
910 assign hypokinetic or akinetic regions of the left ventricular wall to their governing coronary  
911 arteries by tracking the relevant myocardium\_displacement<sup>155</sup>.

## 912 913 6.2 Phase correction on nonplanar surfaces

914 Applying phase correction allows the wearable imager to cover a more diverse population,  
915 including obese people. Also, the phase correction is critical for providing accurate cardiac  
916 monitoring. Because we used a wide-beam compounding transmission in this study, the delay  
917 calculation for the aperture could vary a lot from traditional plane-wave compounding  
918 transmission<sup>27,156</sup>. As an intrinsic feature of wide-beam transmission, the focal point of the aperture  
919 was set at the opposite side to the imaging area, with the distance between the focal point and the  
920 center of the aperture kept constant during the transmission (Supplementary Fig. 13).

921  
 922  
 923  
 924  
 925  
 926  
 927  
 928  
 929  
 930  
 931

Assuming that a linear array of the wearable imager was attached to a planar surface, the transmission and time delay could be calculated following the general approach. Considering the center of the linear array located at (0,0) by default, we can define the distance between the focal point and the center of the aperture as  $df = \sqrt{x_{focal}^2 + z_{focal}^2}$ , in which  $z_{focal} < 0$ . Also, the location of the  $i^{th}$  transducer could be defined as  $(x_i, 0)$ , where  $x_i = (i - 16.5) \times pitch$  because the device had 32 transducers in each imaging plane. Additionally, we defined the aperture size as  $A$  and the angle departure from the vertical direction as  $\theta$ , where  $\theta > 0$  when  $x_{focal} > 0$ . For a given position of a pixel  $(x_p, z_p)$ , the time of the wavefront to go to the pixel since the earliest trigger on the transducers was:

$$t_{\theta,p}^e \approx \frac{\sqrt{(x_p - df \times \sin \theta)^2 + (z_p - df \times \cos \theta)^2} - dt}{c} \quad (13)$$

932  
 933

where  $dt = df \times \cos \theta$  when  $|df \times \sin \theta| < \frac{A}{2}$  and  $dt =$

$\sqrt{(df \times \sin \theta - \text{sign}(\theta) \times \frac{A}{2})^2 + (df \times \cos \theta)^2}$  when  $|df \times \sin \theta| \geq \frac{A}{2}$ . And the time for the reflected wave to get back to the  $i^{th}$  transducer was:

$$t_{i,p}^r = \frac{\sqrt{(z_p - z_i)^2 + (x_p - x_i)^2}}{c} \quad (14)$$

938  
 939

The total time delay since the trigger should be

940  
 941

$$t_{i,\theta,p}^{dt} = t_{\theta,p}^e + t_{i,p}^r \quad (15)$$

942  
 943

where  $c$  was the speed of sound that we assumed to be constant in the medium. Considering the delay differences among transducers, the delay of trigger of  $i^{th}$  transducer was:

944  
 945  
 946

$$t_{i,\theta}^t \approx \frac{\sqrt{(df \times \sin \theta - x_i)^2 + (df \times \cos \theta - z_i)^2} - dt}{c} \quad (16)$$

947  
 948

As a result, the delay of the  $i^{th}$  transducer for beamforming at a given pixel was:

949  
 950

$$t_{i,\theta,p}^{total} = t_{i,\theta,p}^{dt} - t_{i,\theta}^t \quad (17)$$

951

952

953 since each channel started to receive data after transmission.

954

955 When the device was placed on a nonplanar surface, the time delay formula above was no  
956 longer valid (Supplementary Fig. 15). Assume the curvature radius of the nonplanar surface was  
957  $r$ . The previous location the  $i^{th}$  transducer would then move to  $(x'_i, z'_i)$ , and

958

$$959 \quad x'_i = \text{sign}(x_i) \times r \times \sin \varphi \quad (18)$$

960

$$961 \quad z'_i = r \cdot (1 - \cos \varphi) \quad (19)$$

962

963 where  $\varphi = \frac{x_i}{r}$ .

964

965 With the phase correction, the time of the wavefront to go to the pixel since the earliest trigger  
966 on the transducers would be changed to

967

$$968 \quad t'_{\theta,p} \approx \frac{\sqrt{(x_p - df \times \sin \theta)^2 + (z_p - df \times \cos \theta)^2} - dt'}{c} \quad (20)$$

969

970 where  $dt' = \sqrt{df^2 + r^2} + 2 \times df \times r \times \cos \theta - r$  when  $|\varphi| < \frac{A}{2r}$  and  $dt =$

971  $\sqrt{(df \times \sin \theta - \text{sign}(\varphi) \times |x'_1|)^2 + (df \times \cos \theta - \text{sign}(\varphi) \times |z'_1|)^2}$  when  $|\varphi| \geq \frac{A}{2r}$ .

972 Meanwhile, the time for reflected waves to get back to the  $i^{th}$  transducer was changed to

973

$$974 \quad t'_{i,p} = \frac{\sqrt{(z_p - z'_i)^2 + (x_p - x'_i)^2}}{c} \quad (21)$$

975

976 and the delay of triggering the  $i^{th}$  transducer was changed to

977

$$978 \quad t'_{i,\theta} \approx \frac{\sqrt{(df \times \sin \theta - x_i)^2 + (df \times \cos \theta - z_i)^2} - dt'}{c} \quad (22)$$

979

980 Finally, the delay of the  $i^{th}$  transducer for beamforming at a given pixel after phase correction  
981 became:

982

$$983 \quad t'_{i,\theta,p}{}^{total} = t'_{\theta,p} + t'_{i,p} - t'_{i,\theta} \quad (23)$$

984  
985  
986

In the receive beamforming, the value of each pixel could be computed as:

$$I_p = 20 \log_{10} \sum_{\theta=\theta_{min}}^{\theta=\theta_{max}} \sum_{i=1}^{\# \text{ of channel}} RF_i(t'_{i,\theta,p} \times f_s) \quad (24)$$

988  
989  
990  
991

where  $RF_i$  is the radiofrequency signal collected for the  $i^{th}$  transducer and  $f_s$  is the sampling frequency. Any value larger than 255 would be cut off to adapt to the 8-bit display.

992  
993  
994  
995  
996  
997  
998  
999

In Extended Data Fig. 2, for the images labeled with “Planar”, we fixed the probe on a planar glass slide and used ultrasound couplant to compensate the gap between the probe and the skin. The images labeled with “Curved” were obtained with the probe naturally laminated on the curved skin surface. Exemplary images of the parasternal long axis view were collected on an obese subject, whose curvature radius at the imaging site was  $\sim 82$  mm. The size and shape of the left ventricle were obviously distorted without the phase correction. The measured values of the stroke volume, cardiac output, and ejection fraction tend to be smaller pre-phase correction than the results post-phase correction, due to the distorted size and shape of the left ventricle.

1000  
1001

### 6.3 Validation for long-term use

1002  
1003  
1004  
1005  
1006

Motion artifacts plague ultrasound imaging<sup>157-160</sup>. To verify the performance of the wearable imager under daily circumstances, we attached the device to subject’s chest and tested the imaging quality under different postures. In the experiments, there was no obvious deterioration of imaging quality, due to the intimate contact of the device to human skin (Extended Data Fig. 4), attesting the stable performance of the device.

1007  
1008  
1009  
1010  
1011  
1012

We compared the imaging results along the four standard views with ultrasound gel and silicone as the couplant (Supplementary Fig. 20). The results showed that the contrast between different structures and details in the heart anatomy were well conserved when the couplant was changed from ultrasound gel to silicone. We recycled the device and repeated the tests on ten subjects and obtained reliable and reproducible results (Supplementary Fig. 24).

1013  
1014  
1015  
1016  
1017  
1018  
1019

In addition, the biocompatibility of the device was also a potential concern for long-term use, which may adversely irritate the skin. We attached the device to the subject’s chest with a commercial adhesive (e.g., Tegaderm) for 24 hours (Supplementary Fig. 22), during which the skin experienced all kinds of scenarios, including exercising and showering. After removing the device, no allergy was observed. The major issue was the reddish area around the device attachment location caused by peeling off the Tegaderm adhesive.

1020  
1021

### 6.4 Simultaneous measurements of M-mode images and electrocardiogram

1022 At the beginning of the test, the wearable imager was attached to the parasternal site to image  
1023 along the parasternal short axis view. We triggered the recording of B-mode images and  
1024 electrocardiogram (by a commercial device, Cyton Biosensing Board 8 channels) simultaneously.  
1025 With the concurrent ending of the recording, the time (i.e., frame number in this case) of B-mode  
1026 images and electrocardiogram could be aligned. Furthermore, we plotted the M-mode image by  
1027 selecting pixels in one line in the B-mode images and correlating this array of pixels to the frame  
1028 number.

1029

## 1030 **Supplementary Discussion 7: Stress echocardiography**

1031

### 1032 7.1 Significance

1033 Under a steady state of a healthy subject, the left ventricular volume changes consistently, so  
1034 the stroke volumes, cardiac outputs, and ejection fractions (three of the most significant indicators  
1035 of cardiac functions) do not vary significantly<sup>161</sup>. However, the heart state may change frequently  
1036 and could be extremely intricate at times. Abnormal fluctuations exist in estimating the cardiac  
1037 function of patients with heart diseases, and the symptoms could be very unpredictable, which also  
1038 incur dramatic changes in the heart in a relatively short time. Symptoms of cardiovascular diseases  
1039 like myocardial ischemia only emerge under stress, where the induced wall motion abnormalities  
1040 are more noticeable<sup>162</sup>. Therefore, stress echocardiography is carried out. Valvular pathologies are  
1041 easily observed by individually tailored stress echocardiography<sup>163</sup>. In addition, stress  
1042 echocardiography is valuable for studying pulmonary circulation<sup>164</sup>. Stress echocardiography can  
1043 also help determine limits for safe exercise before starting a cardiac rehabilitation program or  
1044 recovering from a cardiac event, and sometimes help evaluate the cardiac status before heart  
1045 surgery.

1046

### 1047 7.2 Limitations of existing procedures

1048 The process of stress echocardiography sometimes suffers from inter-observer variabilities.  
1049 Current evaluation approach requires manually tracing the contour of the left ventricle in the  
1050 echocardiographic images and calculating its end-systolic and end-diastolic volumes for further  
1051 analysis. Assessments are carried out typically based on only one cycle of heartbeat, even if the  
1052 standard guidelines recommend tracking and averaging five cycles before making a  
1053 conclusion<sup>165,166</sup>. It potentially brings huge variance and uncertain accuracy to diagnostic results,  
1054 especially for those less-trained medical assistants in low-resource regions.

1055

1056 Stress echocardiography also requires extremely sophisticated procedures to find an  
1057 appropriate imaging location/orientation in a short time<sup>40</sup>. The acquired views must be of the same  
1058 regions of the myocardium before and after exercise<sup>40</sup>. Same regions in the ultrasonographic  
1059 window are required to make sure the images are from the same or a very similar

1060 location/orientation of the heart. Otherwise, the measurements will be incorrect, because the  
1061 chamber volume varies in images from different locations/orientations.

1062

1063 In addition, the end-point when the patient should stop exercising is dependent on whether  
1064 patients achieve the target heart rate, experience moderate angina/severe chest pain, or reach  
1065 tolerable exercise limits. These subjective criteria may result in suboptimal cardiac testing  
1066 outcomes.

1067

1068 Furthermore, patients may be vulnerable to certain diseases that show up only during exercise,  
1069 which is not monitored by existing procedures. For example, myocardial ischemia does not show  
1070 in the resting state but appears only in stress, resulting in hypokinesia, akinesia, and dyskinesia.  
1071 These symptoms are usually mild but can develop to be acute and lethal if neglected. However,  
1072 because the patient is not monitored during exercise, the initiation of myocardial ischemia is  
1073 unknown, not only missing valuable data but also leaving the patient at risk.

1074

### 1075 7.3 Echocardiography by the wearable imager

1076 Those limitations of existing echocardiography can potentially be addressed with the wearable  
1077 imager demonstrated in this study. The aperture of the wearable imager in this work is relatively  
1078 small. The entire array length is 12.7 mm, which is shorter than the intercostal space (~14.5 to 19.7  
1079 mm<sup>167</sup>). Therefore, imaging is not challenged by the ribs because we only image from one position  
1080 at a time, rather than using a big patch to cover many locations simultaneously. We imaged in the  
1081 parasternal axis views and apical views at different locations (Extended Data Fig. 3). In the  
1082 parasternal long axis view, the wearable imager was attached to the chest of the subject  
1083 continuously during the entire process. The heart rate was estimated to be average 70 beats per  
1084 minute for the rest stage, which changes occasionally though, but still within a normal range. Then,  
1085 the subject exercised on a cycling bike while the device continuously monitored the heart status.  
1086 As the exercise began, the heart rate gradually rose. The subject exercised as hard as possible to  
1087 reach the possible highest heart rate. The whole exercise duration took around 12 mins. After  
1088 exercise, the heart rate slowed down back to normal.

1089

1090 The LVIDs and LVIDd were measured during different stages. Before exercise, the average  
1091 LVIDd and LVIDs were 45 mm and 27 mm, respectively. During exercise, growing need of blood  
1092 supply accelerated the heart beats, but the LVIDd and LVIDs were slightly dropping because a  
1093 shorter pumping period allowed fewer muscle extensions. At the peak of exercise, LVIDd roughly  
1094 dropped to 38 mm and LVIDs went down to 22 mm. After exercise, the LVIDd and LVIDs  
1095 recovered to approximately 41 mm and 24 mm, respectively. Fractional shortening, the reduction  
1096 of end-diastolic diameter during systole, is a measure of the cardiac muscular contractility. It was  
1097 calculated as the difference between the LVIDd and LVIDs divided by the LVIDd.

1098

1099 The parasternal long axis view contains information mostly about the left ventricle and atrium,  
1100 while the apical four-chamber view provides a more comprehensive window of all four chambers  
1101 and is more precise for estimating the left ventricular volume. Because the apical four-chamber  
1102 view requires the patient to be tilted in the lying side position so ultrasound can enter from the  
1103 apex, we could not collect these data during exercise. In the apical four-chamber view, we could  
1104 see that both end-systolic volume and end-diastolic volume were increasing after exercise. This  
1105 process of heart restoration is sometimes defined as heart volume reversal<sup>168</sup>. Reasonably, exercise  
1106 leads to increases in both contractility and afterload of chambers, resulting in a physiological  
1107 decrease in chamber volumes immediately.

1108  
1109 Changes in ventricular size under stress may provide useful information regarding cardiac  
1110 functions. For example, the end-systolic volume reversal may provide complementary information  
1111 for risk stratification of cardiac diseases<sup>168</sup>. A decreasing end-diastolic volume may be a critical  
1112 indicator of hypovolemia resulting from poor oral intake, emesis, or myocardial loss during cancer  
1113 treatment<sup>169</sup>. An unsteady end-systolic volume recovery also portends the possibility of diseases  
1114 like septal defects<sup>170</sup> or valvular regurgitation<sup>171</sup>.

1115

### 1116 **Supplementary Discussion 8: Acoustic coupling of wearable imager**

1117  
1118 In this study, the 50-micron layer of silicone underneath the device is in a liquidous state  
1119 (Silbione part A, A-4717, Factor II Inc.). It was not used to encapsulate the array but instead as an  
1120 acoustic couplant and adhesive layer. The silicone layer is a structural material that improves the  
1121 acoustic coupling and adhesive properties of the device without limiting its flexibility.

1122  
1123 Rigid probes cannot provide meaningful B-mode images without couplants due to  
1124 incompatible mechanical properties between the rigid probe and the soft human skin  
1125 (Supplementary Fig. 21d left panel). The stretchable ultrasound patch is packaged by skin-like soft  
1126 polymers, i.e., SEBS in this case. The mechanical compliance of the patch allows intimate  
1127 conforming to the human skin without external holding, which reduces interfacial air gaps and  
1128 enhances acoustic coupling between the transducer and human skin. Therefore, the patch can  
1129 image the human body even without coupling materials.

1130  
1131 With that being said, microsized air bubbles may still exist at the wearable patch/skin interface.  
1132 To achieve the best acoustic coupling, we added uncured Silbione (part A, A-4717, Factor II Inc.),  
1133 a thin layer of liquid silicone whose acoustic impedance (1.03 MRayl)<sup>172</sup> is very close to the human  
1134 skin, as the couplant underneath the device. The couplant can eliminate microsized air bubbles and  
1135 enhance the coupling between the device and the skin. In addition, traditional hydrophilic  
1136 ultrasonic gels are volatile and cannot last for long periods of time. The silicone couplant does not



1137 evaporate at room temperature. Therefore, it can provide a good acoustic coupling over the long  
1138 term.

1139

1140 To illustrate the performance of the silicone couplant, we compared the image quality of the  
1141 wearable patch on the human body with and without the silicone layer (Supplementary Fig. 21d).  
1142 The cardiac anatomic structures are clearly displayed. The image with silicone couplant is brighter  
1143 than that without, indicating a stronger signal-to-noise ratio due to better interfacial acoustic  
1144 coupling.

1145

1146 To quantify the coupling performance of the liquidous silicone, we have used a single  
1147 transducer to sense a specific target. Specifically, we excited the transducer with a thin layer of  
1148 liquidous silicone as couplant, and then acquired the reflected signals. For comparison, we also  
1149 did the same test using commercial ultrasound gel as couplant. We did the experiments on a  
1150 commercial phantom (Aquaflex, Parker Laboratories) with a reflector 18 mm underneath the  
1151 surface. The results show a comparable signal-to-noise ratio between commercial ultrasonic gel  
1152 and liquidous silicone (Supplementary Fig. 21), indicating the outstanding acoustic coupling  
1153 performance of the silicone.

1154

1155 In addition, we also imaged the heart from four different views with commercial ultrasound  
1156 gel as the couplant. The resulting images were compared with Supplementary Fig. 20 generated  
1157 with liquidous silicone as the couplant. Images from all views show that the contrast between  
1158 different structures and details in the cardiac anatomy are highly similar, and no obvious structural  
1159 differences are found. These results show the practicality and excellent performance of liquidous  
1160 silicone-based couplant.

1161

1162 The acoustic attenuation of the silicone is negligible. The attenuation depends on the  
1163 ultrasound frequency and the material thickness. Given the attenuation coefficient of  $\sim 0.11$  dB/mm  
1164 for liquidous silicone at 3 MHz<sup>173</sup>, a 50  $\mu\text{m}$  thick couplant only causes 0.005 dB attenuation, which  
1165 has practically no negative effect on the acoustic properties of the wearable ultrasonic array.

1166

1167 Furthermore, the liquidous silicone has a high viscosity (60 Pa·s)<sup>174</sup>, which makes the device  
1168 less susceptible to sliding on the skin, ensuring a consistent imaging window on the same target  
1169 during long-term continuous monitoring.

1170

## 1171 **Supplementary Discussion 9: Continuous cardiac performance monitoring**

### 1172 9.1 Monitoring ejection fraction, cardiac output, and stroke volume simultaneously

1173 Commonly monitored vital signs contain body temperature, respiration rate, peripheral blood  
1174 pressure, and heart rate. The first three parameters cannot directly reflect the heart status, while  
1175 the heart rate only tells how quickly the heart is pumping but does not reveal the actual

1176 performance of the heart. Other parameters, like ejection fraction, cardiac output, and stroke  
1177 volume should be explored for a more comprehensive and conclusive diagnosis.

1178

1179 Ejection fraction represents the fraction of the blood ejected from the left ventricle per cycle.  
1180 It is an indicator of the left ventricle's overall systolic performance (Equation 23). Cardiovascular  
1181 diseases lurk in an abnormal fluctuation of ejection fraction. Normal left ventricular ejection  
1182 fraction should be  $\geq 50\%$ , and a reduced one may manifest itself as heart failure<sup>175</sup>: a moderately  
1183 reduced ejection fraction is within 40-49%, and a reduced one is  $< 40\%$ . Chronically attenuated  
1184 ejection fraction is undoubtedly a danger sign, and an unreasonably high ejection fraction also  
1185 entails troubles like hypertrophic cardiomyopathy<sup>176</sup>, a common cause of sudden cardiac arrest.  
1186 As one of the most clinically significant indices of cardiac function, ejection fraction is key in  
1187 differentiating systolic versus diastolic heart failure, and is well correlated with mortality in stable  
1188 outpatients with coronary artery disease and heart failure<sup>177,178</sup>.

1189

1190 Cardiac output is a volumetric blood flow rate and is an indicator of the tissue oxygenation  
1191 (Equation 24). The cardiac output, the product of the heart rate and the stroke volume, the blood  
1192 volume pumped from the left ventricle every minute<sup>179</sup>, can aid in the diagnosis of heart failure  
1193 conditions, monitor patient status during surgeries and intensive care, and evaluate the overall  
1194 cardiac functions<sup>180</sup>. The cardiac output is widely monitored in anesthesiology and emergency  
1195 care<sup>181</sup>. Measurement of cardiac output is specifically essential in unstable patients whose  
1196 condition may undergo dramatic changes in a short time, as it indicates an overall systemic oxygen  
1197 delivery and tissue perfusion<sup>182</sup>. Many pathologies besides cardiovascular diseases lead to changes  
1198 in cardiac output. Abnormally decreased cardiac output could be a sign of heart failure caused by  
1199 valvular heart diseases<sup>179</sup>, but also could be intoxications like acute azotemia<sup>183</sup>, indicating a severe  
1200 dysfunction of the kidney. Aberrant high cardiac output may be a complication of sepsis<sup>184</sup>,  
1201 hyperthyroidism<sup>185</sup>, or anemia<sup>186</sup>. When evaluating the cardiac output, oftentimes a patient may  
1202 appear asymptomatic during resting conditions due to a wide range of physiological regulatory  
1203 processes such as vasodilation and minor increases of heart rate within the physiological range.  
1204 Therefore, maximal cardiac output measurements during exercise are also of particular interest for  
1205 their ability to reveal underlying problems in otherwise normally asymptomatic subjects.

1206

1207 Stroke volume is the difference between the EDV and the ESV, representing the absolute  
1208 blood volume ejected from the left ventricle in a single cycle. Stroke volume, when used together  
1209 with cardiac output and/or ejection fraction, can provide a much more comprehensive overview of  
1210 the cardiac status. For example, as mentioned above, cardiac output can often appear asymptomatic.  
1211 In those cases, the presence of a lowered stroke volume may reveal underlying heart failure. In  
1212 other cases, a patient might appear asymptomatic if only considering the ejection fraction. Then,  
1213 the presence of a decreased stroke volume would be able to indicate diastolic heart failure.

1214

1215 There are several other examples demonstrating why monitoring any one of these parameters  
1216 in isolation may lead to inaccurate diagnosis results. For example, ejection fraction may overstate  
1217 cardiac functions in left ventricular hypertrophy, which can lead to heart failure. In this case,  
1218 ejection fraction remains normal, but stroke volume and cardiac output are dropping<sup>187-189</sup>, which  
1219 is also well known as heart failure with preserved ejection fraction. Diagnosis only based on  
1220 ejection fraction would be wrong, while a comprehensive analysis on ejection fraction combined  
1221 with cardiac output and stroke volume can generate correct results. Conversely, diastolic and  
1222 systolic dysfunctions of the left chambers sharply reduce ejection fraction<sup>190</sup>, but the cardiac output  
1223 can maintain in the normal range with compensation of increased heart rate. Besides cardiac  
1224 diseases, some surgical procedures may also have impacts on cardiac functions that require  
1225 monitoring these three indices simultaneously.

1226  
1227 This scenario is also paralleled in the measurement of blood pressure, which is commonly  
1228 done in current practice. Blood pressure reflects a composition of multiple contributing factors,  
1229 for example, cardiac pre-load and vascular resistance. Much like the scenarios presented by stroke  
1230 volume, ejection fraction, and cardiac output, a normal blood pressure reading could obscure  
1231 underlying abnormalities in the cardiac pre-load, and vascular resistance if measured in isolation.  
1232 Measurement of the left ventricular volume can serve as an indicator for these factors contributing  
1233 to blood pressure. The cardiac pre-load is how much the myocardium is stretched prior to  
1234 contraction, and is reflected in the EDV<sup>191</sup>. Vascular resistance can be estimated from cardiac  
1235 output using lumped parameter models of the circulatory system<sup>192,193</sup>. The ability to monitor the  
1236 volume of the left ventricle can thus provide insight into the contributing factors to blood pressure  
1237 and reveal diseases that might otherwise be obscured.

1238  
1239 Therefore, ejection fraction, cardiac output, and stroke volume are important parameters for  
1240 evaluating cardiac performance<sup>194</sup>, and together provide a comprehensive analysis of the blood  
1241 delivery capabilities of the heart. Continuously monitoring these indices of the heart for the long  
1242 term is of strong prognostic value and has great potential to decrease the mortality and morbidity  
1243 of many cardiovascular diseases and conditions.

## 1244 1245 9.2 Monitoring the left ventricular volume by 3D imaging

1246 From Equations 22 to 24, the ejection fraction, cardiac output, and stroke volume are directly  
1247 related to the volume of the left ventricle (EDV and ESV). Thus, the most direct method to measure  
1248 these indices would be to monitor the left ventricular volume. Ideally, the most accurate and direct  
1249 approach would be to capture 3D images of the left ventricular chamber throughout the cardiac  
1250 cycle and use those 3D images to calculate the volume. Common methods of capturing these 3D  
1251 images include traditional ultrasound, computed tomography, radionuclide imaging, and magnetic  
1252 resonance imaging. However, these common cardiac imaging techniques have a host of limitations,  
1253 including device bulkiness, low temporal resolutions, and long-term toxicity to the body.

1254 Furthermore, in many cases, it is desirable to continuously monitor cardiac output in the operating  
1255 theater to prevent complications during surgery such as shock<sup>195</sup>, which is not viable for the  
1256 aforementioned techniques given these drawbacks.

1257  
1258 In addition, the calculation based on manual image labelling suffers from interobserver  
1259 variability. Specifically, when labelling the left ventricular dimensions, the endocardial border  
1260 requires to be traced continuously from one side of the mitral annulus to the other side. However,  
1261 because the endocardial is hypoechoic, no sharp boundary can be easily seen in the image, yielding  
1262 large discrepancies of left ventricular dimensions between clinicians' observations<sup>42</sup>. The  
1263 discrepancies can be further magnified in calculating stroke volume, cardiac output, and ejection  
1264 fraction, which results in an inaccurate diagnosis and introduces uncertainties in subsequent  
1265 treatment regimens. In addition, less severe abnormality suffers from greater interobserver  
1266 variability, where early symptoms will easily slip away if not well measured by two or more  
1267 experienced echocardiographers.

1268  
1269 9.3 Monitoring the left ventricular volume by 2D imaging

1270 The next most direct method of obtaining the left ventricular volume would be to approximate  
1271 the 3D volume of the left ventricle through 2D imaging. This approach faces similar problems due  
1272 to the use of imaging but is computationally faster and can achieve higher temporal resolutions  
1273 than 3D imaging.

1274  
1275 While 2D imaging with ultrasound is a widely used approach for its convenience, traditional  
1276 ultrasound has a bulky housing and requires the probe to be manually held in place. Point-of-care  
1277 ultrasound probes transcend the limitations of traditional medical imaging<sup>11</sup> and promote precision  
1278 medicine for household use, but they still require an external force to maintain a stable coupling  
1279 with the skin. Otherwise, the image window will change and generate unfair comparisons, which  
1280 results in misdiagnoses. In addition, their use highly depends on the clinicians' experience, which  
1281 is prone to generating inter-observer variabilities and operational errors<sup>196</sup>. Robotic arms have been  
1282 applied in such a case, but the higher cost and the even more bulky design are the new problems<sup>197</sup>,  
1283 making it inaccessible in most cases and impractical for continuous and long-term measurements.

1284  
1285 9.4 Monitoring the left ventricular volume by model estimations

1286 Therefore, the traditional approaches to continuously monitoring stroke volume, cardiac  
1287 output, and ejection fraction do not tend to employ imaging, but instead use models to estimate  
1288 these parameters from other indirect measurements. Here, we provide a review of some of the  
1289 major relevant non-imaging methods.

1290  
1291 (a) Fick's method

1292 According to the Fick principle, the ratio between the rate at which oxygen is absorbed into  
1293 the blood and the rate at which blood is delivered through the body, is directly represented by the  
1294 difference in blood oxygen content between mixed venous blood and arterial blood. This principle  
1295 is summarized by<sup>180</sup>:

$$CO = \frac{VO_2}{C_a - C_v} \quad (25)$$

1298 where  $CO$  is cardiac output,  $VO_2$  is the amount of pure gaseous oxygen consumed per unit time,  
1299 and  $C_a$  and  $C_v$  are oxygen content of arterial and mixed venous blood, respectively. Typically,  
1300  $VO_2$  is measured using a spirometer, while  $C_a$  and  $C_v$  require catheters to be inserted into the  
1301 patient.  $C_v$  is measured from the pulmonary artery or vena cava, while  $C_a$  is often measured from  
1302 the brachial or femoral artery<sup>180</sup>.

1304 While Fick's method can be highly accurate, in the range of 5 to 10%<sup>180</sup>, and is often used as  
1305 a benchmark for other methods, it is highly invasive and requires catheterization. Furthermore, to  
1306 take accurate readings, the patient's cardiac output and oxygen consumption must be stable for  
1307 several minutes at a time<sup>180</sup>. It is also inconvenient for infants, or during surgery, because a  
1308 sufficient blood volume is required for this technique<sup>180</sup>.

1310  
1311 (b) Indicator dilution techniques

1312 Indicator dilution is a variation of the Fick principle and works in a similar way. Rather than  
1313 using oxygen as an indicator, other indicators can be injected into the bloodstream at a single point,  
1314 and their concentration is analyzed downstream. The most common indicators used in dilution are  
1315 indocyanine green dye (dye dilution), or cold saline (thermodilution).

1316 In the case of dye dilution, the dye concentration is measured using a densitometer, based on  
1317 the optical density of the blood. This is then plotted over time, and the area under the curve can be  
1318 related to the cardiac output and the amount of dye initially injected using the Stewart-Hamilton  
1319 equation<sup>198</sup>:

$$CO = \frac{V_{indicator}}{\int_0^{\infty} C(t) dt} \quad (26)$$

1323 where the numerator is the initial amount of indicator injected, and  $C(t)$  is the concentration of  
1324 the indicator measured downstream over time.

1326

1327 In reality, because the dye is not removed from the bloodstream by the kidneys sufficiently  
1328 fast, the concentration curve peaks multiple times as the dye recirculates<sup>180</sup>. Therefore, the curve  
1329 must be extrapolated so that it returns to zero concentration.

1330

1331 For thermodilution, the Stewart-Hamilton equation is modified to account for the heat transfer  
1332 between blood and saline<sup>180,198</sup>:

1333

$$1334 \quad CO = \frac{K * V_{indicator} * (T_{blood} - T_{indicator})}{\int_0^{\infty} T_{measured}(t) dt} \quad (27)$$

1335

$$1336 \quad K = \frac{c_{indicator} \rho_{indicator}}{c_{blood} \rho_{blood}} \quad (28)$$

1337

1338 where  $c$  is the specific heat,  $\rho$  is the density,  $V_{indicator}$  is the volume of indicator initially  
1339 injected,  $T_{blood}$  and  $T_{indicator}$  are the initial temperatures of the blood and indicator, respectively,  
1340 and  $T_{measured}(t)$  is the temperature measured downstream over time.

1341

1342 The injected saline lowers the temperature of the blood as it travels through the bloodstream,  
1343 followed by warming as it is mixed and diluted in the blood. This is measured using a thermistor.

1344

1345 Indicator dilution is unsuitable for continuous monitoring as the temporal resolution is too low.  
1346 One must wait for roughly 1 minute for the indicator to circulate and fully dilute<sup>180</sup>. In addition,  
1347 the densitometer requires a lengthy calibration process<sup>180</sup>. Unlike the Fick method, there is no self-  
1348 sustaining constant flux of indicator, so periodic reinjection is required. Over time, this can  
1349 increase the risk of embolism, infection, and fluid imbalances<sup>180</sup>.

1350

1351 These methods can also be error-prone. For example, thermodilution techniques will have  
1352 limited accuracy given unstable body temperature, but this may be uncontrollable in certain cases,  
1353 like liver transplantation surgery<sup>199</sup>. In addition, arterial pulse waves could also be transferred to  
1354 cardiac measurements, but this is also unreliable for monitoring on trends because it cannot  
1355 compensate for circulatory changes. Also, the Stewart-Hamilton model itself assumes ideal fluid  
1356 flow. Many of the assumptions of ideal fluid flow are violated by the human circulatory system,  
1357 such as single inflow and single outflow tracts, complete mixing of the fluids, steady flow, and no  
1358 recirculation of indicator<sup>198</sup>.

1359

1360 Additionally, in dye dilution, the downslope of the concentration curve must be extrapolated  
1361 extensively due to recirculation of the dye, limiting the accuracy. In thermodilution, one must  
1362 carefully maintain the temperature of the injectate, or else it may cause the temperatures to deviate.  
1363 Thermodilution is also unreliable in low cardiac output situations, where it tends to overestimate

1364 the cardiac output. Under low-flow conditions, the indicator has more time to equilibrate with the  
1365 surrounding tissues, leading to diminished measured temperature changes and a smaller area under  
1366 the curve<sup>200</sup>, because heat exchange is assumed to only occur between blood and saline.

1367

1368 (c) Conductance catheterization

1369 In conductance catheter measurements, a catheter with multiple electrodes segmented along  
1370 its length is inserted into the left ventricular chamber. The blood within the chamber is segmented  
1371 into different volumes stacked together, with their boundaries defined by the left ventricular wall  
1372 and the equipotential surfaces through the electrodes<sup>201</sup>. Using the dielectric and conductive  
1373 properties of the blood, each separate volume of blood can then be treated as a resistor and  
1374 capacitor in parallel<sup>201</sup>. The height is the distance between electrodes. The cross-sectional area is  
1375 the cross-sectional area of the blood inside the left ventricle<sup>201</sup>. This cross-section varies over time  
1376 throughout the cardiac cycle. The conductance,  $1/R$ , can be modeled by<sup>201</sup>:

1377

$$\frac{1}{R(t)} = \frac{\sigma V(t)}{L^2} \quad (29)$$

1378

1379 where  $\sigma$  is the conductance of the blood,  $V$  is the volume of the segment, and  $L$  is the length  
1380 between electrodes. From there, the volumetric contribution of each segment to the stroke volume  
1381 can be found<sup>201</sup>:

1382

$$\Delta V = \frac{L^2}{\sigma} \left( \frac{1}{R_{be}} - \frac{1}{R_{ee}} \right) \quad (30)$$

1383

1384 where  $R_{be}$  and  $R_{ee}$  are the resistances at the beginning and end of ejection, respectively.

1385

1386 The summation of each segment then gives the total stroke volume, and from there, ejection  
1387 fraction and cardiac output may also be determined.

1388

1389 This method has the disadvantage of being highly invasive, requiring catheterization of the  
1390 left ventricle. The conductivity of blood must also be calibrated. This can lead to errors, as the  
1391 conductivity of blood changes throughout the cardiac cycle (see the Bioimpedance section). The  
1392 model also assumes the equipotential surfaces to be parallel and the blood in the ventricle to be  
1393 the only conducting objects, which may deviate from the real situation<sup>201</sup>.

1394

1395 (d) Radionuclide angiography

1396 Traditionally, gamma cameras used in radionuclide angiography were too slow to perform  
1397 continuous monitoring of left ventricular volume, ejection fraction, and cardiac output. However,  
1398 now there are small and lightweight scintillation probes, which can perform radionuclide  
1399

1400

1401 angiography right at the bedside. A radionuclide indicator is injected into the circulation, and the  
1402 radionuclide count density is measured throughout the cardiac cycle<sup>202,203</sup>. The maximum count  
1403 density throughout the cycle represents end-diastole, while the minimum represents end-systole<sup>202</sup>.  
1404 In this way, the ejection fraction may be determined with the following equation<sup>202,203</sup>:  
1405

1406 
$$EF = \frac{\text{end diastolic counts} - \text{end systolic counts}}{\text{total diastolic counts} - \text{background counts}} \quad (31)$$

1407  
1408 Count averaging is used (roughly 5 heartbeats) to increase the reliability of the measurement and  
1409 raise the count density<sup>202</sup>. The drawback of this approach is namely the ionizing radiation, which  
1410 is safe in shorter timeframes, but unsuitable for extended monitoring. Because count averaging is  
1411 used, irregular activities such as fibrillation or ectopic activities can affect the accuracy<sup>202</sup>.  
1412

1413 (e) Velocity measurements

1414 Cardiac output can also be found by measuring the blood velocity at a vessel, while knowing  
1415 its diameter. Ways of measuring the blood velocity include Doppler ultrasound and  
1416 electromagnetic flow probes. In Doppler ultrasound, the changes in the signal frequency are related  
1417 to the blood flow velocity<sup>26</sup>:  
1418

1419 
$$\frac{Fd}{Fs} = \frac{u}{x} \quad (32)$$

1420  
1421 where  $Fd$  is the frequency shift,  $Fs$  is the source frequency,  $u$  is the velocity, and  $x$  is the sound  
1422 speed. Thus, by measuring the frequency shift, the flow velocity can be measured.  
1423

1424 In electromagnetic flow probing, a probe is implanted and slipped around a blood vessel.  
1425 According to Faraday's law of magnetic induction, a conductor (i.e., the blood in this case) moving  
1426 through a magnetic field generates a voltage that is proportional to the velocity<sup>180</sup>:  
1427

1428 
$$e = BLu \quad (33)$$

1429  
1430 where  $e$  is the induced voltage,  $B$  is the magnetic flux density,  $L$  is the spacing between  
1431 electrodes, and  $u$  is the flow velocity.  
1432

1433 Velocity measurements must first be calibrated by measuring the blood vessel diameter before  
1434 it can be converted to cardiac output<sup>192</sup>. In the case of Doppler, the angle of the probe to the blood  
1435 flow must additionally be identified<sup>180</sup>. While studies have found Doppler to be inaccurate in  
1436 measuring cardiac output, especially in children, its strength is in monitoring the trends and its  
1437 capability of detecting rapid changes<sup>192</sup>. This makes it useful for monitoring surgical or fluid



1438 administration procedures in clinical settings. In addition, Doppler is one of the few non-invasive  
1439 methods that measure cardiac output.

1440

1441 Electromagnetic flow probes face significant drawbacks in that they require the blood vessel  
1442 to be fully exposed through surgery such that the probe can be positioned around the blood  
1443 vessel<sup>180</sup>. The accuracy of this method also depends strongly on how well the surgical exposure is  
1444 done<sup>180</sup>. Overall, it is an unfavorable method in most situations.

1445

1446 (f) Pulse contour analysis

1447 In pulse contour analysis, the arterial pulse wave is recorded to produce a measurement of  
1448 cardiac output. The area under the pulse wave curve is related to the stroke volume, and therefore  
1449 the area under the curve times the heart rate can be related to the cardiac output<sup>192</sup>. To derive the  
1450 relationship for reliable monitoring, a three-element Windkessel model of the aorta's mechanical  
1451 characteristics and the peripheral resistance of the body was used to represent the circulation<sup>192,193</sup>.  
1452 To calibrate the model, the relationship between the aortic pressure and cross-sectional area must  
1453 be derived, so that the vessel compliance can be estimated<sup>193</sup>. Studies have also further developed  
1454 the model to be able to identify the stressed and unstressed states of the left ventricle and  
1455 additionally calculate the ejection fraction<sup>204</sup>.

1456

1457 Due to the significant amount of calibrations required for this approach, the accuracy is limited.  
1458 In addition, as with most models, ideal conditions must be satisfied for the model to work well.  
1459 Indeed, current commercial devices for measuring cardiac output via pulse contour analysis  
1460 demonstrate a lack of ability to properly account for peripheral circulatory changes<sup>192</sup>. The pulse  
1461 contour analysis method can be unreliable during surgeries, such as during liver transplantation,  
1462 where cirrhosis patients have high cardiac output and low fluctuating peripheral resistance<sup>192</sup>.

1463

1464 (g) Bioimpedance

1465 Bioimpedance techniques relate the changes of electrical impedance across the thorax to the  
1466 cardiac cycle to monitor the cardiac performance. Bioimpedance is also one of the few non-  
1467 invasive techniques for monitoring cardiac output. Classical methods of processing the impedance  
1468 signals were dubious in their accuracy and whether they measured the blood flow of the heart at  
1469 all<sup>192</sup>. Patients with conditions such as pulmonary edema, where excessive lung water was present,  
1470 repeatedly had poor results in validation studies of bioimpedance<sup>192</sup>.

1471

1472 Recently, more reliable methods of processing the bioimpedance signals have been developed.  
1473 Electrical velocimetry is based on the idea that red blood cells are randomly oriented when there  
1474 is no blood flow in the aorta, and subsequently become aligned when the aortic valve opens. This  
1475 alignment produces a change in the conductivity of the blood.

1476

1477 The overall bioimpedance measured can be modeled with the following equation:

1478

1479 
$$Z(t) = Z_0 + \Delta Z_R + \Delta Z_C \quad (34)$$

1480

1481 where  $Z_0$  is the quasi-static background impedance,  $\Delta Z_R$  is the artifact from respiration, and  $\Delta Z_C$   
1482 is the impedance change due to the cardiac cycle.

1483

1484 From the impedance curve of  $\Delta Z_C$ , one can determine the acceleration of the blood flow based  
1485 on the time taken to align the red blood cells. An average velocity can then be estimated and  
1486 converted to stroke volume and cardiac output based on body mass.

1487

1488 In adults, electrical velocimetry is just within the 30% limits of agreement<sup>205</sup>, but is not reliable  
1489 in children, likely due to the body mass-based assumptions<sup>192</sup>.

1490

1491 In summary, these methods tend to have several sources of error due to their reliance on  
1492 models and assumptions. The lack of imaging-derived left ventricular volume measurements  
1493 causes them to be reliable only under ideal conditions and to include extraneous signal sources in  
1494 their measurements. The use of imaging is not viable in long-term continuous monitoring either,  
1495 with the currently available devices. Non-imaging techniques can monitor for slightly longer  
1496 periods of time, but are generally too invasive and inconvenient, with many requiring  
1497 catheterizations and injections, cannot be used in everyday life or during exercise, and are also not  
1498 viable solutions for long-term monitoring. In addition, those invasive approaches require expertise  
1499 in the placement and manipulation of the catheters to get the correct results. Only well-trained  
1500 clinicians can handle this measurement modality<sup>97</sup>. As a result, many of these techniques are  
1501 typically only used within the intensive care unit or during an operation, where their benefits  
1502 sufficiently outweigh the drawbacks. Thus, there is a significant technological gap that can be  
1503 filled by a wearable, versatile, and non-invasive imager that can do direct imaging-derived  
1504 measurements of the left ventricular volume.

1505

## 1506 9.5 Anatomical considerations of imaging posture

1507 In the apical four-chamber view, we could only collect data during recovery but not during  
1508 exercise (Fig. 5). This is not to do with a technological limitation, but rather an intrinsic anatomical  
1509 fact. Extended Data Fig. 4 has shown that the apical four-chamber view is best captured in the  
1510 lying side position, which has limited the continuous monitoring during exercise. From our  
1511 supplementary data (Supplementary Fig. 28) and literatures<sup>206,207</sup>, it is generally accepted that the  
1512 apical four-chamber view is best captured in the lying side position and will be partly  
1513 blurred/blocked in other positions. The lying side position is the clinically required position to  
1514 obtain a qualified apical four-chamber view<sup>206,207</sup>.

1515

1516 The positional requirements for the apical four-chamber view are very strict for two reasons.  
1517 First, only when the patient is in the lying side position does the ultrasound beam enter the heart's  
1518 apex at a straight angle (Supplementary Fig. 28). Other positions (e.g., standing) will yield  
1519 incorrect measurements of chamber dimensions and thus cardiac indices.

1520  
1521 Second, we compared the apical four-chamber images from a commercial imager taken by an  
1522 experienced cardiologist and from a wearable imager taken by a trained amateur, both with the  
1523 subject in the standing position (Supplementary Fig. 28). The cardiac chamber morphologies  
1524 cannot be fully reconstructed in either image. The right ventricle and right atrium have been totally  
1525 shadowed by the lungs. While we can roughly see the morphology of the left ventricle and left  
1526 atrium, the image quality is poor. The left ventricular endocardium cannot be visible, and the left  
1527 atrium is malformed, because part of the ultrasound array has been blocked by the lungs and only  
1528 a small fraction of the elements play an effective role in the imaging process<sup>207</sup> (Supplementary  
1529 Fig. 28). It results in images with low spatial-resolutions and low contrast-to-noise ratios.

1530  
1531 On the contrary, lying in the lying side position brings the relative orientations of the heart  
1532 and the transducer array out of the lung shadow. Therefore, the inability to collect high-quality and  
1533 morphologically representative apical four-chamber images in the standing position is more of an  
1534 intrinsic anatomical fact rather than a limitation of the commercial imager or the wearable imager.  
1535 Thus, we imaged the heart in the apical four-chamber view only with the lying side position.

1536  
1537 However, the apical four-chamber view is not the only source of information in  
1538 echocardiography. We have also presented continuous monitoring of the parasternal long axis view  
1539 throughout the whole process (before exercise, during exercise, and during recovery; Fig. 4), as  
1540 the anatomy does not limit this view as strictly as it does for the apical four-chamber view. The  
1541 M-mode recording in Figure 4b is extracted from the B-mode recording. Extended Data Fig. 5  
1542 shows that the patch is capable of taking B-mode images during exercise and illustrates how the  
1543 M-mode is extracted. The chamber motion is noticeable, and the change of heart rate is also  
1544 computed in Figure 4c. Abundant information, such as left ventricular internal diameter end  
1545 diastole/systole, the fractional shortening ratio, and the anatomic integrity of the left ventricle are  
1546 also determined. In addition, Figure 4d and Figure 4e are presenting the details from different  
1547 stages, demonstrating the capability of wearable imager in the continuous monitoring during  
1548 exercise.

1549  
1550 In addition, monitoring the cardiac status can be valuable during many surgeries and other  
1551 interventions to prevent further complications<sup>208</sup>. Given that the lying side position is the standard  
1552 position during the echocardiography measurement for ejection fraction, our device can be directly  
1553 applied to numerous situations where monitoring of cardiac function is essential and lying side  
1554 position is easy to reach. For example, during general anesthesia as well as the postoperative period,

1555 there is always the risk of cardiac events for patients who undergo noncardiac surgeries, such as  
1556 myocardial infarction and heart failure<sup>208-212</sup>. Therefore, the monitoring of the cardiac function is  
1557 valuable in this context especially for the patients with risk factors<sup>208</sup>. During the beginning of  
1558 general anesthesia, the lying side position can be easily reached, thus providing a preliminary  
1559 evaluation of the cardiac function preoperatively with our device.

1560

1561 In this work, two-dimensional cardiac images can generate an approximate left ventricular  
1562 volume by the Modified Simpson's rule, which is widely accepted in clinical diagnosis even  
1563 though it comes with approximation and inaccuracy. Future work can follow up on developing  
1564 solutions for imaging in the parasternal long axis view during exercise/stress testing. For example,  
1565 we can fabricate a 2D matrix probe to reconstruct images three-dimensionally. The cardiac volume  
1566 and other related parameters can be directly and more accurately computed from three-  
1567 dimensionally reconstructed images.

1568

### 1569 **Supplementary Discussion 10: Detailed left ventricle working processes**

1570

1571 A new cardiac cycle starts from the end of left ventricular relaxation in the last cycle. When  
1572 the pressure in the left ventricle drops below that in the left atrium, the pressure difference pushes  
1573 the mitral valve to open, so blood flows from the left atrium to the left ventricle. The inflow of  
1574 blood triggers the first volume increment of the left ventricle, which is called rapid inflow. The  
1575 blood inflow builds up the pressure in the left ventricle and at the same time releases the pressure  
1576 in the left atrium. As the pressure difference decreases and the inflow rate slows down, the volume  
1577 of the left ventricle hits the first equilibrium, and the mitral valve tends to close. This period is the  
1578 interval between passive blood flow and active blood flow caused by atrium contraction, which is  
1579 named diastasis. Afterward, the left atrium starts to contract to build the second pressure difference.  
1580 The pressure difference again enforces the mitral valve to open and causes the second stage of  
1581 blood inflow to the left ventricle. Simply, the process of this pressure generation is called atrial  
1582 systole or atrial contraction. At the end of this process, the volume of the left ventricle reaches its  
1583 peak as the second equilibrium.

1584

1585 Then, the left ventricle starts to contract to raise the pressure inside. Because the mitral valve  
1586 and aortic valve keep closed during the contraction, the volume of the left ventricle holds.  
1587 Therefore, this contraction is called isovolumetric contraction. The mitral valve is a one-way valve,  
1588 so there is no blood countercurrent back into the left atrium and only the aortic valve opens after  
1589 the isovolumetric contraction. The blood in the left ventricle is then ejected into the aorta, which  
1590 is called rapid ejection. The rapid ejection results in an obvious drop in the left ventricular volume  
1591 and pressure so there is a sharp slope in the curve. Like the rapid inflow, as the pressure difference  
1592 between the aorta and left ventricle vanishes, the aortic valve closes. Following the ejection, a  
1593 small portion of blood in the left ventricle remains. Because the aortic valve is also a one-way

1594 valve to keep the unidirectional blood flow, the left ventricular volume keeps stable during  
1595 relaxation, which is also named isovolumetric relaxation. At the end of the isovolumetric  
1596 relaxation, next cardiac cycle commences.

1597

1598 The precise monitoring of cardiac events can provide more insights into pathologies of cardiac  
1599 dysfunctions. For example, the ejection rate based on the volume curve can reveal the myocardium  
1600 contractility and stenosis of aortic valves.

1601

## 1602 **Supplementary Discussion 11: Neural network for continuous ultrasound imaging**

1603

### 1604 11.1 Developing the deep learning model

1605 We surveyed different deep learning models in the literature and made the selection based on  
1606 their popularity and relevance to this study. Currently, widely-adopted image segmentation deep  
1607 learning models can be classified into two categories: U-Net models, which are known for fast and  
1608 precise biomedical image segmentation with multiple variants<sup>213</sup>, and Fully Convolutional  
1609 Networks (FCN) models, an end-to-end deep learning method, which first uses a series of fully  
1610 connected convolutional layers to find useful features from the input image and then use an  
1611 upsampling layer to restore the output image size to the same as the input image size<sup>214</sup>.

1612

1613 Specifically, U-Net models are based on the well-established U-Net architecture for fast and  
1614 precise biomedical image segmentation<sup>213</sup>. U-Net architecture<sup>213</sup> has gained wide adoption. Many  
1615 researchers have proposed variant models based on the U-Net architecture. In this study, in  
1616 addition to the original U-Net model, we also worked with its variants, including Attention-U-Net  
1617 (U-Net model with an attention gate)<sup>215</sup>, U-Net++ (U-Net with redesigned skip pathways, dense  
1618 skip connections, and deep supervision)<sup>216</sup>, NAS-UNet (Neural Architecture search with a U-Net  
1619 architecture)<sup>217</sup>, U-Net+ResNet50 (U-Net with ResNet encoders)<sup>218</sup>, and U-Net mini (a simplified  
1620 structure of the original U-Net<sup>219</sup>).

1621

1622 The FCN model is widely used for semantic segmentation<sup>214</sup>. FCN gained wide adoption for  
1623 its outstanding performance and no restriction on the input image size. Specifically, an FCN model  
1624 first uses a series of fully connected convolutional layers to find useful features from the input  
1625 image and then uses an upsampling (backwards strided convolution) layer to restore the output  
1626 image size to the same as the input image size. If we return the output directly after solely using  
1627 the upsampling layer, we call the network FCN-32 based on the number of upsampling operations.  
1628 It is believed that spatial location information could be lost when going deep in the neural network.  
1629 One solution for this is to fuse the predictions of multiple stages of the convolution layers. FCN-  
1630 8, for example, fuses the predictions of the final three layers, and therefore only needs to upsample  
1631 for eight times. Unless otherwise specified, all of our models used vanilla encoder as auto-encoder.

1632 We also experimented with other types of auto-encoders, such as VGG and ResNet, in which cases  
1633 we specify the auto-encoder names in the model name.

1634

1635 To ensure accuracy of the pre-processing of input images, we performed frame-level  
1636 segmentation/labelling of the left ventricle under the guidance of a cardiologist, and followed the  
1637 Modified Simpson’s rule<sup>220</sup> for volume calculation. For the commercial imager, we collected  
1638 totally 500 frames on static subjects, 221 out of which are manually labelled for training. For the  
1639 wearable imager, we collected overall 500 frames on the static subjects and 5858 frames on the  
1640 moving subjects, 201 and 2029 out of which, respectively, are manually labelled for training.

1641

1642 We used data augmentation techniques to expand the limited labelled dataset. We applied  
1643 rotation, scaling, and gaussian noise to the data to augment the dataset. Specifically, we generated  
1644 four additional images for each of the labelled images by rotating the original data  
1645 clockwise/counterclockwise by 5 degrees, rescaling it by a factor of 1.2, and applying gaussian  
1646 noise to it. The results indicated that the data augmentation slightly improved the performance of  
1647 the deep learning model (Supplementary Fig. 27).

1648

1649 We evaluated the models’ performance quantitatively using Mean-Intersection-Over-Union  
1650 (mIoU), which is one of the most widely used evaluation metrics for benchmarking object  
1651 detection<sup>221</sup>. Specifically, intersection-over-union (IoU) is used to compare the similarity between  
1652 two shapes<sup>221</sup> and is calculated using:

1653

$$1654 \quad IoU = \frac{\textit{Area of intersection}}{\textit{Area of union}} \quad (35)$$

1655

1656 The mIoU is then calculated by taking the mean of IoU for all images in a dataset. In this study,  
1657 we calculated mIoU by taking the mean of IoU of each pair of the deep learning model predicted  
1658 image segmentations and the manually labelled image segmentations. Specifically, for each  
1659 “(predicted-image, labelled-image)” pair, its IoU equals to the number of pixels within the left  
1660 ventricle in both images divided by the total number of unique pixels within the left ventricle by  
1661 either of the two images. The evaluation results for different models are listed in Supplementary  
1662 Fig. 26 and Supplementary Table 5.

1663

1664 During exercise, small amounts of the recorded B-mode images were corrupted when the heart  
1665 was blocked by the deep-breathing lung. To solve this problem, we applied an imputation  
1666 algorithm to complement the missing parts in these corrupted images to generate a continuous  
1667 waveform (Supplementary Fig. 29).

1668

1669 11.2 Detailed analysis of the neural network

1670 Wearable sensors can generate continuous images. A milestone in the roadmap of developing  
1671 wearable sensors is to integrate deep-learning algorithms to process the continuous images  
1672 automatically. There are some commercial systems<sup>91</sup> and research studies<sup>3,90</sup> on developing  
1673 algorithms or deep-learning models for quick calculation of ejection fraction and cardiac output,  
1674 but the data output is still discontinuous because the commercial probe needs to be operated  
1675 manually and can only produce intermittent data points. Integrating the wearable patch with deep-  
1676 learning models can continuously output a large amount of actionable information and clinical  
1677 insights, which have not been achieved in the literature.

1678

1679 For the deep learning component, our primary goals are (1) to identify image segmentation  
1680 models to automatically extract the left ventricular volume from B-mode images; (2) to integrate  
1681 the best-performing models in our research settings and analyze their performance. In the  
1682 following sections, we provide more analysis and discussions about training paradigm comparison  
1683 and model selection, data collection and processing (containing sample sizes), model  
1684 implementation and parameter tuning strategy (containing learning rate), model performance, and  
1685 future directions.

1686

1687 (1) Training paradigm comparison and model selection

1688 Researchers have made tremendous progresses in improving automatic image segmentation  
1689 using various types of machine learning models in recent years. Most researchers focused on using  
1690 supervised learning models<sup>222,223</sup>, which are models that learn from a training dataset with “correct”  
1691 ground-truth labels. Many researchers have reported promising results using supervised learning  
1692 models for medical image segmentation<sup>3,223</sup>. Although supervised learning models achieve high  
1693 accuracy in image segmentation tasks, their weakness is in the expensive training cost because  
1694 they acquire the training set through manual labeling in most cases.

1695

1696 In this study, we mainly focused on integrating supervised deep learning models into our  
1697 research settings because segmentation results with a high accuracy are a prerequisite for  
1698 extracting accurate cardiac performance metrics from the images. The weakness of supervised  
1699 learning can be considerably mitigated by few-shot learning and reinforcement learning (detailed  
1700 discussions are provided in future directions below). Among various supervised learning image  
1701 segmentation models, those gaining the most popularity<sup>224</sup> are Convolutional Neural Networks,  
1702 which are deep learning models that directly learn from raw pixel data by adaptively assigning  
1703 weights to different areas/pixels of the input<sup>225</sup>. Specifically, in the field of medical image  
1704 segmentation, fully Convolutional Neural Networks have achieved superior results compared to  
1705 traditional Convolutional Neural Networks models in many studies<sup>213</sup>. Therefore, we chose to  
1706 work with different variations of FCN models and U-Net models that are fully Convolutional  
1707 Neural Networks performing particularly well within medical research settings<sup>222,223,226</sup>. We have

1708 discussed each of the specific variations of these models in the Methods and Supplemental  
1709 Information.

1710

1711 (2) Data collection and processing

1712 The deep learning models in this work were implemented with readable, consistent, and well-  
1713 structured codes, high-quality datasets, and reproducible results. The sample size is listed in  
1714 Supplementary Table 4. All data were used by all models. Notably, we worked with two types of  
1715 datasets in this study. The first type was “static” datasets, which contained left ventricle ultrasound  
1716 B-mode images we collected from static subjects. The second type was “after exercise” datasets,  
1717 which contained left ventricle ultrasound B-mode images we collected from subjects after intense  
1718 physical exercise. The “after exercise” datasets were more challenging to process because (1) the  
1719 size of the left ventricle was continuously and rapidly changing, leading to a higher variability in  
1720 the dataset; (2) it contained noisier images, in which the left ventricle was sometimes blocked by  
1721 the lung because the subjects were breathing heavily. To the best of our knowledge, this study  
1722 represents the first to continuously segment cardiac ultrasound images with intensively changing  
1723 left ventricular volumes. After collecting the data, we cropped the image size to be  $512 \times 512$   
1724 pixels and manually segmented them to create the ground-truth as the training dataset. Furthermore,  
1725 we used data augmentation techniques such as rotating, scaling, and adding gaussian noises to  
1726 expand the size of the training dataset.

1727

1728 (3) Model implementation and parameter tuning strategy

1729 We implemented the models based on open-source codes listed in Supplementary Table 3.  
1730 The final hyperparameters after careful tuning in this study are also listed in Supplementary Table  
1731 3. Specifically, when training the models, we selected adaptive moment estimation (Adam) as the  
1732 optimizer for all models. We found Adam to be the best optimizer among other optimization  
1733 algorithms because it not only trains the best-performing models but also converges faster and  
1734 requires less time for tuning. As an adaptive optimizer, Adam adaptively changes learning rates  
1735 for different parameters, and, therefore, the models’ performance was not much affected by the  
1736 initial learning rate. Thus, we applied each model implementation’s default learning rate in most  
1737 cases.

1738

1739 Because most of the neural network models in this study were very deep, batch normalization  
1740 was applied to make the networks faster and more stable. Specifically, when training deep neural  
1741 networks, an update in the training process could change parameters in all layers, causing them to  
1742 have different distributions after each update. This makes the optimization process like chasing a  
1743 “moving” target and thus causes the network to become unstable and slow to train. We applied  
1744 batch normalization to solve this problem. Specifically, each Convolutional Neural Network layer  
1745 was connected with a batch normalization layer. The batch normalization layers standardized the  
1746 network layer’s output by applying a transformation that makes each layer’s output mean close to



1747 0 and standard deviation close to 1. This will effectively keep each layer's input distribution  
1748 unchanged, and thus stabilize the network and speed up the optimization process.

1749

#### 1750 (4) Model performance

1751 We have compared the models' performance both quantitatively and qualitatively (Extended  
1752 Data Figs. 6 and 7, and Supplementary Fig. 26). Specifically, we found that images segmented by  
1753 FCN-32 model achieved not only the highest mIoU but also the highest image fidelity. We  
1754 achieved automatic image segmentation using the FCN-32 model.

1755

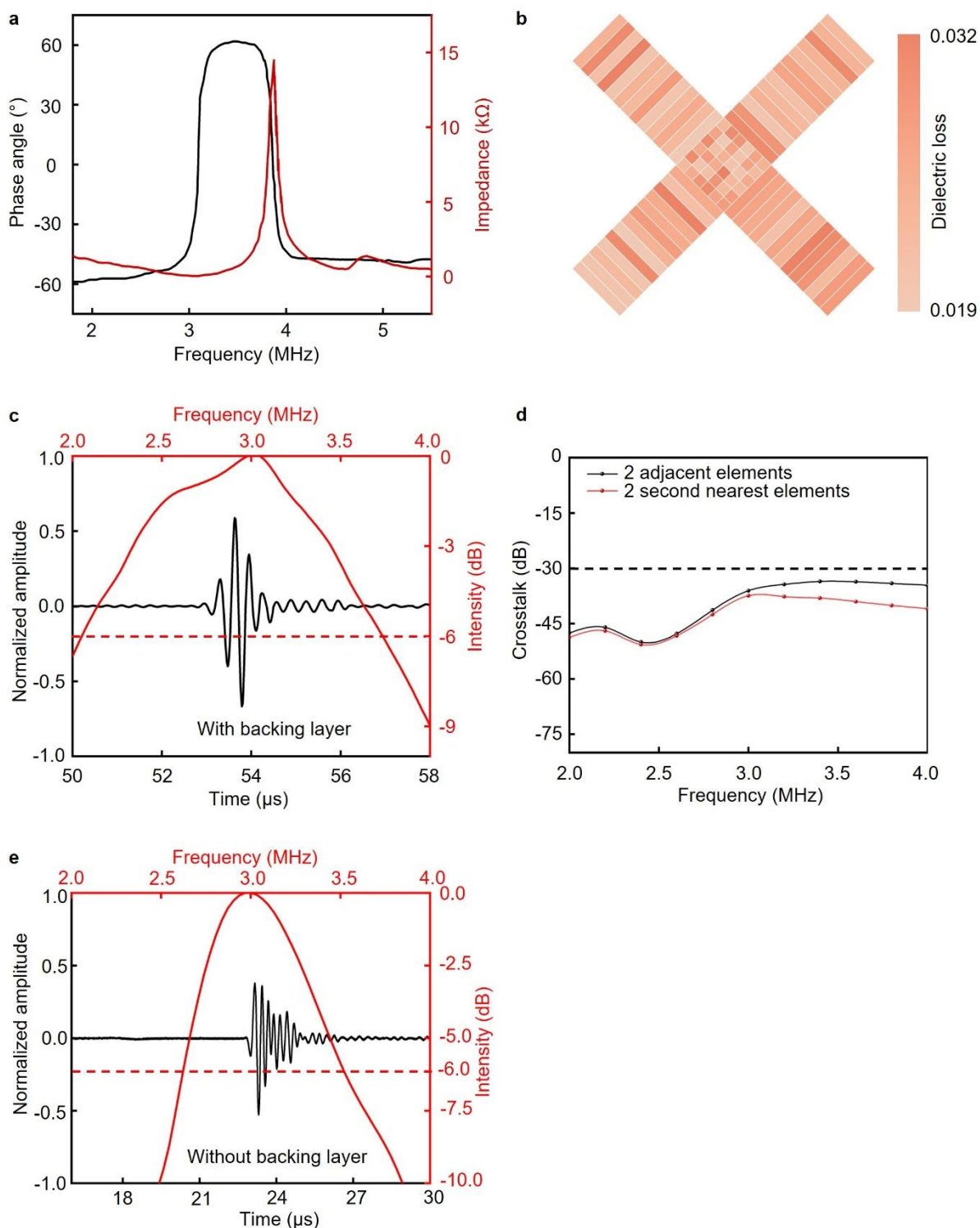
1756 One of the reasons that FCN-32 achieved better results than U-Net models was that FCN-32  
1757 did not have skip-connections. As introduced in the Supplementary Fig. 25, FCN-32's structure  
1758 included a series of fully-connected convolutional layers and a single upsampling layer at the end.  
1759 Compared with FCN models, U-Net models had more upsampling layers and concatenated outputs  
1760 of previous layers using skip connections. Although these differences made U-Net models more  
1761 robust to scale variations, there might be risks that the connections brought back some unnecessary  
1762 features. Because all of our data were of similar scales, the robustness to scale variations was not  
1763 a priority in our dataset. Therefore, the additional robustness brought by the skip-connections in  
1764 U-Net models was unable to make significant improvements to the model. On the other side, the  
1765 skip-connections and additional up-sampling layers possibly brought back redundant features that  
1766 harmed the model's performance. We found FCN models usually output one singular region of  
1767 left ventricle, while U-Net models sometimes output a few small detached external pieces  
1768 (Extended Data Fig. 6). Additionally, the edges of U-Net's segmentations also appeared to be  
1769 "fuzzier" than those of FCN's, proving that FCN was better at removing redundant features  
1770 (Extended Data Fig. 6). Similarly, although the fusing step in FCN-8 could restore some location  
1771 information, it could also bring back redundant information that was already filtered by previous  
1772 layers, and hence made FCN-8's performance slightly worse than FCN-32's.

1773

#### 1774 (5) Future directions

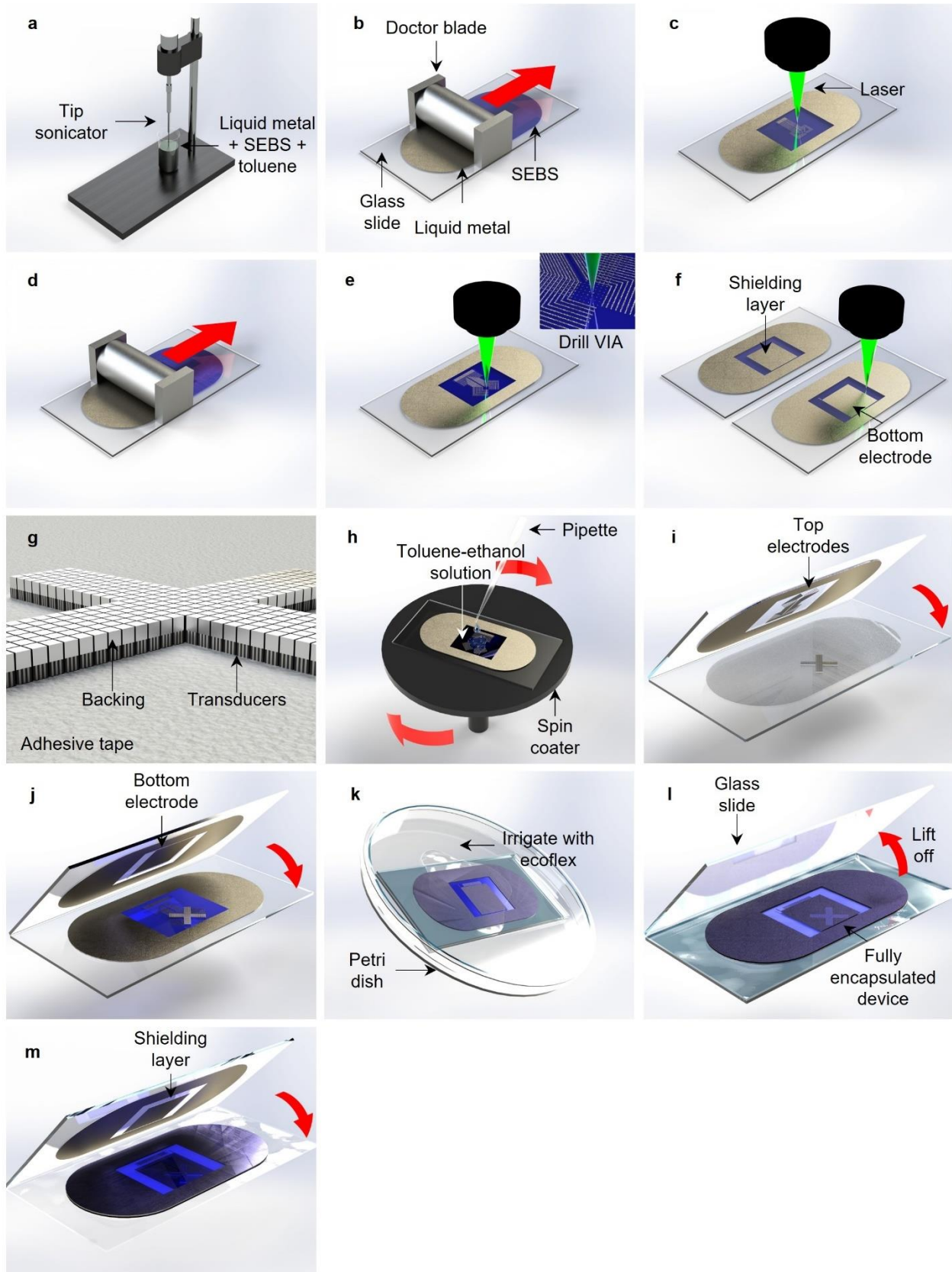
1775 The FCN-32 model with the current dataset was sufficient for image segmentation in this  
1776 study, which facilitated the frame-by-frame output of those cardiac indices. The FCN-32 had good  
1777 generalization capability regarding different left ventricular volumes and different image noise  
1778 levels. As for the application to new transducers and perspective data on new subjects in future  
1779 studies, the generalizability of the current model could be further improved by expanding the  
1780 training dataset or optimizing the network. For example, few-shot learning<sup>49</sup>, an advanced version  
1781 of supervised learning, can achieve promising results with the model trained on only a few labeled  
1782 images for each subject<sup>227</sup>. Using this model, it is easier to expand the cohort size to achieve a  
1783 higher data diversity by collecting images from a small number of subjects. Another potential  
1784 strategy is reinforcement learning<sup>50</sup>, which is another training paradigm alongside supervised  
1785 learning and unsupervised learning. It can optimize models' training and data augmentation

1786 approaches so that those models can be better tuned and less overfitted<sup>226</sup>, thus improving the  
1787 models' generalizability. By integrating those strategies, the FCN-32 model will potentially be  
1788 adapted to a larger population with nosier data.



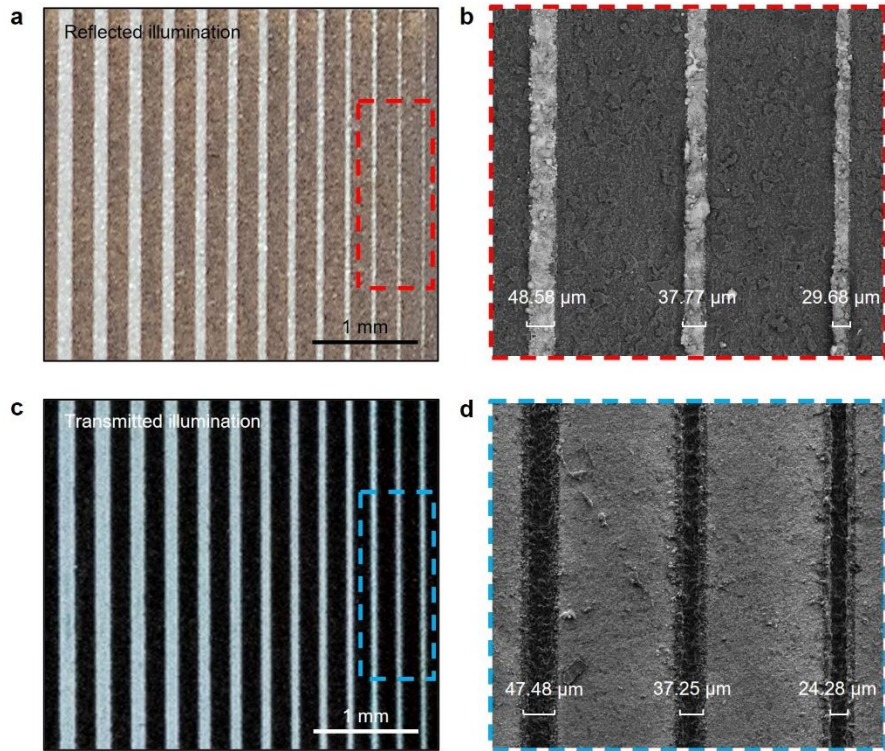
1789 **Supplementary Fig. 1 | Characterization of the transducer array.** **a**, Electrical impedance  
 1790 spectrum with the amplitude and phase angle. It shows the 3 MHz resonance frequency and 3.87  
 1791 MHz antiresonant frequency. The calculated electromechanical coupling coefficient is 0.67. **b**,  
 1792 Map of the dielectric loss of all transducer elements in the orthogonal imager. **c**, The pulse-echo

1793 response and corresponding frequency spectrum of the transducers, showing a wide bandwidth of  
1794 ~55% and a central frequency of 3 MHz. **d**, Crosstalk between a pair of adjacent elements and a  
1795 pair of second nearest neighbors, which is lower than the standard -30 dB indicated by the dashed  
1796 line. **e**, The pulse-echo response and corresponding frequency spectrum of the transducers,  
1797 showing a wide bandwidth of ~30% and a central frequency of 3 MHz.

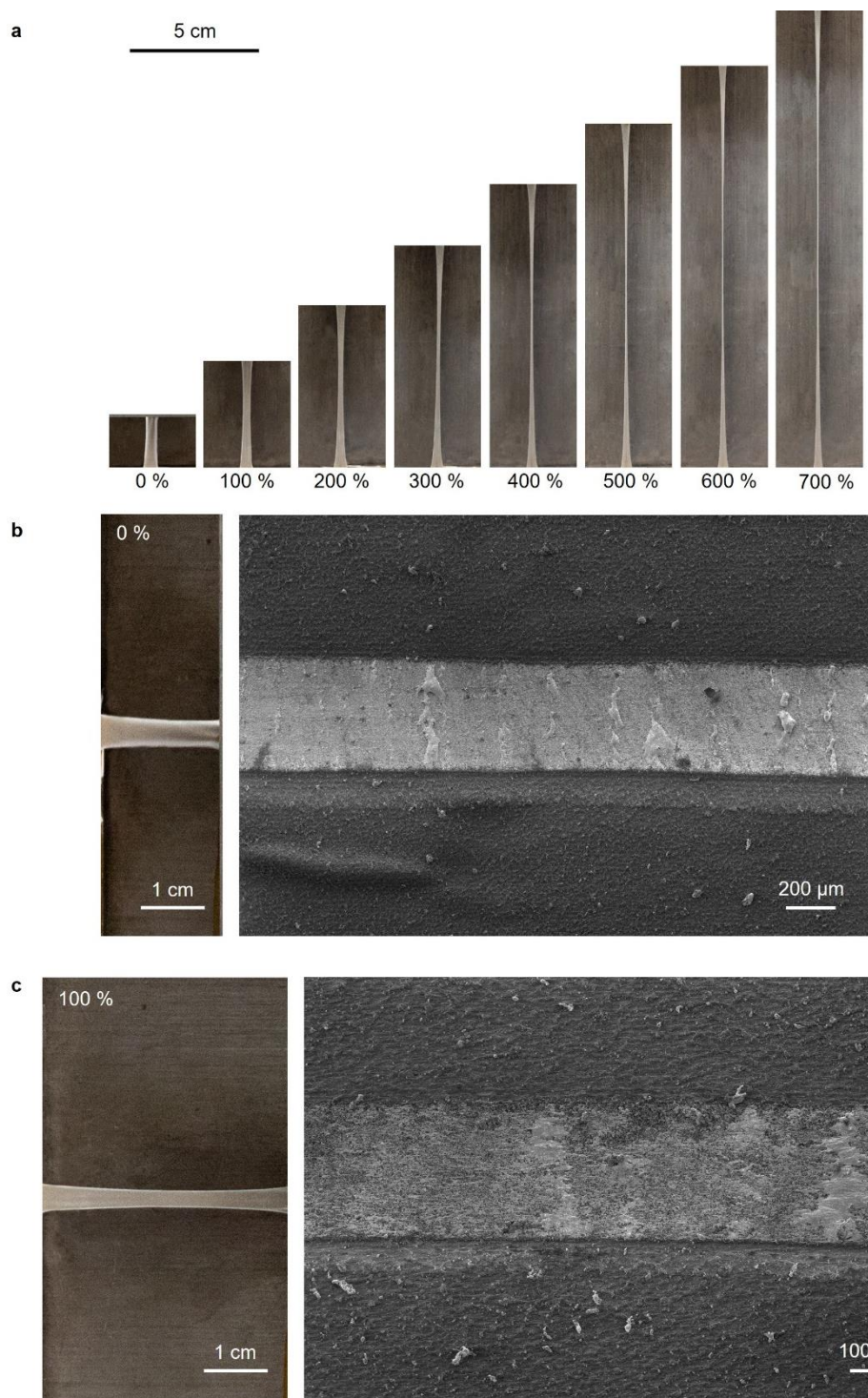


1798 **Supplementary Fig. 2 | Fabrication processes of the wearable imager.** a, Sonicate liquid metal

1799 in toluene with SEBS to homogenize the materials. **b**, Print the liquid metal composite on a SEBS  
1800 substrate using a doctor blade. **c**, Pattern the liquid metal-based composite electrode using laser  
1801 ablation. **d**, Print a subsequent layer of liquid metal insulated with a layer of SEBS on the previous  
1802 electrode. More layers of electrodes can be fabricated by repeating this step. **e**, Drill vertical-  
1803 interconnect-accesses (VIAs) using laser ablation to allow electrical connection between the top  
1804 electrodes and transducers. **f**, Pattern the shielding layer, bottom electrode, and alignment mask  
1805 using laser ablation. **g**, Dice the transducer array together with the backing layer. **h**, Spin coat  
1806 toluene-ethanol solution onto the electrodes to allow adhesion between electrodes and transducers.  
1807 **i**, Bond the top electrodes to the transducer array. **j**, Bond the bottom electrode to the transducer  
1808 array. **k**, Irrigate the gap between the two glass slides with Ecoflex to encapsulate the device. **l**,  
1809 Lift off the glass slides to release the device. **m**, Soften the shielding layer and bond it to the device.

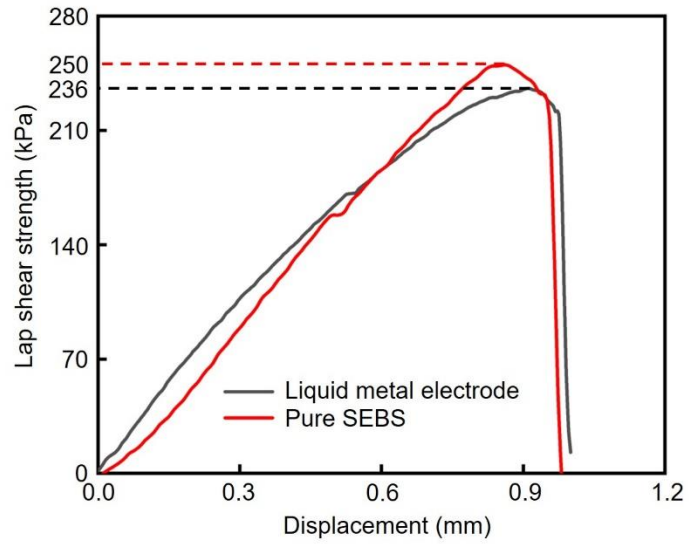




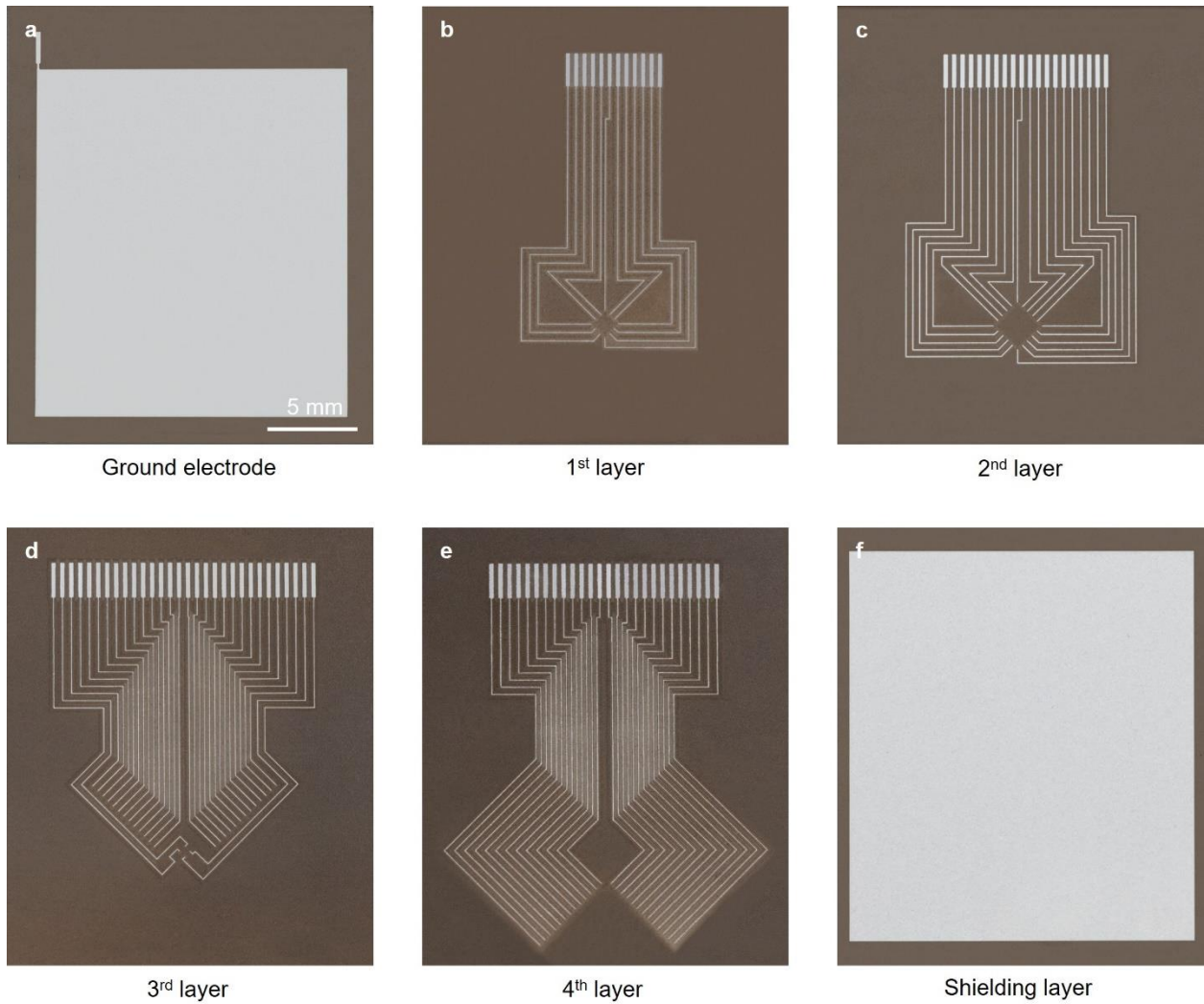


1816 **Supplementary Fig. 4 | Mechanical testing of the liquid metal composite electrodes.** **a**, The  
 1817 high stretchability of the electrodes allows ~700% maximum strain. Optical and scanning electron  
 1818 microscope images of the liquid metal composite electrodes **b**, before and **c**, after uniaxially  
 1819 stretched for 100 % strain. There are no visible cracks in the electrode after stretching, indicating  
 1820 its excellent intrinsic stretchability.

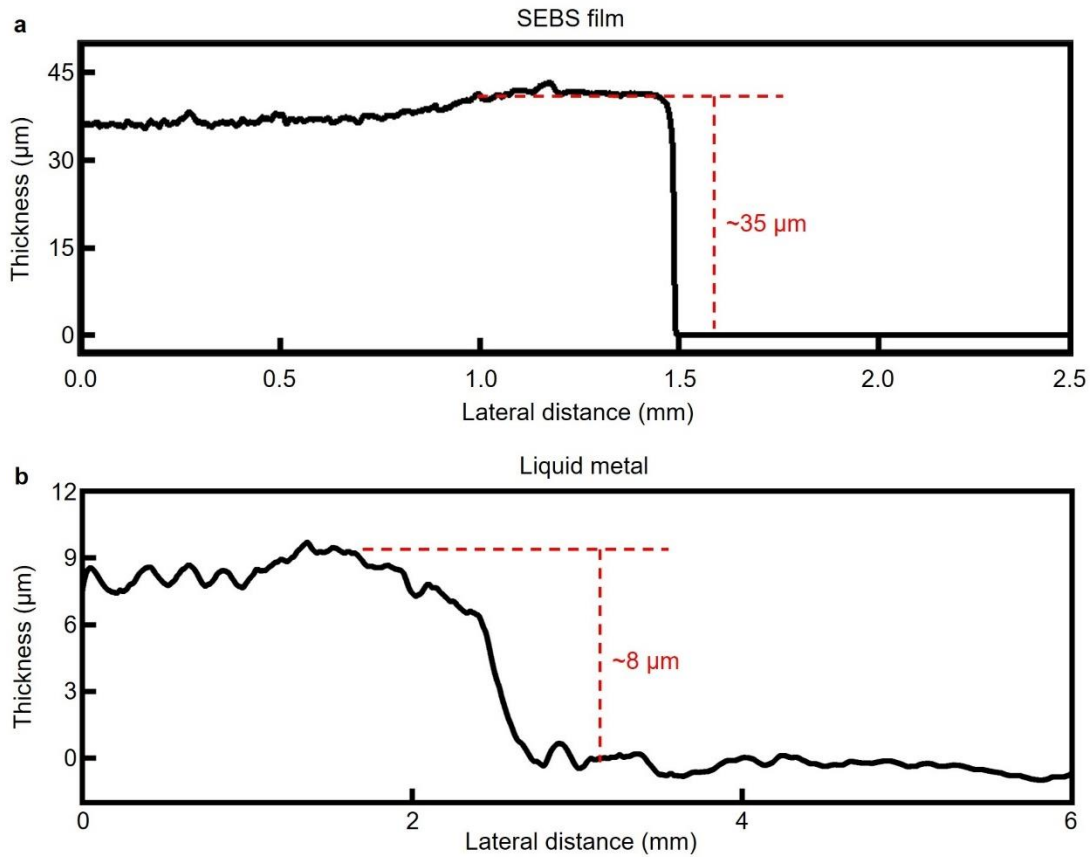




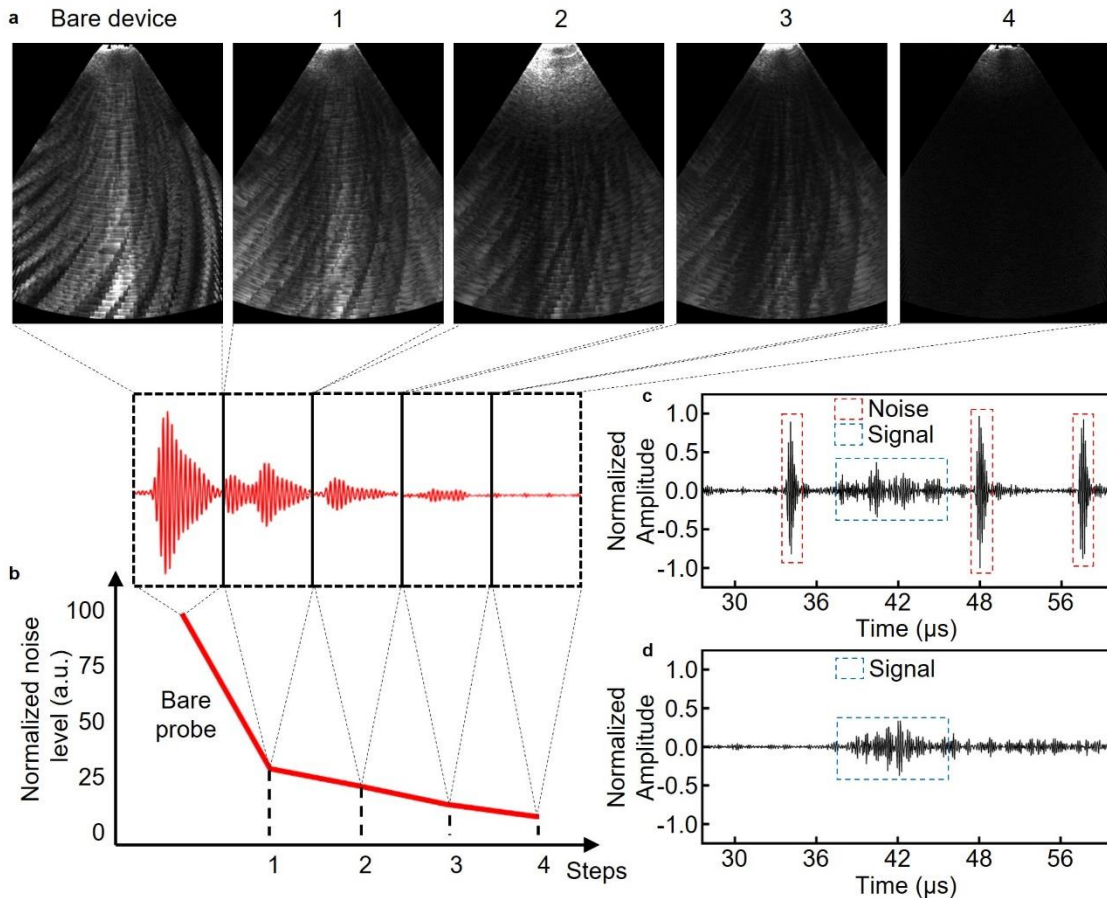
1821 **Supplementary Fig. 5 | Results of lap shear strength tests.** Both liquid metal electrode and pure  
1822 SEBS are characterized. The curves peak values represent the bonding strength.



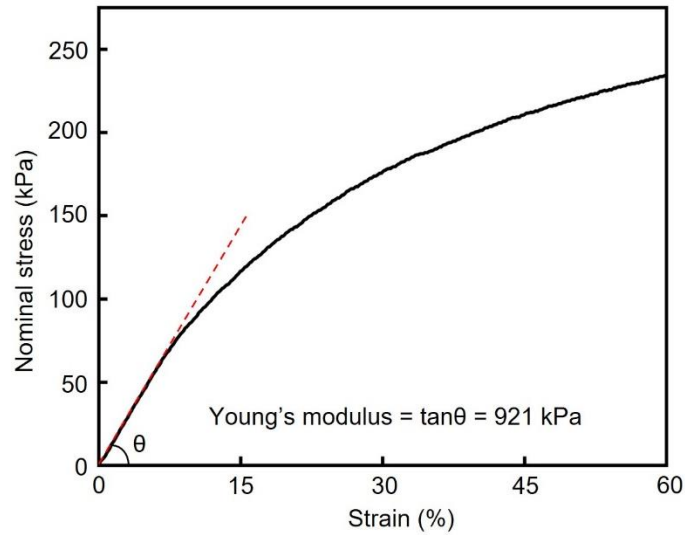
1823 **Supplementary Fig. 6 | Optical images of the multilayered liquid metal composite electrodes.**  
 1824 **a**, Ground electrode. **b**, The first layer. **c**, The second layer. **d**, The third layer. **e**, The fourth layer.  
 1825 **f**, The shielding layer. All images share the same scale bar.



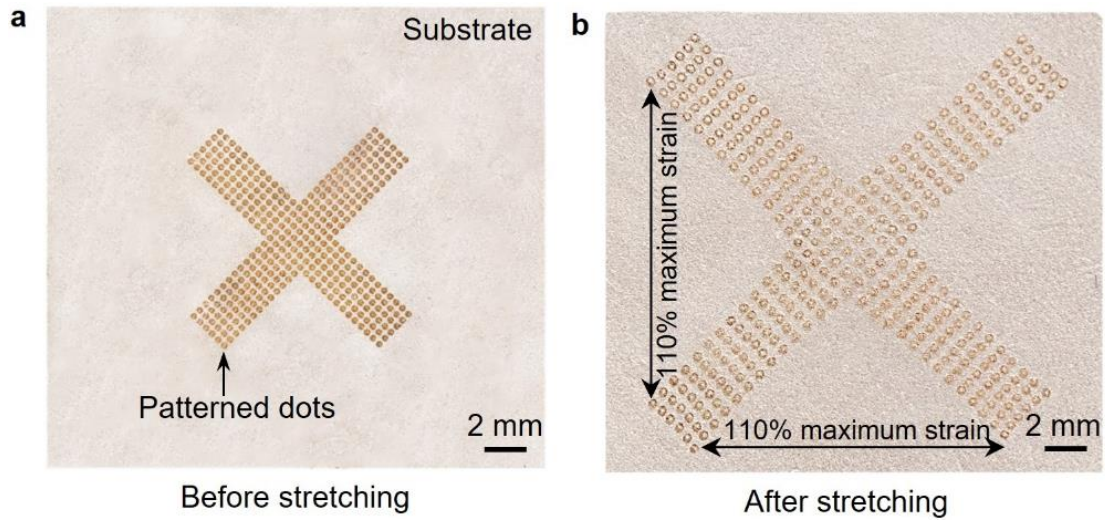
1826 **Supplementary Fig. 7 | The thickness of the SEBS substrate and the printed liquid metal**  
 1827 **composite.** The thicknesses of **a**, the SEBS film and **b**, the liquid metal composite layer were  
 1828 measured by a Dektak profilometer. The thin thicknesses of the substrate and the electrode  
 1829 contribute to the overall low form-factor of the wearable imager.



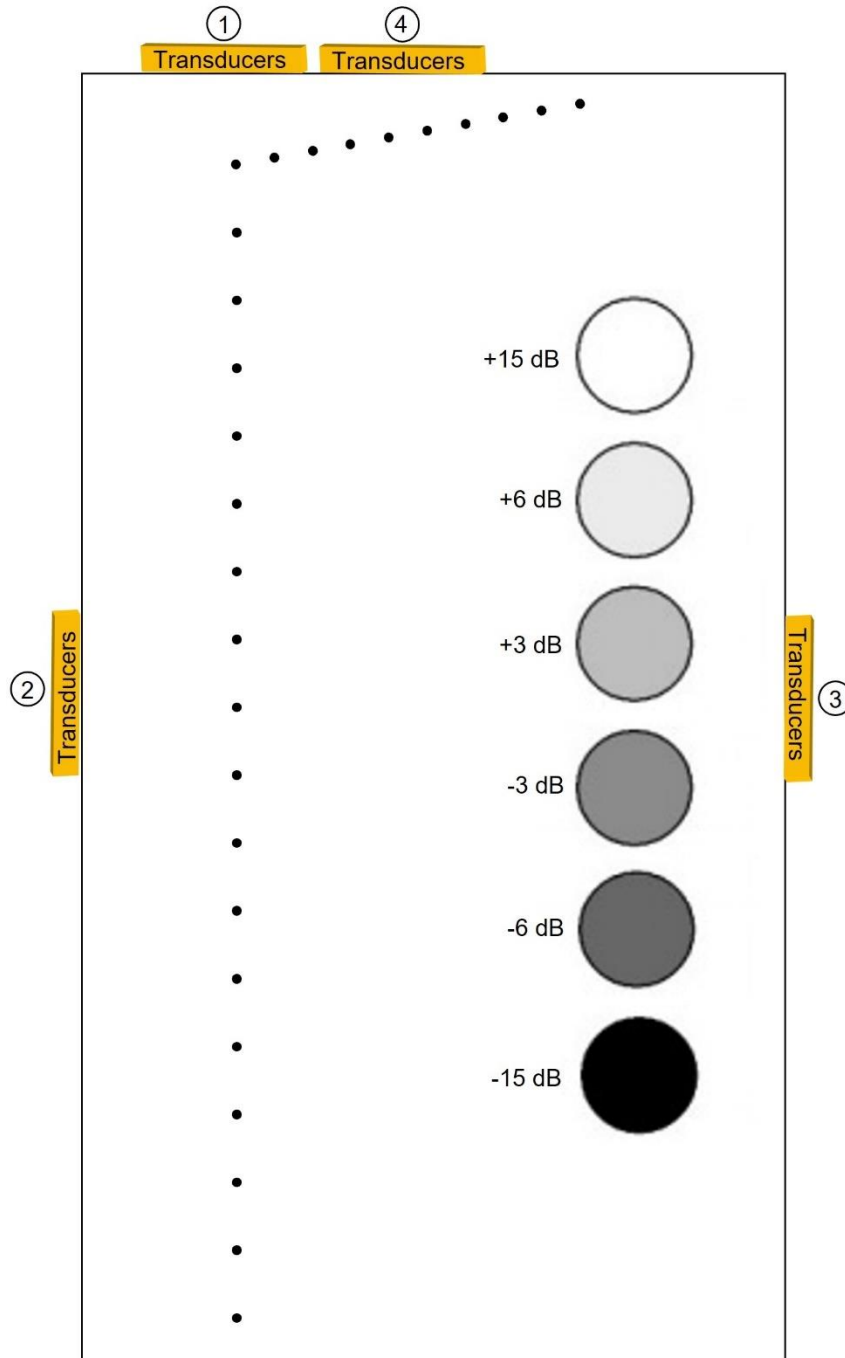
1830 **Supplementary Fig. 8 | Characterization of noise levels after applying different strategies**  
 1831 **sequentially.** **a**, B-mode images and **b**, noise amplitude after Step 1: Shielding electrode. Step 2:  
 1832 Electrical matching between the transducer and the pulser. Step 3: Ground wire modification by  
 1833 adding an inductor and capacitor in series to the ground wire. The modification rendered the  
 1834 ground wire to be more resistive at around the transducer center frequency and drain noise at  
 1835 around the transducer center frequency to the ground better. Other noise can be effectively  
 1836 removed by filters. Step 4: Signal accumulation, which is a built-in function provided by  
 1837 Verasonics. The signal accumulation overlaps recent frames to counteract the running noise. We  
 1838 normalized the noise level by dividing all noise levels by the highest noise level for better  
 1839 comparison. **c**, Signals from the cardiac myocardium mixed with noises without shielding. **d**,  
 1840 Signals with much reduced noises after shielding.



1841 **Supplementary Fig. 9 | Stress-strain curve of the entire device.** The cardiac imager was  
 1842 stretched uniaxially, from which the Young's modulus of the entire device was calculated to be  
 1843 921 kPa. It showed the device had a similar modulus to the human skin (420 to 850 kPa)<sup>24</sup>. The  
 1844 test was performed under nominal stress, which equals to force divided by initial cross-sectional  
 1845 area of the entire device.

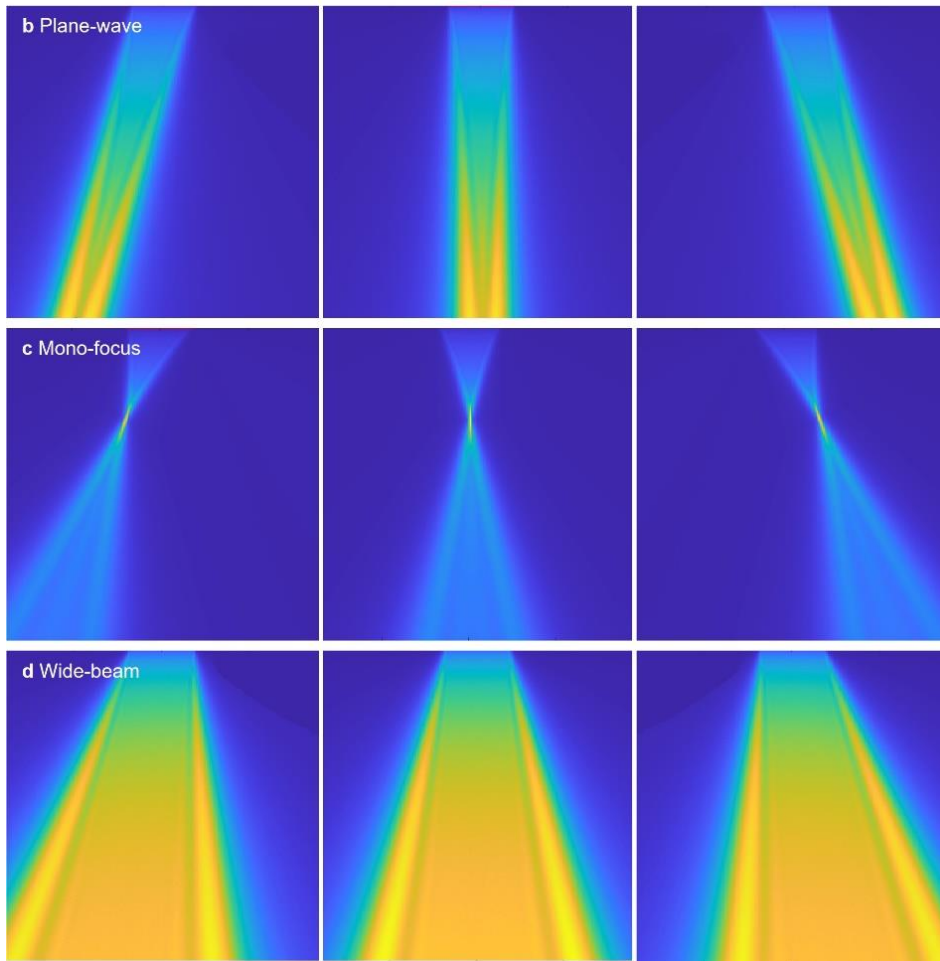
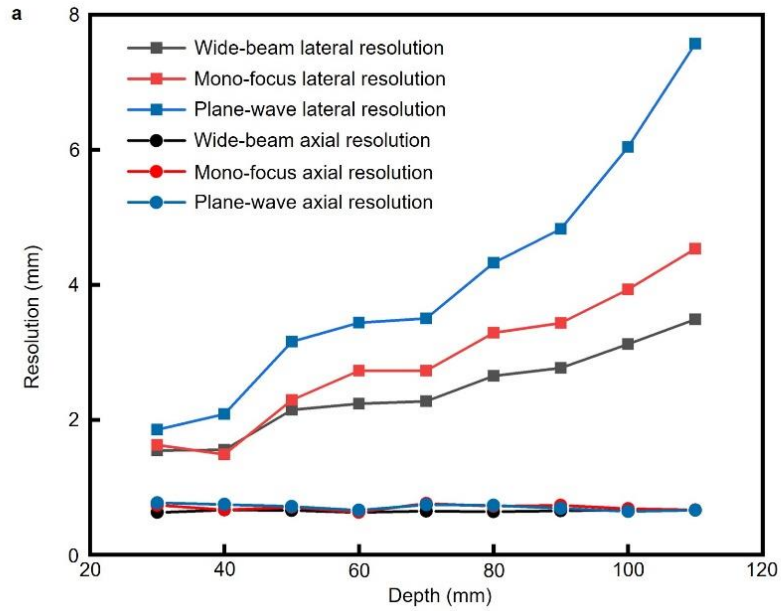


1846 **Supplementary Fig. 10 | Biaxial mechanical testing of the entire device.** Because the shielding  
1847 and ground layers are opaque, we patterned dots on the SEBS substrate to represent the location  
1848 of each transducer element. Optical images show the device **a**, before and **b**, after stretching. The  
1849 spatial distribution of arrayed elements is comparable to that obtained through simulation in Figure  
1850 1e, verifying the accuracy of the simulation.



1851 **Supplementary Fig. 11 | The structure of the phantom for device characterizations.** We used  
 1852 a commercial phantom (CIRS 539) to characterize multiple properties of the wearable imager. The  
 1853 signal-to-noise ratio, axial, lateral and elevational resolutions at different depths, and axial  
 1854 accuracy were tested when the device was put at the position 1. The lateral accuracy, as well as  
 1855 axial and lateral resolutions at different lateral distances, were tested when the device was put at  
 1856 the position 2. The dynamic range, contrast-to-noise ratio, and contrast resolution were tested when  
 1857 the device was put at the position 3. The dead zone was tested when the device was put at the  
 1858 position 4.

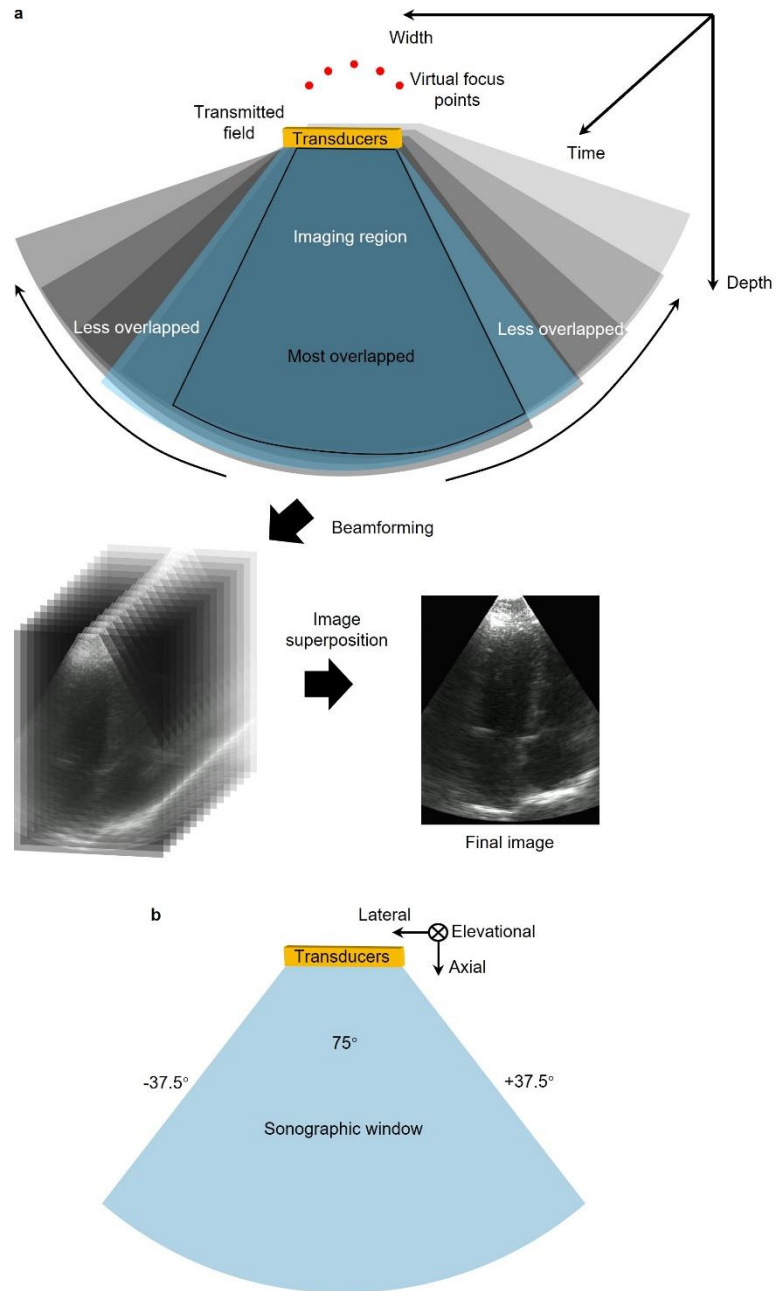




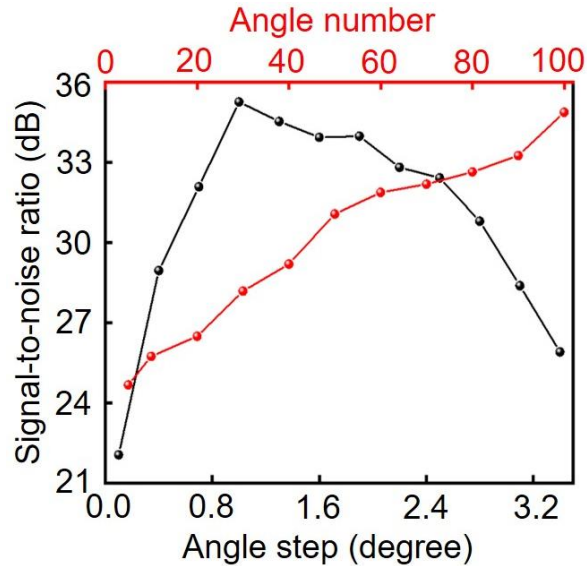
1859 **Supplementary Fig. 12 | Characterization of resolutions and acoustic fields with different**  
 1860 **transmission methods and angles. a,** The lateral and axial resolutions of wide-beam  
 1861 **compounding, mono-focus, and plane-wave transmission**<sup>156,228</sup>. The wide-beam compounding



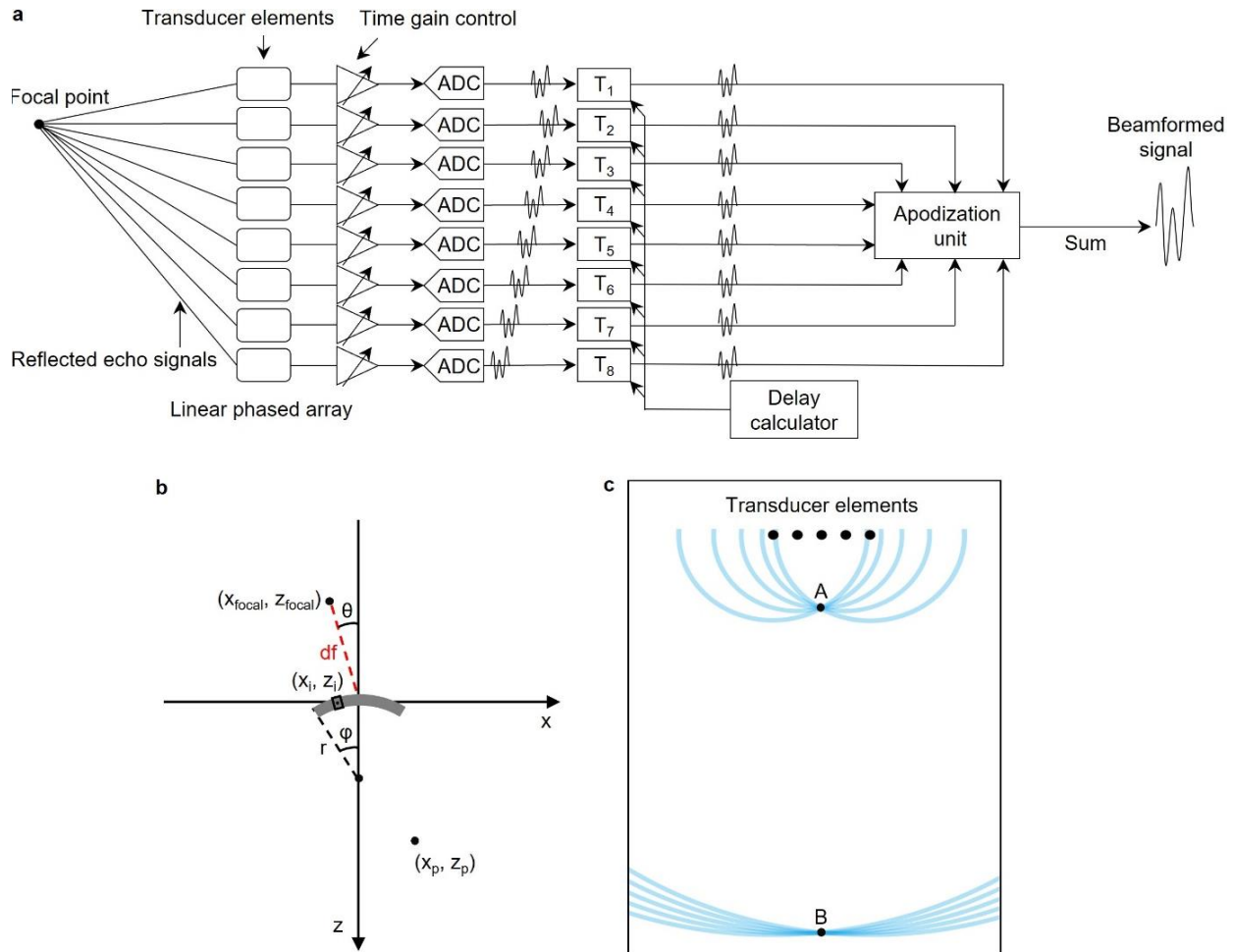
1862 transmission has the best resolutions among all three. Acoustic fields of **b**, plane-wave, **c**, mono-  
1863 focus, and **d**, wide-beam compounding transmission methods, with transmission angles of  $-21^\circ$ ,  
1864  $0^\circ$ , and  $21^\circ$ . The plane-wave strategy produces the worst resolutions. This is because this mode  
1865 only transmits a single plane-wave, resulting in a low echoic signal-to-noise ratio, and poor spatial  
1866 resolutions. The mono-focus strategy yields a greater signal-to-noise ratio, and better spatial  
1867 resolutions. However, the resolution will deteriorate outside the focal zone. The wide-beam  
1868 compounding transmission has a stronger and more uniform acoustic wave intensity over a larger  
1869 area than the other two.



1870 **Supplementary Fig. 13 | The mechanism of wide-beam compounding B-mode imaging.** a,  
 1871 Multiple frames are first acquired with multiple transmissions at different angles. The multiple-  
 1872 angle scan compensates the low echoic energies from regions away from the center, expanding the  
 1873 insonation area from being rectangular to sector-shaped. The enhanced echoic energy improves  
 1874 the resolution at high steering angles. The frames are collected at the same rate as the high pulse  
 1875 repetition frequency. The final image is obtained by the superposition of acquired frames, which  
 1876 achieve synthetic focusing with improved resolution over the entire ultrasonographic window.  
 1877 Additionally, the superposition helps eliminate the random noise in the images. b, Schematics of  
 1878 the acoustic field simulation setup. All key parameters are labeled and set the same as the practical  
 1879 imaging procedure.



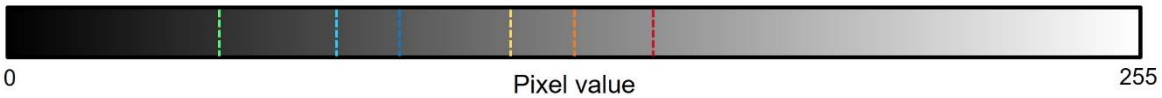
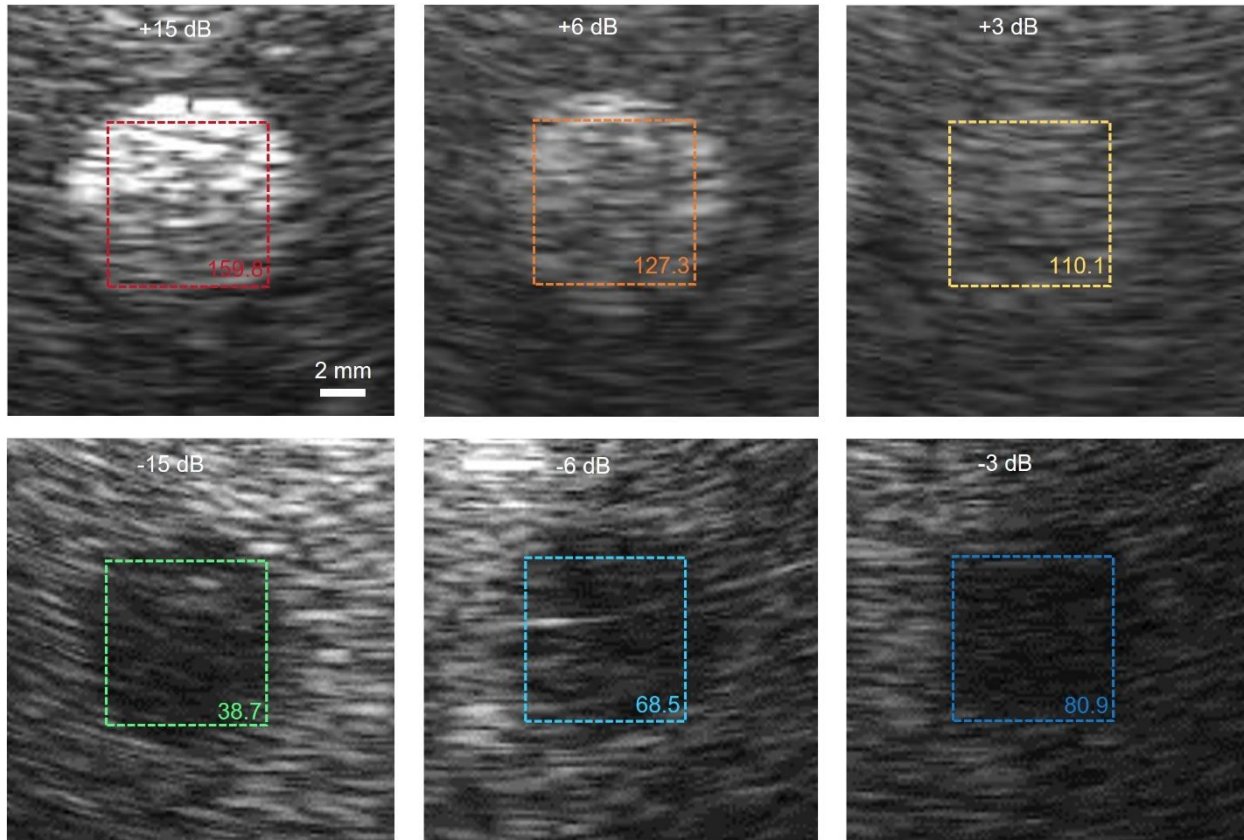
1880 **Supplementary Fig. 14 | Signal-to-noise ratio as a function of step size and number of steering**  
 1881 **angles of the wide-beam compounding imaging.** The image's signal-to-noise ratio firstly rises  
 1882 and then falls with the angle step size but increases monotonically with the angle number. When  
 1883 the angle step size initially increases, the most constructive interference of multiple acoustic fields  
 1884 is in the region of interest, ensuring the highest signal-to-noise ratio for the image reconstruction.  
 1885 As the angle step size keeps increasing, the overlap between individual acoustic fields decreases,  
 1886 resulting in a reduced signal-to-noise ratio. The signal-to-noise ratio increases as the number of  
 1887 angles grows, because all individual acoustic fields are more or less coherently integrated to  
 1888 reconstruct images. However, an excessive number of angles sacrifices the imaging temporal  
 1889 resolution. We used 96 steering angles with a 1° step, which gives adequate penetration depth and  
 1890 spatial resolutions while maintaining an acceptable frame rate of 20-30 Hz.



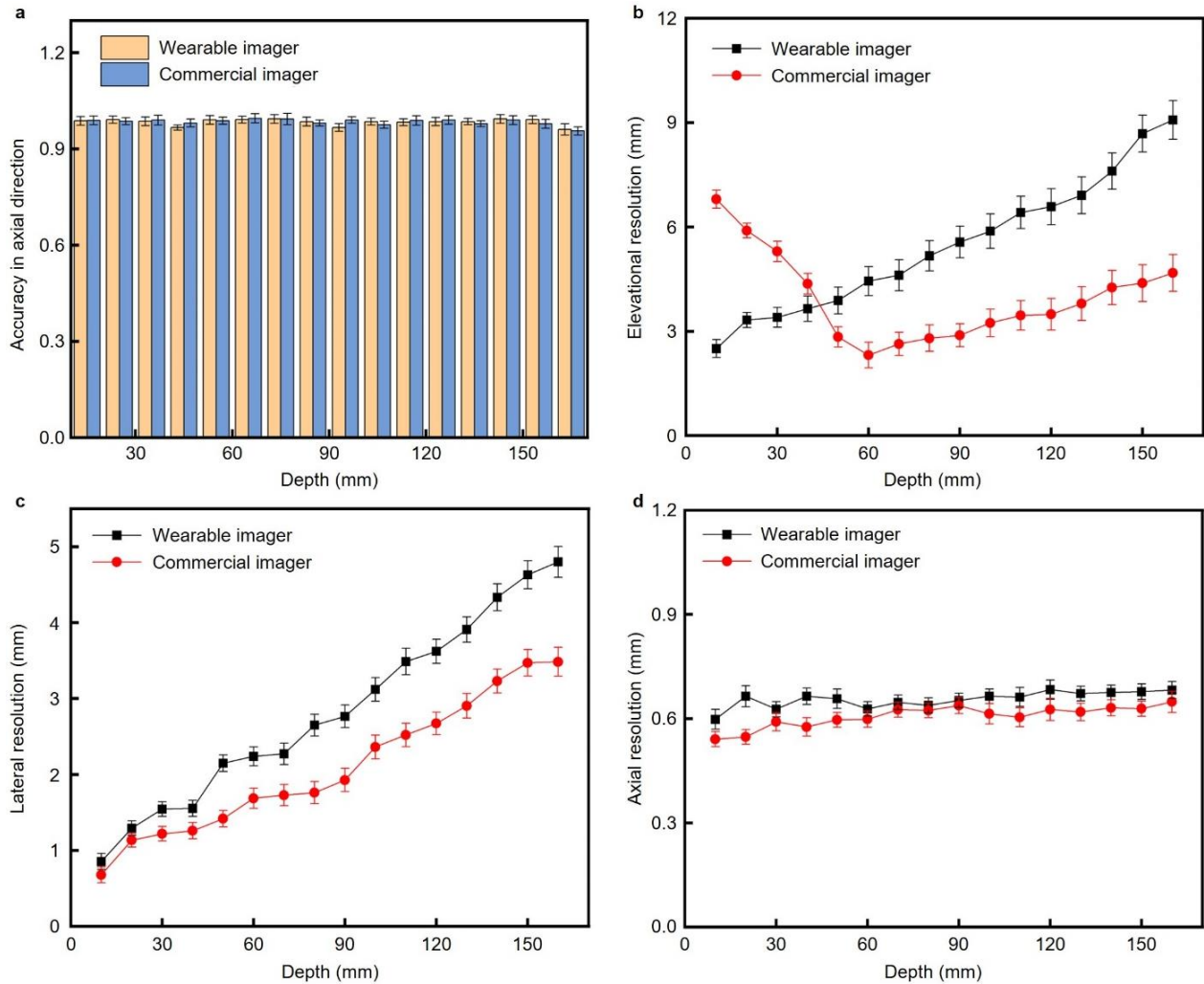
1891

1892 **Supplementary Fig. 15 | The flow chart of receive beamforming.** **a**, The reflected echoes are  
 1893 received by the transducer elements, whose signals are amplified by the time gain control to  
 1894 enhance the weak signals from deep objects. The amplified signals are then converted to digital  
 1895 signals by an analog to digital converter (ADC), and then sent into a delay calculator for phase  
 1896 difference correction and signal alignment. Direct summing of the synchronized signals may result  
 1897 in significant side-lobe artifacts. Therefore, adaptive apodization assigns varying weights to the  
 1898 various signals, which are eventually summed together as beamformed signals with an enhanced  
 1899 signal-to-noise ratio. **b**, Schematic calculation for phase correction. ( $x_{focal}, z_{focal}$ ) is the focal point.  
 1900 ( $x_i, z_i$ ) is the  $i^{th}$  transducer. ( $x_p, z_p$ ) is the pixel of interest.  $\theta$  is the steering angle.  $df$  is the focal  
 1901 depth.  $r$  is the curvature radius.  $\varphi$  is the angle departure of the  $i^{th}$  transducer from  $z$ -axis on the  
 1902 curvature. **c**, Schematic receive beamforming of ultrasound signals. There are two beamformed  
 1903 signals A and B. The lateral diffusion in A is less than that in B, which indicates a better lateral  
 1904 resolution of A. In other words, the closer the imaging area to the transducer elements, the better  
 1905 the lateral resolution.

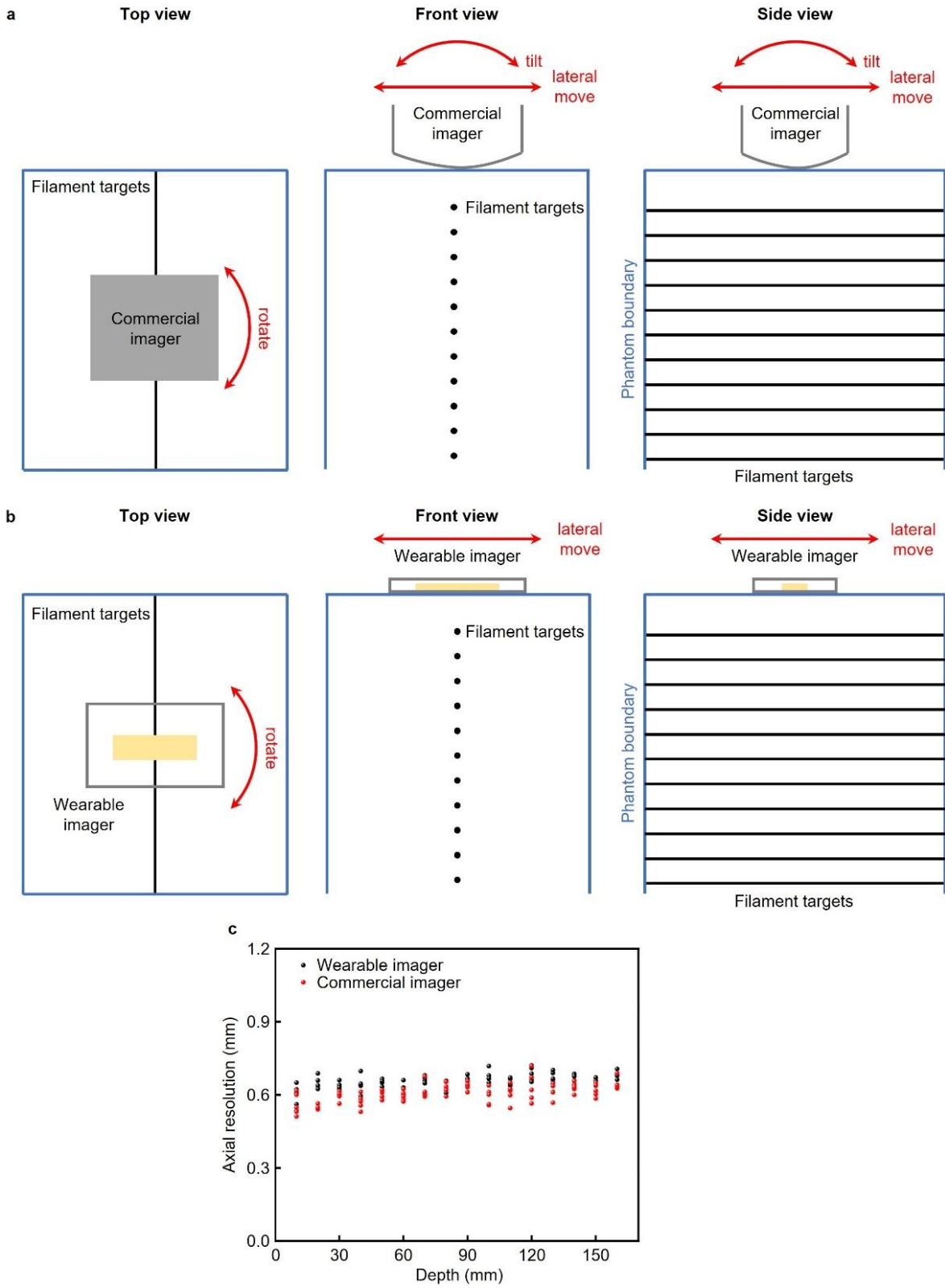
1906



1907  
 1908 **Supplementary Fig. 16 | Gray scale B-mode images of phantoms and selected windows for**  
 1909 **calculating the dynamic range.** Red: The +15 dB contrast gives an average pixel value of 159.8.  
 1910 Orange: The +6 dB contrast gives an average pixel value of 127.3. Yellow: The +3 dB contrast  
 1911 gives an average pixel value of 110.1. Green: The -15 dB contrast gives an average pixel value of  
 1912 38.7. Cyan: The -6 dB contrast gives an average pixel value of 68.5. Blue: The -3 dB contrast gives  
 1913 an average pixel value of 80.9. These pixel values are labelled on the pixel scale bar at the bottom.  
 1914 The dynamic range is thus calculated to be 63.2 dB, which is well above the 60 dB threshold  
 1915 usually used in medical diagnosis to give adequate details of the echo patterns in the images.



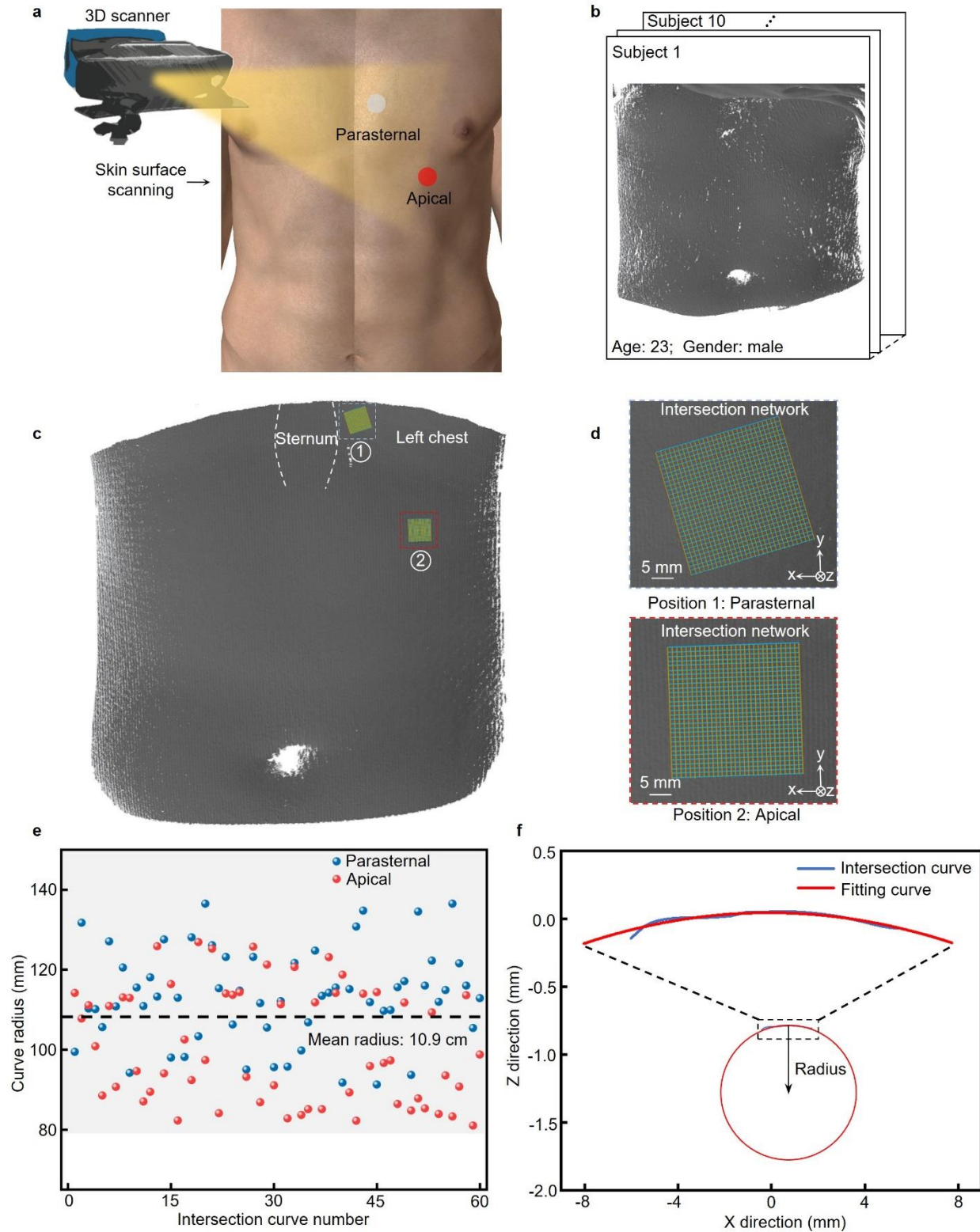
1916 **Supplementary Fig. 17 | Detailed comparison of the imaging metrics between the wearable**  
 1917 **and the commercial imagers. a**, Accuracy of the detected scatter positions as a function of the  
 1918 scatter depth. **b**, Elevational resolution as a function of depth. **c**, Lateral resolution as a function of  
 1919 depth. **d**, Axial resolution as a function of depth. Each test was repeated for five times. Each  
 1920 column or point is defined by the mean and the standard deviation (the error bar) of the results  
 1921 from five tests.



1922 **Supplementary Fig. 18 | Schematic experimental setups of resolution tests.** The setups are for  
 1923 **a**, the commercial imager and **b**, the wearable imager. The degrees of freedom of each imager are

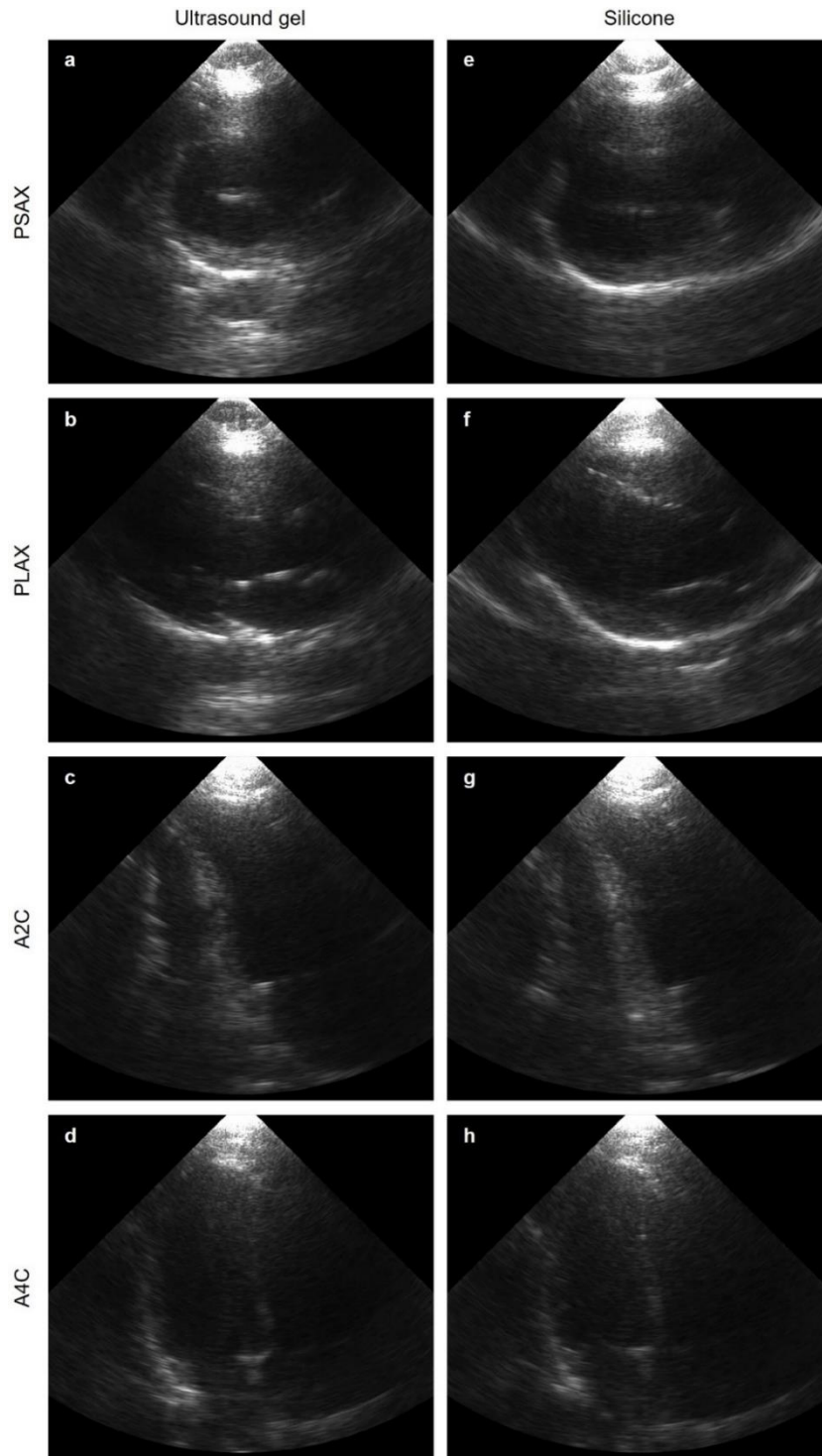
1924 labeled in red arrows. c, The axial resolutions of the wearable imager and the commercial imager  
1925 at each depth were measured five times. The five degrees of freedom of the commercial imager  
1926 and the three degrees of freedom of the wearable imager introduced measurement variations. The  
1927 higher the degrees of freedom, the higher the possibility of worsening the measured axial  
1928 resolutions. Even though the commercial imager bandwidth is larger than that of the wearable  
1929 imager, some data points of the commercial imager are worse than those of the wearable imager  
1930 because of the measurement variations.



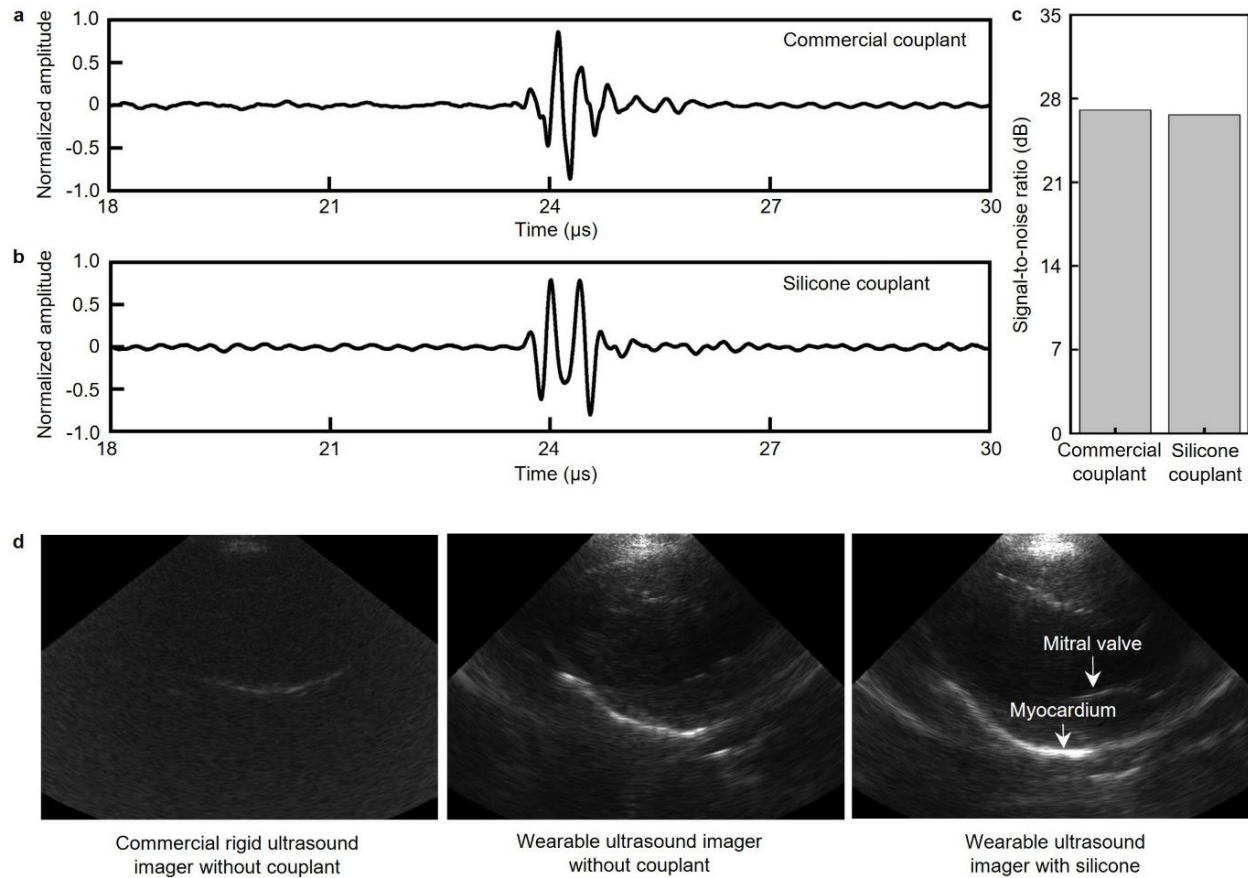


1931 **Supplementary Fig. 19 | Processes of evaluating the surface curvature for phase correction.**  
 1932 **a**, Scan the imaging sites on the subject using a 3D scanner. **b**, Obtain 3D surface reconstruction  
 1933 from the scanning. **c**, Select the two sites of interest in this study and build intersection networks

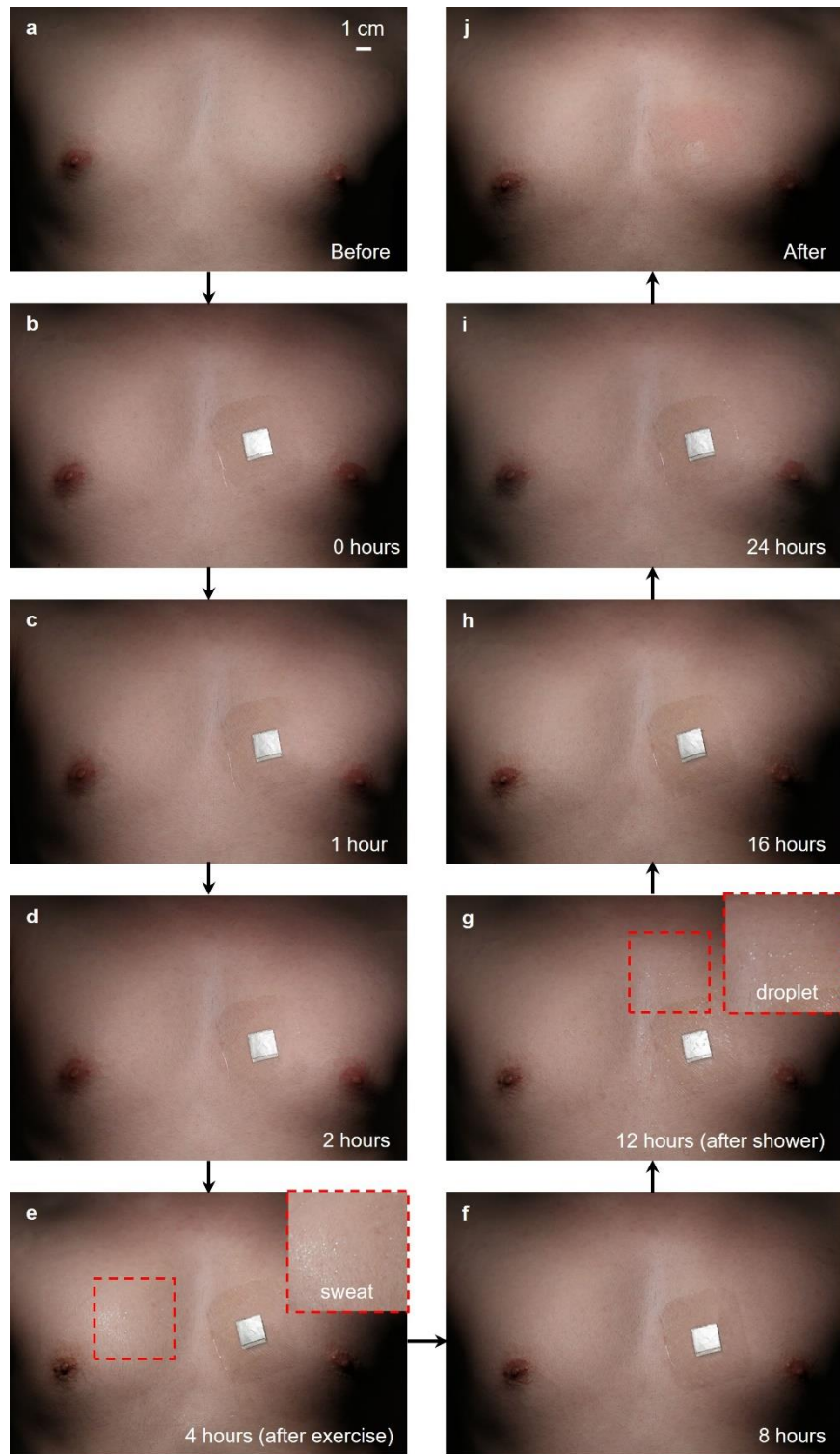
1934 in the Catia software. **d**, Zoomed-in schematics of the two intersection networks from a  
1935 reconstructed 3D surface. **e**, Collect the average curve radii from curves in the intersection  
1936 networks. **f**, Fit every intersection curve with a smooth curve. Select the intersection curve whose  
1937 fitting radius is the closest to the mean radius of all curves from the site. The fitting curve is then  
1938 used to correct the phased distortion induced by the surface curvature of human body.



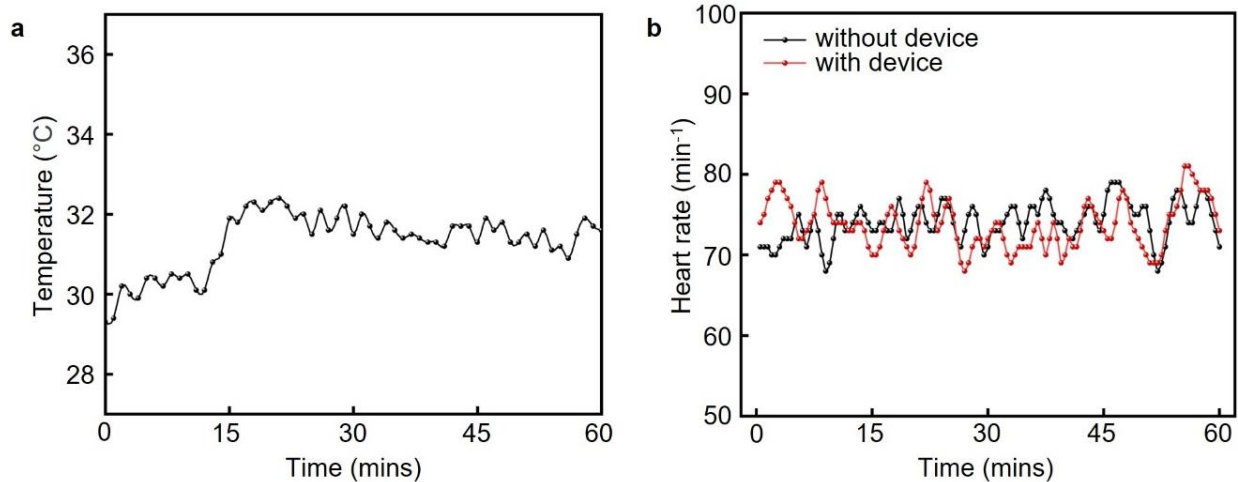
1939 **Supplementary Fig. 20 | B-mode images collected with different couplants. a-d,** The PSAX,  
 1940 PLAX, A2C and A4C views collected with evaporative ultrasound gel. **e-h,** The PSAX, PLAX,  
 1941 A2C and A4C views collected with non-evaporative silicone. No obvious structural differences  
 1942 are found in the comparison. PSAX: parasternal short axis view; PLAX: parasternal long axis view;  
 1943 A2C: apical two-chamber view; A4C: apical four-chamber view.



1944 **Supplementary Fig. 21 | Quantitatively evaluation of different coupling conditions.**  
 1945 Comparison of the coupling performance between commercial ultrasonic gel and liquidous  
 1946 silicone couplants. Received signals of the single transducer with **a**, commercial ultrasonic gel,  
 1947 and **b**, liquidous silicone couplant. **c**, The two couplants result in comparable signal-to-noise ratios  
 1948 of the received signals. **d**, Cardiac images taken under different coupling conditions. The left panel  
 1949 shows the image from a commercial rigid ultrasound imager without couplant. The middle panel  
 1950 shows the image from a wearable ultrasound imager without couplant. The right panel shows the  
 1951 image from a wearable ultrasound imager with silicone couplant.

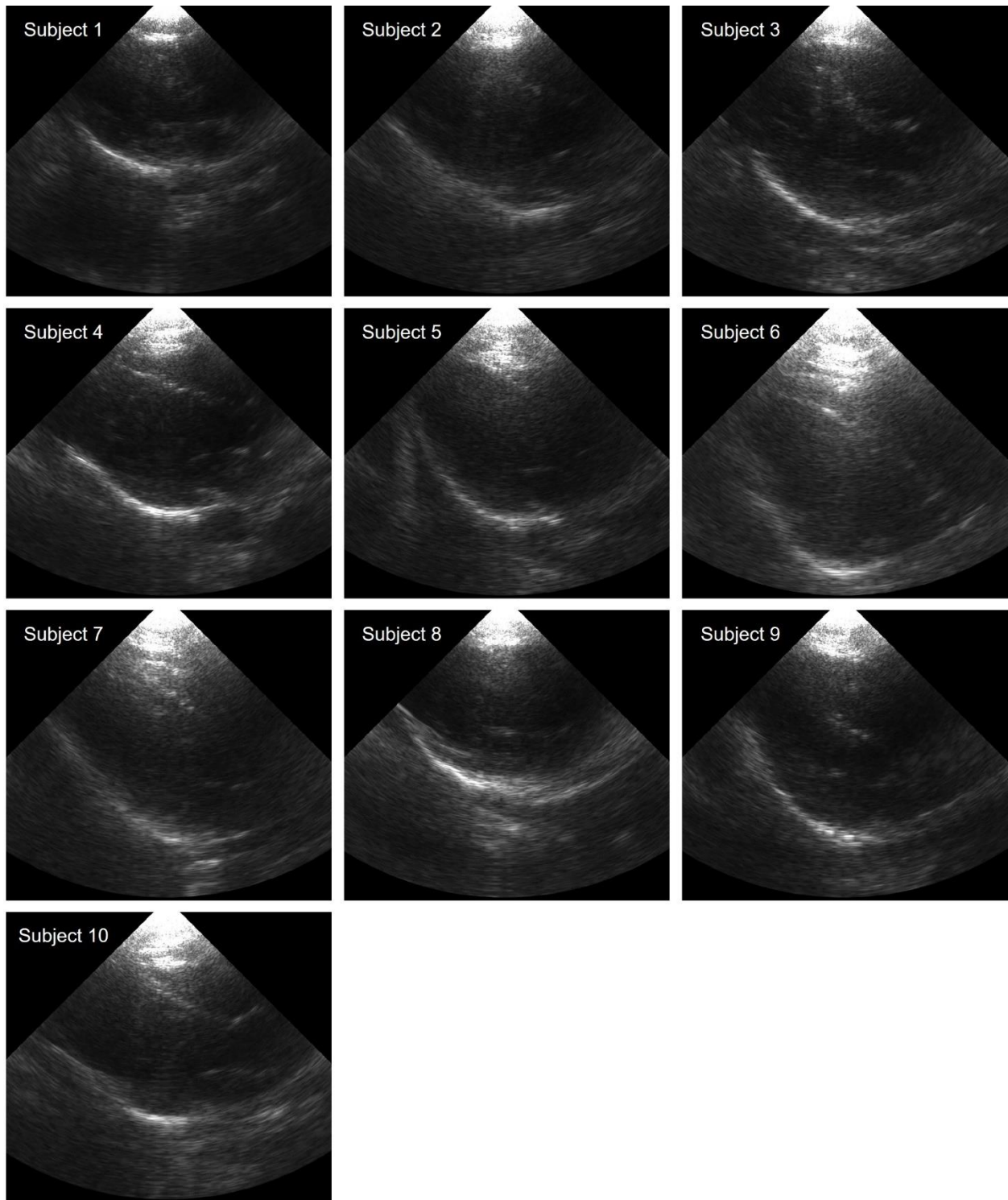


1952 **Supplementary Fig. 22 | Optical images of attaching the wearable imager to the chest for**  
 1953 **long-term.** Optical images of the chest **a**, before attaching the probe, **b-i**, 0, 1, 2, 4, 8, 12, 16, and  
 1954 24 hours after the attachment, and **j**, after detaching the imager from the human body. Sweat  
 1955 droplets can be seen in the zoomed-in inset in **e**, after the subject finished working out. Water  
 1956 droplets can be seen in the zoomed-in inset in **g**, after the subject finished showering.

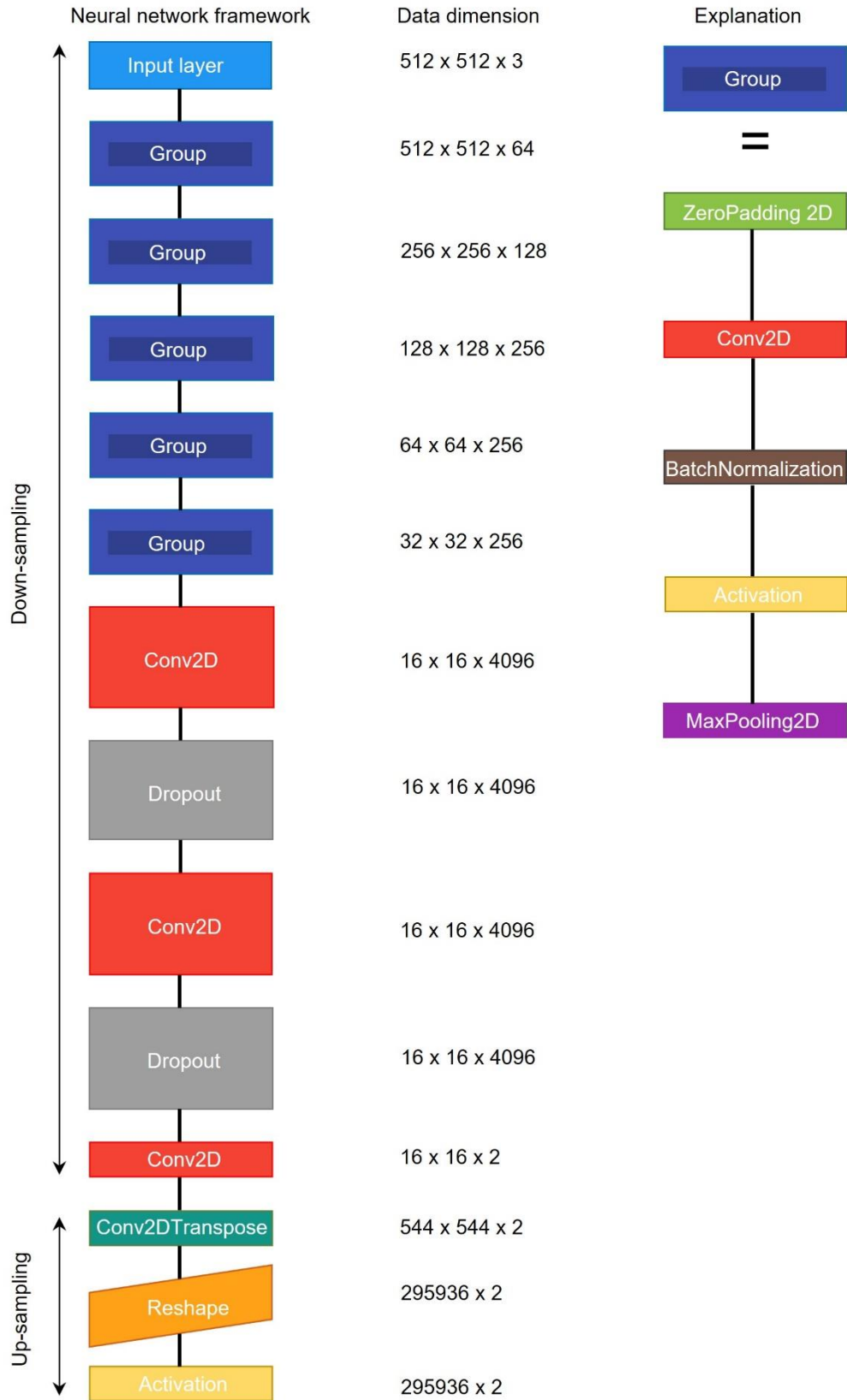


1957 **Supplementary Fig. 23 | Continuous surface temperature and heart rate monitoring for 1**  
 1958 **hour. a.** Recording the surface temperature of the device by a thermal camera every minute for 1  
 1959 hour. The highest temperature is ~33 °C, which is harmless to the human body. **b.** Monitoring the  
 1960 heart rate using a oximeter every half minute with and without the device attachment. No obvious  
 1961 difference is observed, showing the safety of the wearable cardiac imager for long-term monitoring.





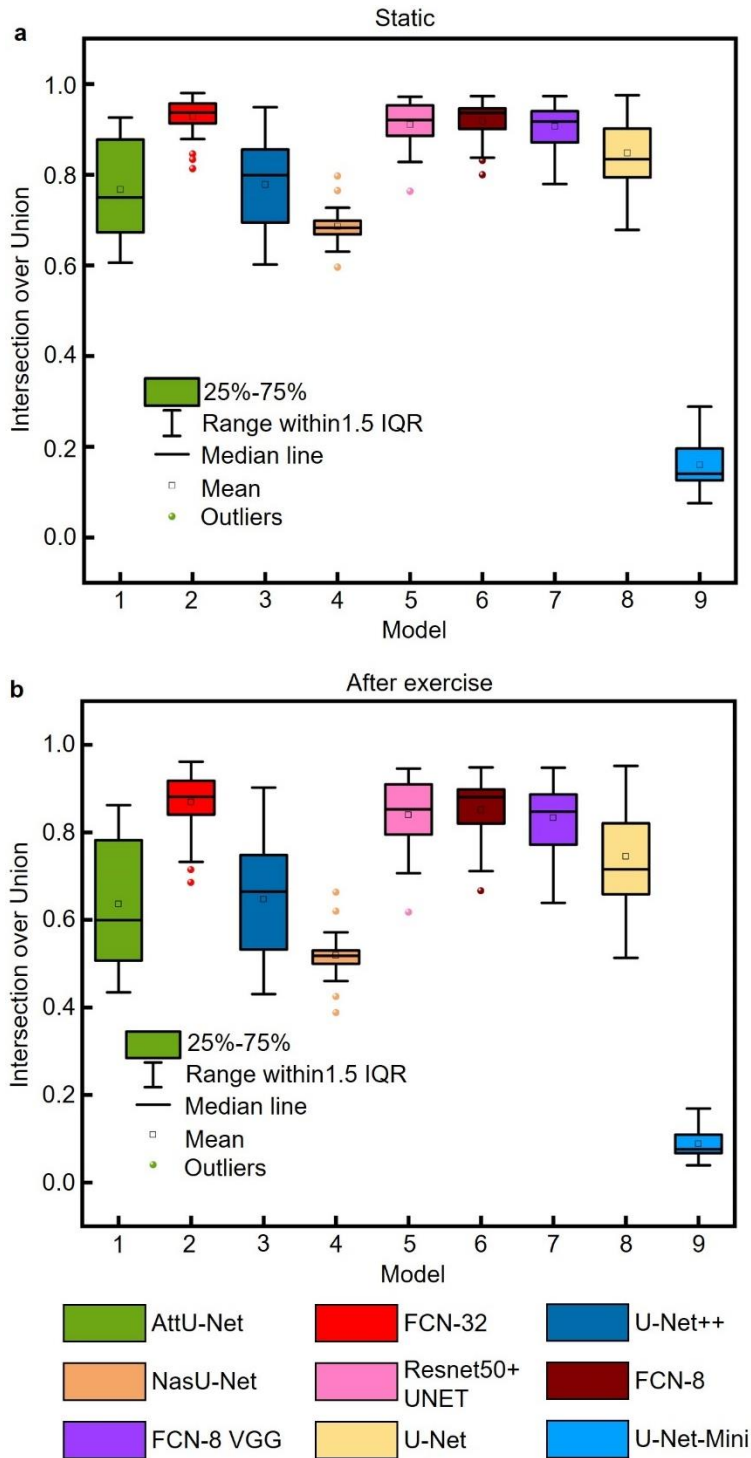
1962 **Supplementary Fig. 24 | Images of the parasternal long axis view from 10 subjects using a**  
1963 **recycled device.** Expanding the testing cohort size validates the reproducibility and reliability of  
1964 the wearable imager.



1965 **Supplementary Fig. 25 | The structure of the FCN-32 neural network.** The FCN-32's structure

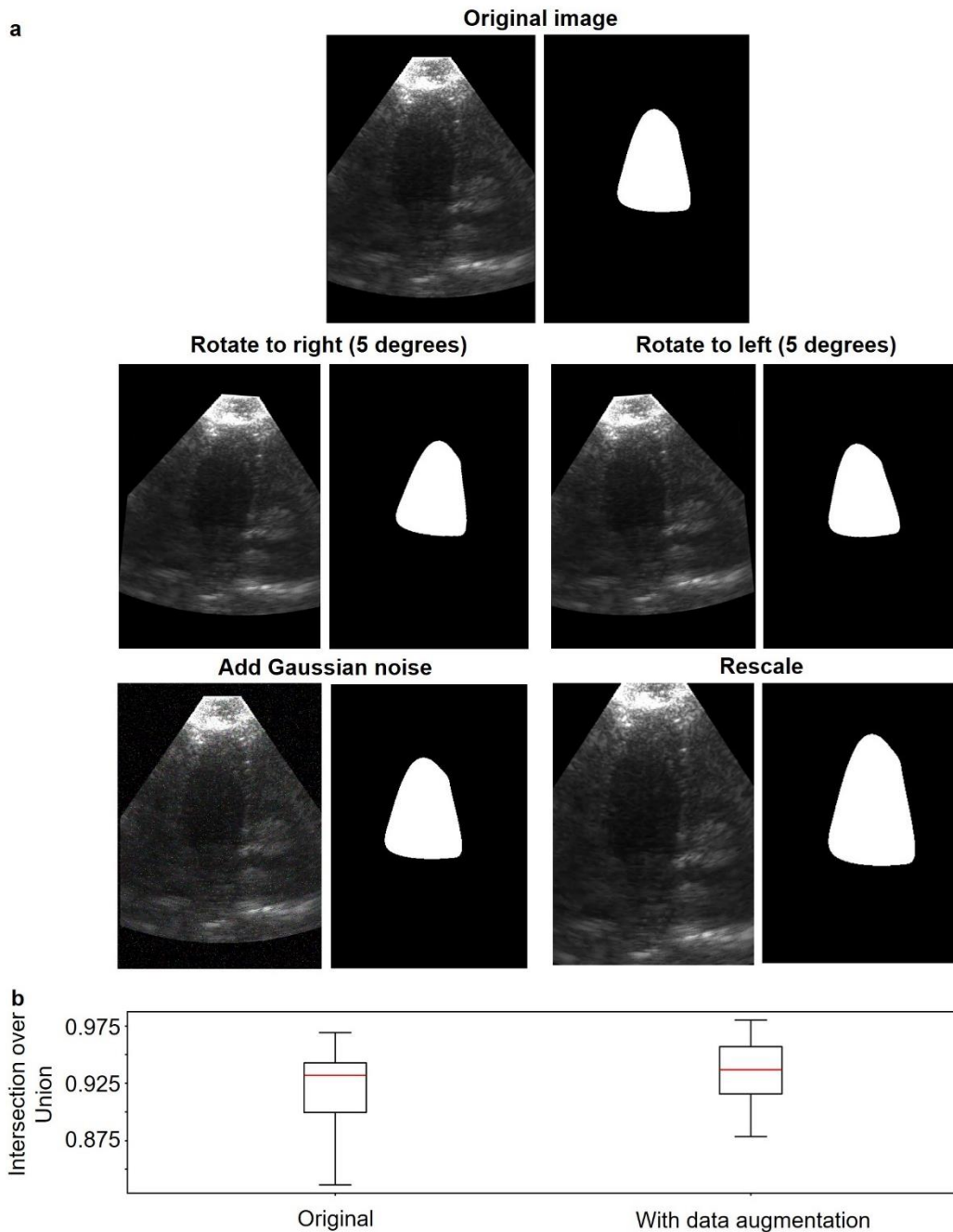


1966 includes a series of fully-connected convolutional neural network (CNN) layers and an upsampling  
1967 layer at the end. We used the AlexNet structure for the downsampling process. The input layer is  
1968 first connected to five groups of connected CNN layers, then connected to two additional CNN-  
1969 dropout bilayers, and finally connected to an upsampling layer to restore to its original size.  
1970 Specifically, the five CNN groups have similar structures but different dimensions. The input of  
1971 each group is first zero-padded and sent into a 2D convolutional layer. Then, we used batch  
1972 normalization to standardize the CNN's output and activate it with a Rectified Linear Unit and  
1973 downsample it with max-pooling.

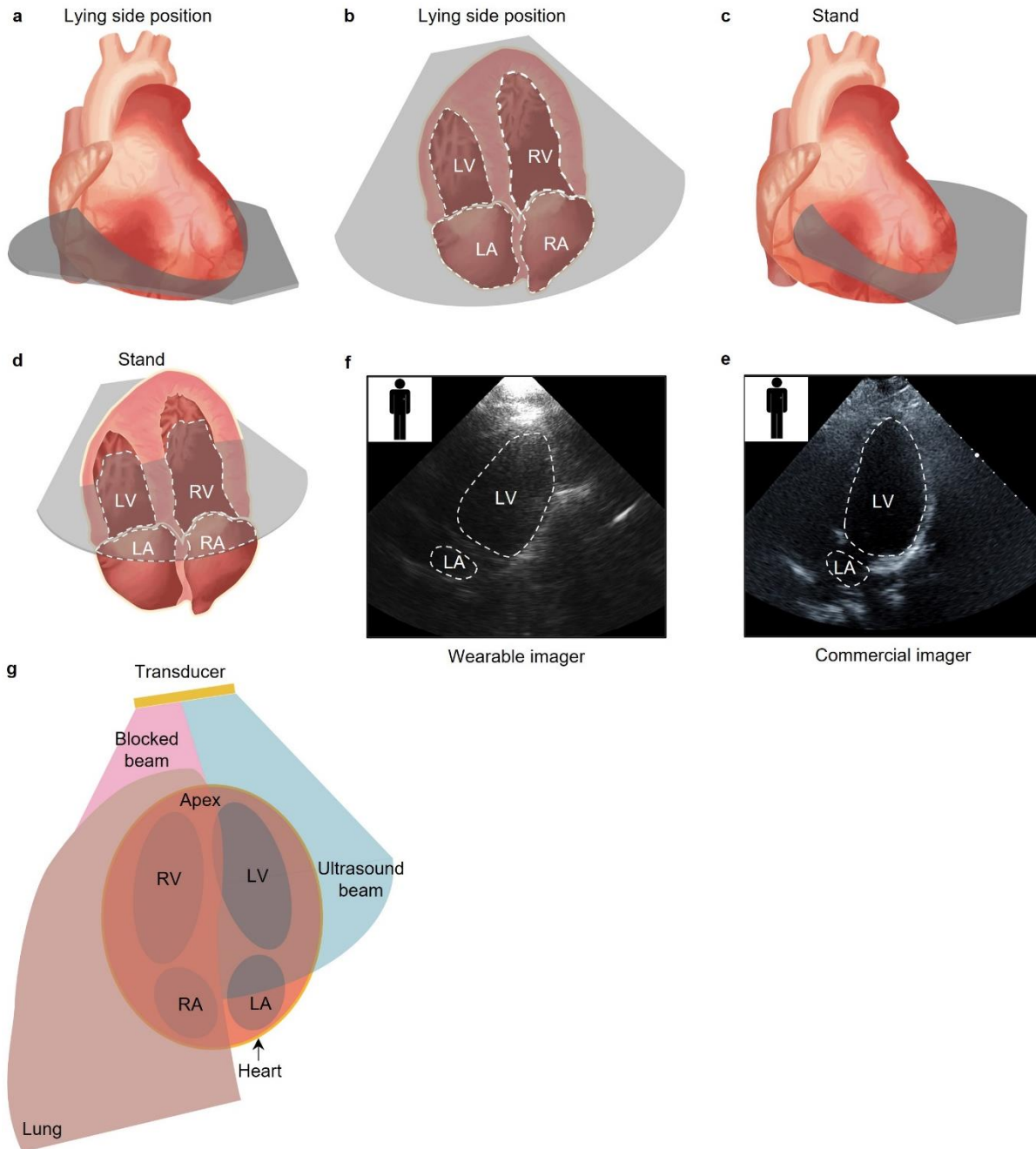


1974 **Supplementary Fig. 26 | The comparison of the intersection over union among different**  
 1975 **models used in this study.** The comparison is made **a**, before and **b**, after exercise. For a pair of  
 1976 predicted images and manually-labelled ground truth image, its intersection over union equals to  
 1977 the number of pixels that are classified as within the left ventricle in both images divided by the  
 1978 total number of unique pixels that are classified as within the left ventricle by either of the two  
 1979 images. The figure shows each model's Intersection over Union on a testing dataset. The FCN-32

- 1980 performs the best with the highest intersection over union and its variation is among the lowest.
- 1981 1.5 interquartile range (IQR) is a common rule in statistics to differentiate the outliers. Data points
- 1982 outside of this range are regarded as outliers.

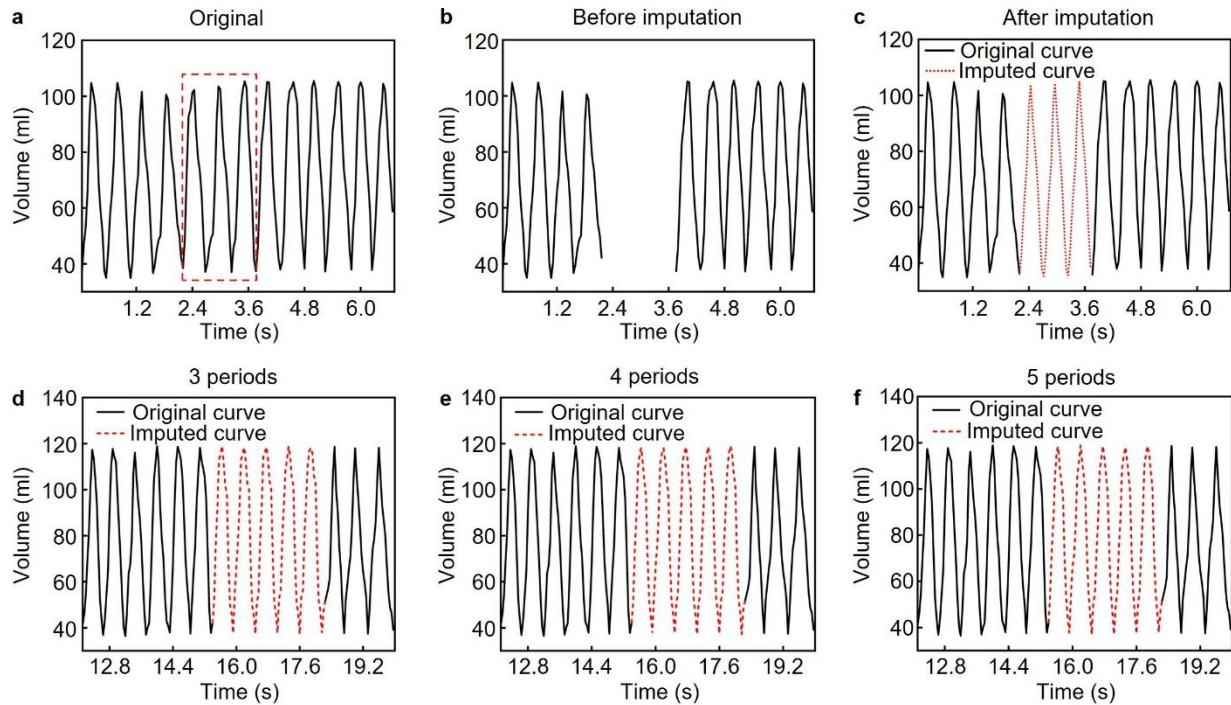


1983 **Supplementary Fig. 27 | The types and results of data augmentation.** **a**, Four types of data  
 1984 augmentation and corresponding segmentation results. We applied rotation, scaling, and gaussian  
 1985 noise to the data to augment the size of the dataset. **b**, The data augmentation increases the average  
 1986 and reduces the variation of mean intersection over union.



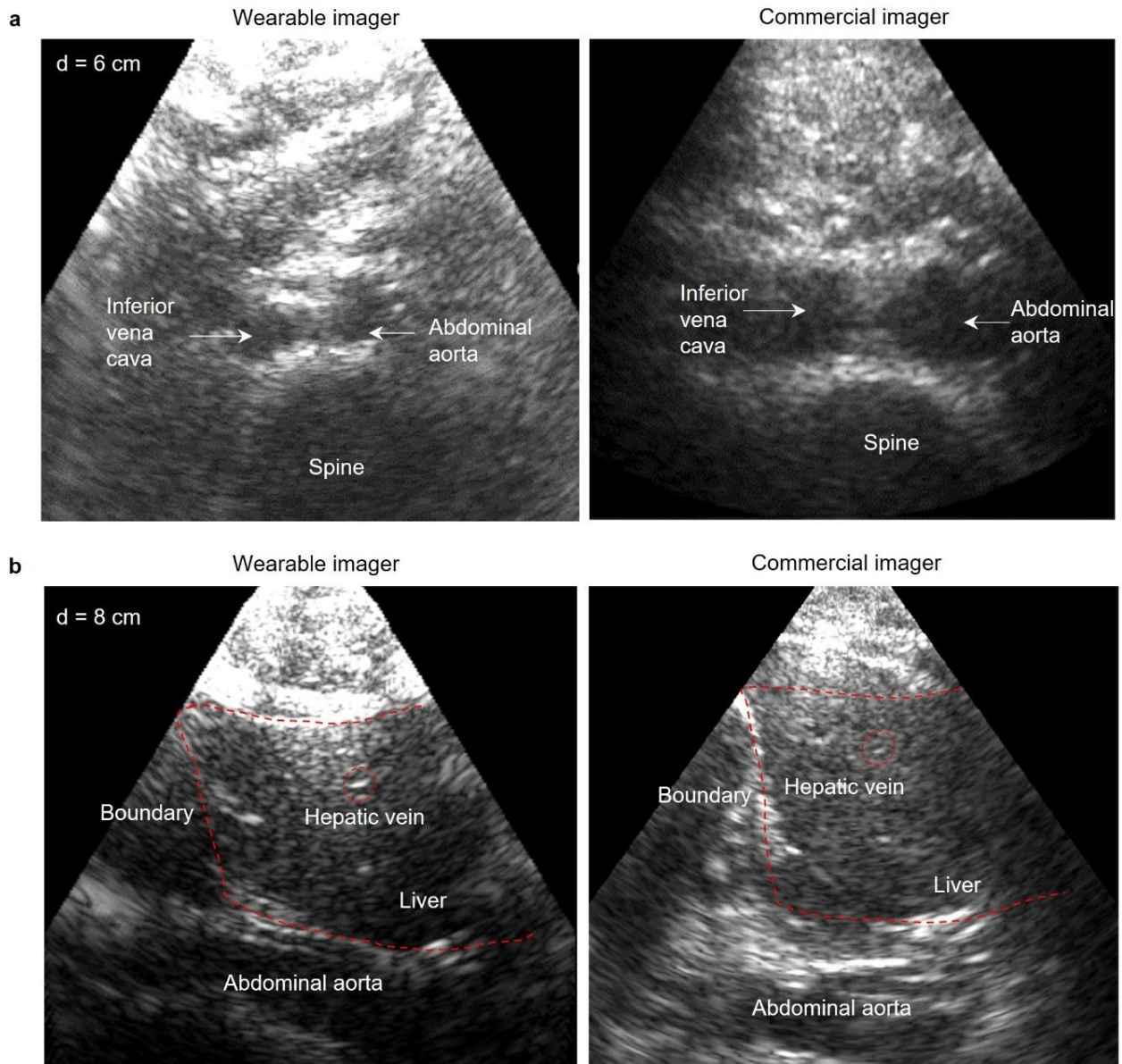
1987 **Supplementary Fig. 28 | Imaging from apical four chamber view with different positions.** a,  
 1988 and b, showing schematics of the apical four chamber view in the lying side position. The  
 1989 ultrasound beam enters the heart directly from the apex, and the morphology of four chambers  
 1990 can be fully scanned (white dash box in b), which will result in accurate calculation of left ventricle  
 1991 volume and cardiac indices. c, and d, showing the apical four chamber view in the standing  
 1992 position. The ultrasound beam enters the heart obliquely from the apex, causing incomplete  
 1993 imaging of four chambers (white dash box in d). e, showing an image from a commercial imager  
 1994 tested by an experienced cardiac sonographer. f, showing an image from a wearable ultrasound  
 1995 imager by a trained amateur. Left ventricle (LV) and left atrium (LA) can be roughly seen in both

1996 images. **g**, Because a part of the transducer array was blocked by the lung, only the unblocked part  
1997 could send ultrasound to the LV and LA, which led to a low signal-to-noise ratio and a lower image  
1998 quality in the standing position than that in the lying side position. Both the right ventricle and  
1999 right atrium were mostly obscured due to lung shadow.



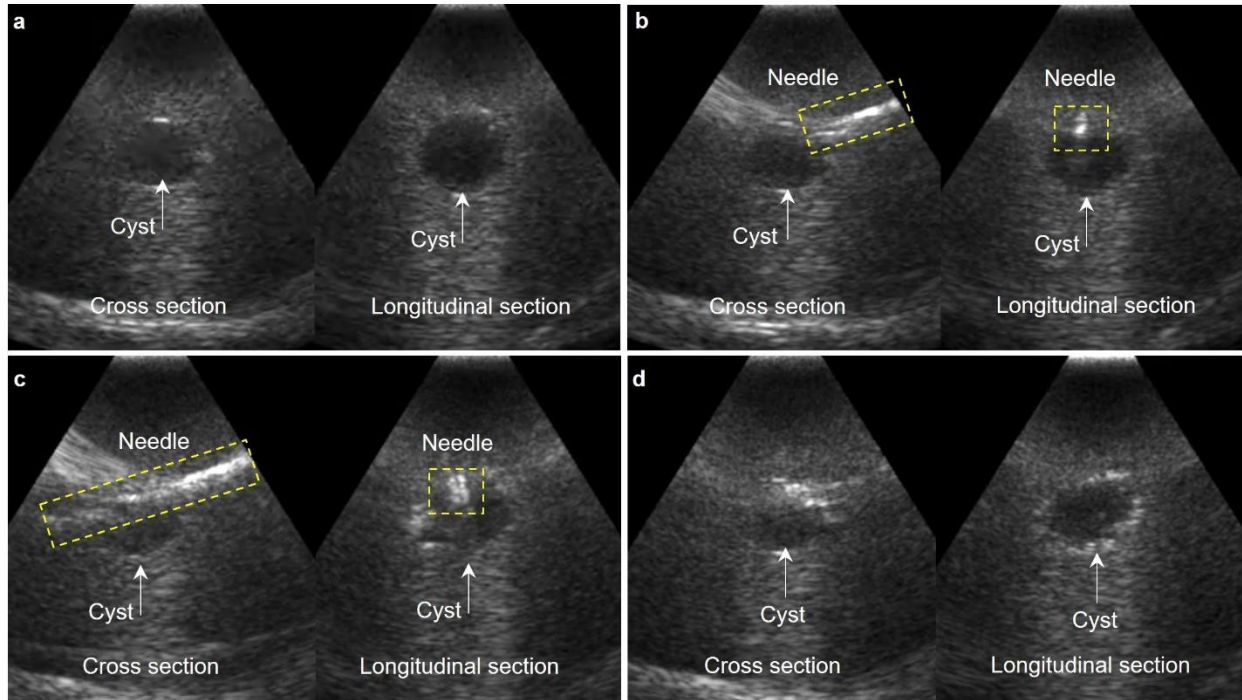
2000 **Supplementary Fig. 29 | Validation of the image imputation algorithm.** To validate the  
 2001 reliability of this image imputation algorithm, we manually erased three periods from **a**, an  
 2002 originally continuous volume wave to get **b**, the erased result before imputation. After imputation,  
 2003 **c**, the completed new wave has a good agreement with the original one with a 0.93 Pearson  
 2004 correlation coefficient. To define the hyperparameter N, we compared different imputation results  
 2005 with **d**, N=3, **e**, N=4, and **f**, N=5. The results show the differences between the generated waves  
 2006 from various N numbers are negligible. We decide to use N=3 in practice for its simplicity and  
 2007 algorithm efficiency.



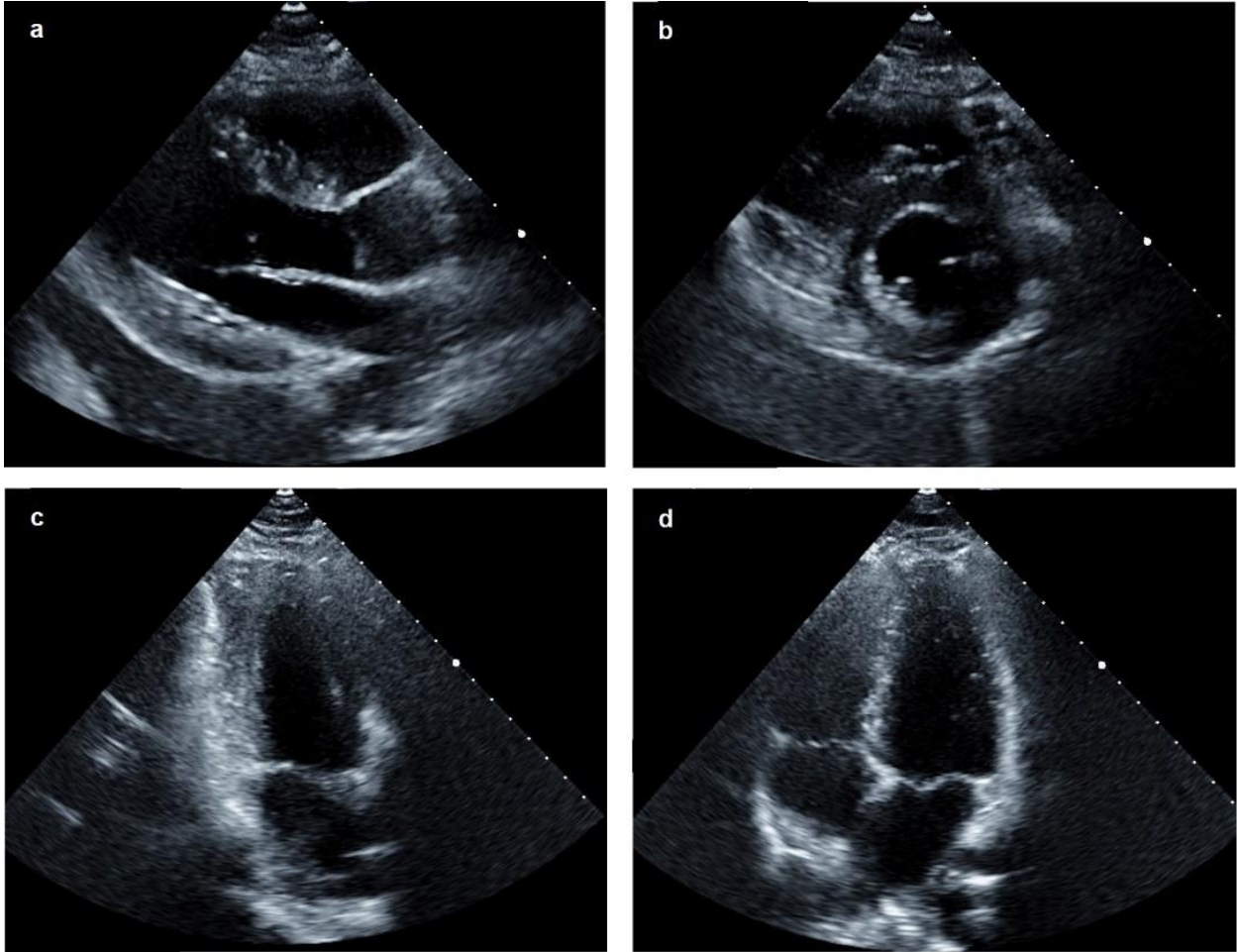


2008 **Supplementary Fig. 30 | B-mode images of the abdominal area and liver from the wearable**  
 2009 **and the commercial imagers. a**, B-mode images of the abdominal area with a depth of ~6 cm.  
 2010 Similar structures including the inferior vena cava and abdominal aorta can be recognized in both  
 2011 images. **b**, B-mode images of the liver with a depth of ~8 cm. The complete boundary and fine  
 2012 structures such as the hepatic vein can be observed in both images.

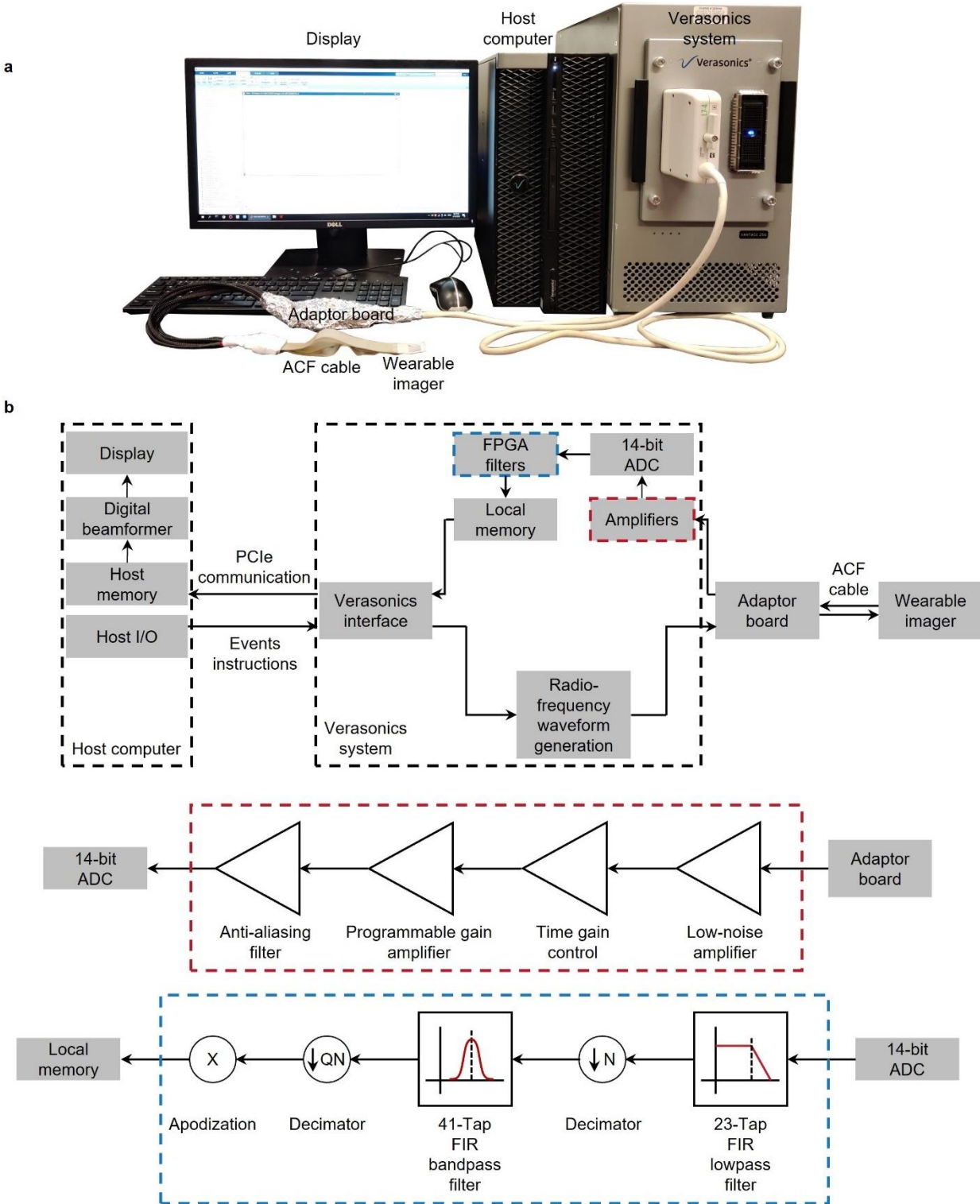




2013 **Supplementary Fig. 31 | B-mode images of biopsy tests on a commercial phantom (CIRS 052).**  
 2014 **a**, The cross section and longitudinal section of the area of interest before inserting the biopsy  
 2015 needle. **b**, The cross section and longitudinal section of the area of interest after inserting the biopsy  
 2016 needle. **c**, The cross section and longitudinal section of the area of interest after releasing the inner  
 2017 inner stylet. **d**, The cross section and longitudinal section of the area of interest after removing the biopsy  
 2018 needle. The positions and the behaviors of the biopsy needle are clearly recorded in two orthogonal  
 2019 orientations simultaneously by the wearable imager. The uniquely enabling capability of the  
 2020 wearable imager is to forgo the need for an operator to constantly hold the device.

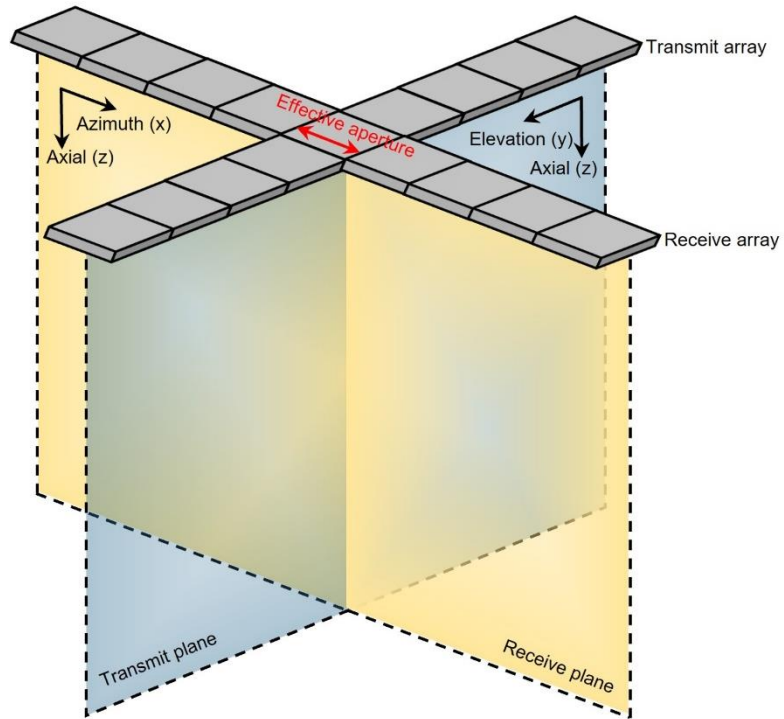


2021 **Supplementary Fig. 32 | B-mode images of cardiac anatomies tested by an experienced**  
2022 **cardiac sonographer.** B-mode images from **a**, parasternal long axis view, **b**, parasternal short axis  
2023 view, **c**, apical two-chamber view, and **d**, apical four-chamber view using a clinical ultrasound  
2024 machine.



2025 **Supplementary Fig. 33 | Photograph and schematics of the imaging system.** **a**, Experimental  
 2026 setup of the imaging system. Key components have been labelled. **b**, Working flow chart of the  
 2027 system. Red dashed box: Analog signal conditioning path. The low-noise amplifier pre-amplifies  
 2028 the raw signal with high fidelity to facilitate the following conditioning. The time gain control is a

2029 programmable amplifier that can selectively amplify electrical signals induced by echoes from  
2030 different depths. The intensity loss from deep regions is compensated in the time-gain control. The  
2031 programmable gain amplifier allows the overall pixel level to be instantly adjustable when imaging.  
2032 The anti-aliasing filter is a low-pass filter that cuts off the high-frequency component beyond the  
2033 Nyquist frequency to make unambiguous analog-to-digital sampling. The corner frequency of the  
2034 anti-aliasing filter is determined before each run according to the sampling rate. Blue dashed box:  
2035 Digital signal conditioning path. The 23-tap FIR filter is programmed based on the transducer's  
2036 center frequency and filters out signals with frequencies over four times of the central frequency.  
2037 The decimator decimates the signals by N times, where N depends on the central frequency and  
2038 sampling rate to lower the required bandwidth for data transmission. The 41-tap FIR bandpass  
2039 filter only allows data near the center frequency to pass, which refines the signals. Another  
2040 decimator downsamples the data stream according to the setting of the bandpass filter and  
2041 sampling rate to maximize the transmission efficiency. Finally, apodization is applied to the data  
2042 in each channel to fulfill the requirement for gradual aperture tapering. ACF: anisotropic  
2043 conductive film; ADC: analog digital converter; FPGA: field-programmable gate array; PCIe:  
2044 peripheral component interconnect express; FIR: finite impulse response; I/O: input/output.



2045 **Supplementary Fig. 34 | Configuration of a Mills cross array.** It includes a transmit array and  
 2046 a receive array. Transmit and receive beamforming applied by both arrays helps focus in the  
 2047 elevational direction. But the signal-to-noise ratio and the lateral resolution are limited in the  
 2048 reconstructed image due to the small effective aperture.

<b>Parameters</b> <b>Modality</b>	<b>Spatial resolution</b>	<b>Temporal resolution</b>	<b>Radioactivity</b>	<b>Invasiveness</b>	<b>Mapping</b>	<b>Citation</b>
Magnetic resonance imaging	1.6 mm	33.3 ms	No	No	3D	5
X-Ray computed tomography	0.3 mm	50 ms	Yes	No	3D	6
Single photon emission computed tomography	10 mm	37.5 ms	Yes	No	3D	7
Positron emission tomography	2 mm	2000 ms	Yes	No	3D	7
Optical voltage map	1 mm	0.25 ms	No	No	2D	8
Optical coherence tomography	0.001 mm	85 ms	No	No	3D	9
Ultrasonography	1 mm	< 1 ms	No	No	3D	10,11

2049 **Supplementary Table 1 | Summary of existing imaging methods for the heart.** Spatial  
2050 resolution, temporal resolution, radioactivity, invasiveness, and mapping capability are evaluation  
2051 parameters in this study. Comprehensive analysis of these parameters of cardiac imaging  
2052 technologies helps us understand standards of medical imaging technologies, which serve as  
2053 guidance for developing the wearable cardiac imager.

<b>Model</b>	<b>Bonding strength (kPa)</b>	<b>Reference</b>
Histoacryl	2	22
Tisseel	6	22
Bioglue	8	22
3M Electrically Conductive Adhesive Transfer Tape 9703	13	229
Coseal	18	22
3M Electrically Conductive Adhesive Transfer Tape 9712	20	230
3M Electrically Conductive Adhesive Transfer Tape 9713	22	231
3M Electrically Conductive Adhesive Transfer Tape 9719	27	232
3M EMI Copper Foil Shielding Tape 1181	27	233
3M 3313 Copper Foil Tape	228	234
Liquid metal electrode	236 kPa	This work
Pure SEBS	250 kPa	This work

2054 **Supplementary Table 2 | Comparison between the bonding strength of the liquid metal**  
2055 **electrode, pure SEBS, and commercial adhesives.** The bonding strength between the electrode  
2056 and the transducer element is stronger than many commercial adhesives, preventing the electrodes  
2057 from delamination under various deformations.

<b>Model type</b>	<b>Training paradigm</b>	<b>Input Image Resolution</b>	<b>Learning rate</b>	<b>Optimizer</b>	<b>Code availability</b>
<b>U-Net</b>	Supervised learning	$512 \times 512$	$10^{-3}$	Adam	235
<b>FCN-32</b>	Supervised learning	$512 \times 512$	$10^{-3}$	Adam	236
<b>FCN-8</b>	Supervised learning	$512 \times 512$	$10^{-3}$	Adam	237
<b>Attention-U-Net</b>	Supervised learning	$512 \times 512$	$10^{-5}$	Adam	238
<b>U-Net++</b>	Supervised learning	$512 \times 512$	$10^{-4}$	Adam	239
<b>FCN-8 VGG</b>	Supervised learning	$512 \times 512$	$10^{-3}$	Adam	240
<b>VGG-U-Net</b>	Supervised learning	$512 \times 512$	$10^{-3}$	Adam	241
<b>Resnet50-U-Net</b>	Supervised learning	$512 \times 512$	$10^{-3}$	Adam	242

2058 **Supplementary Table 3 | Model parameters and code availability.** Key parameters of all  
2059 implemented models include model type, training paradigm, input image resolution, learning rate,  
2060 optimizer, and code availability. The models' hyperparameters were carefully tuned and were  
2061 implemented based on readable, consistent, and well-structured open source code.



	<b>Static, commercial probe</b>	<b>Static, wearable patch</b>	<b>After exercise, wearable patch (without data augmentation)</b>	<b>After exercise, wearable patch (with data augmentation)</b>
<b>Size of labeled data</b>	221	201	2029	10145
<b>Size of unlabeled data</b>	279	299	3829	3829

2062 **Supplementary Table 4 | Sample sizes for all models.** All models were trained with all data  
2063 collected in static and after intensive exercise.

<b>Model Name</b>	<b>Mean Intersection over Union (static)</b>	<b>Mean Intersection over Union (after exercise)</b>
Attention-U-Net	0.77	0.64
U-Net++	0.78	0.65
Nas-U-Net	0.69	0.52
Resnet50-U-Net	0.91	0.84
FCN-8	0.92	0.85
FCN-8 VGG	0.91	0.83
U-Net	0.85	0.74
U-Net-mini	0.16	0.09
<b>FCN-32</b>	<b>0.93</b>	<b>0.87</b>

2064 **Supplementary Table 5 | Mean Intersection over Union among different models.** The table  
2065 displays each model's mean Intersection over Unions on a testing dataset when the subject is static  
2066 and after exercise. The evaluation of Intersection over Union is based on the comparison of a pair  
2067 of predicted image and ground truth image. Specifically, the Intersection over Union equals to the  
2068 number of pixels in the overlaid area of both images divided by the number of pixels in the  
2069 combined area of both images. Mean Intersection over Union is the average Intersection over  
2070 Union across all images in the testing dataset. The FCN-32 model has the highest mean Intersection  
2071 over Union among all models.  
2072

2073 **Supplementary Video 1. Cardiac long and short axis views imaged by an orthogonal array.**  
2074  
2075 **Supplementary Video 2. Cardiac apical four- and two- chamber views imaged by an**  
2076 **orthogonal array.**  
2077  
2078 **Supplementary Video 3. Continuous cardiac imaging during rest, exercise, and recovery.**  
2079  
2080 **Supplementary Video 4. Left ventricle segmentation results by FCN-32.**  
2081  
2082 **Supplementary Video 5. Imaging guided biopsy on a phantom by an orthogonal array.**  
2083

2084 **References**

- 2085 1 Levick, J. R. *An Introduction to Cardiovascular Physiology* (Butterworth-Heinemann,  
2086 1991).
- 2087 2 Yazdanyar, A. & Newman, A. B. The burden of cardiovascular disease in the elderly:  
2088 morbidity, mortality, and costs. *Clin. Geriatr. Med.* **25**, 563-577, vii (2009).
- 2089 3 Ouyang, D. *et al.* Video-based AI for beat-to-beat assessment of cardiac function. *Nature*  
2090 **580**, 252-256 (2020).
- 2091 4 Jozwiak, M., Monnet, X. & Teboul, J. L. Monitoring: from cardiac output monitoring to  
2092 echocardiography. *Curr. Opin. Crit. Care* **21**, 395-401 (2015).
- 2093 5 Frahm, J., Voit, D. & Uecker, M. Real-Time Magnetic Resonance Imaging: Radial  
2094 Gradient-Echo Sequences With Nonlinear Inverse Reconstruction. *Invest. Radiol.* **54**, 757-  
2095 766 (2019).
- 2096 6 Commandeur, F., Goeller, M. & Dey, D. Cardiac CT: Technological Advances in Hardware,  
2097 Software, and Machine Learning Applications. *Curr. Cardiovasc. Imaging Rep* **11**, 1-12  
2098 (2018).
- 2099 7 Angelidis, G. *et al.* SPECT and PET in ischemic heart failure. *Heart Fail. Rev.* **22**, 243-261  
2100 (2017).
- 2101 8 Efimov, I. R., Nikolski, V. P. & Salama, G. Optical imaging of the heart. *Circ. Res.* **95**, 21-  
2102 33 (2004).
- 2103 9 Gargesha, M., Jenkins, M. W., Wilson, D. L. & Rollins, A. M. High temporal resolution  
2104 OCT using image-based retrospective gating. *Opt. Express* **17**, 10786-10799 (2009).
- 2105 10 Wang, R. Y. *et al.* High-resolution image reconstruction for portable ultrasound imaging  
2106 devices. *Eurasip J. Adv. Sig. Pr.* **2019**, 1-12 (2019).
- 2107 11 Baribeau, Y. *et al.* Handheld Point-of-Care Ultrasound Probes: The New Generation of  
2108 POCUS. *J. Cardiothorac. Vasc. Anesth.* **34**, 3139-3145 (2020).
- 2109 12 Zimetbaum, P. J. & Josephson, M. E. Use of the electrocardiogram in acute myocardial  
2110 infarction. *N. Engl. J. Med.* **348**, 933-940 (2003).
- 2111 13 Alihanka, J., Vaahtoranta, K. & Saarikivi, I. A new method for long-term monitoring of the  
2112 ballistocardiogram, heart rate, and respiration. *Am. J. Physiol.* **240**, R384-392 (1981).
- 2113 14 García-González, M. A., Argelagós-Palau, A., Fernández-Chimeno, M. & Ramos-Castro,  
2114 J. in *Comput. Cardiol. 2013*. 461-464 (IEEE).
- 2115 15 Elgendi, M. On the analysis of fingertip photoplethysmogram signals. *Curr. Cardiol. Rev.*  
2116 **8**, 14-25 (2012).
- 2117 16 Isaacson, D., Mueller, J. L., Newell, J. C. & Siltanen, S. Imaging cardiac activity by the D-  
2118 bar method for electrical impedance tomography. *Physiol. Meas.* **27**, S43-50 (2006).
- 2119 17 Schiller, N. B. *et al.* Recommendations for quantitation of the left ventricle by two-  
2120 dimensional echocardiography. American Society of Echocardiography Committee on  
2121 Standards, Subcommittee on Quantitation of Two-Dimensional Echocardiograms. *J. Am.*  
2122 *Soc. Echocardiogr.* **2**, 358-367 (1989).

- 2123 18 Hu, H. *et al.* Stretchable ultrasonic transducer arrays for three-dimensional imaging on  
2124 complex surfaces. *Sci. Adv.* **4**, eaar3979 (2018).
- 2125 19 Wang, C. *et al.* Monitoring of the central blood pressure waveform via a conformal  
2126 ultrasonic device. *Nat. Biomed. Eng.* **2**, 687-695 (2018).
- 2127 20 Shung, K. K. *Diagnostic Ultrasound* 1-232 (CRC press, Boca Raton, 2005).
- 2128 21 Huang, Z. L. *et al.* Three-dimensional integrated stretchable electronics. *Nat. Electron.* **1**,  
2129 473-480 (2018).
- 2130 22 Wu, S. J., Yuk, H., Wu, J., Nabzdyk, C. S. & Zhao, X. A Multifunctional Origami Patch for  
2131 Minimally Invasive Tissue Sealing. *Adv. Mater.* **33**, e2007667 (2021).
- 2132 23 Wu, H., Shen, G. & Chen, Y. A radiation emission shielding method for high intensity focus  
2133 ultrasound probes. *Biomed. Mater. Eng.* **26 Suppl 1**, S959-966 (2015).
- 2134 24 Chen, Q. P. *et al.* Ultrasonic inspection of curved structures with a hemispherical-  
2135 omnidirectional ultrasonic probe via linear scan SAFT imaging. *Ndt. & E. International*  
2136 **129** (2022).
- 2137 25 Wang, C. *et al.* Bioadhesive ultrasound for long-term continuous imaging of diverse organs.  
2138 *Science* **377**, 517-523 (2022).
- 2139 26 Wang, C. *et al.* Continuous monitoring of deep-tissue haemodynamics with stretchable  
2140 ultrasonic phased arrays. *Nat. Biomed. Eng.* **5**, 749-758 (2021).
- 2141 27 Montaldo, G., Tanter, M., Bercoff, J., Benech, N. & Fink, M. Coherent plane-wave  
2142 compounding for very high frame rate ultrasonography and transient elastography. *IEEE*  
2143 *Trans Ultrason Ferroelectr Freq Control* **56**, 489-506 (2009).
- 2144 28 Ghavami, M., Ilkhechi, A. K. & Zemp, R. Flexible transparent CMUT arrays for  
2145 photoacoustic tomography. *Opt. Express* **30**, 15877-15894 (2022).
- 2146 29 Xiao, Y., Boily, M., Hashemi, H. S. & Rivaz, H. High-Dynamic-Range Ultrasound:  
2147 Application for Imaging Tendon Pathology. *Ultrasound Med. Biol.* **44**, 1525-1532 (2018).
- 2148 30 Zander, D. *et al.* Ultrasound Image Optimization ("Knobology"): B-Mode. *Ultrasound Int*  
2149 *Open* **6**, E14-E24 (2020).
- 2150 31 Kempfski, K. M., Graham, M. T., Gubbi, M. R., Palmer, T. & Lediju Bell, M. A. Application  
2151 of the generalized contrast-to-noise ratio to assess photoacoustic image quality. *Biomed*  
2152 *Opt Express* **11**, 3684-3698 (2020).
- 2153 32 Huang, X., Lediju Bell, M. A. & Ding, K. Deep Learning for Ultrasound Beamforming in  
2154 Flexible Array Transducer. *IEEE Trans. Med. Imaging* **40**, 3178-3189 (2021).
- 2155 33 Cerqueira, M. D. *et al.* Standardized myocardial segmentation and nomenclature for  
2156 tomographic imaging of the heart. A statement for healthcare professionals from the  
2157 Cardiac Imaging Committee of the Council on Clinical Cardiology of the American Heart  
2158 Association. *Circulation* **105**, 539-542 (2002).
- 2159 34 Feigenbaum, H. Role of M-mode technique in today's echocardiography. *J. Am. Soc.*  
2160 *Echocardiogr.* **23**, 240-257; 335-247 (2010).
- 2161 35 Devereux, R. B. *et al.* Standardization of M-mode echocardiographic left ventricular

2162 anatomic measurements. *J. Am. Coll. Cardiol.* **4**, 1222-1230 (1984).

2163 36 Armstrong, W. F., Pellikka, P. A., Ryan, T., Crouse, L. & Zoghbi, W. A. Stress  
2164 echocardiography: recommendations for performance and interpretation of stress  
2165 echocardiography. Stress Echocardiography Task Force of the Nomenclature and Standards  
2166 Committee of the American Society of Echocardiography. *J. Am. Soc. Echocardiogr.* **11**,  
2167 97-104 (1998).

2168 37 Rerych, S. K., Scholz, P. M., Newman, G. E., Sabiston, D. C., Jr. & Jones, R. H. Cardiac  
2169 function at rest and during exercise in normals and in patients with coronary heart disease:  
2170 evaluation by radionuclide angiocardiology. *Ann. Surg.* **187**, 449-464 (1978).

2171 38 Little, W. C. & Applegate, R. J. Congestive heart failure: systolic and diastolic function. *J.*  
2172 *Cardiothorac. Vasc. Anesth.* **7**, 2-5 (1993).

2173 39 Hill, J. & Timmis, A. Exercise tolerance testing. *BMJ* **324**, 1084-1087 (2002).

2174 40 Marwick, T. H. Stress echocardiography. *Echocardiography* 491-519 (2018).

2175 41 Hammermeister, K. E., Brooks, R. C. & Warbasse, J. R. The rate of change of left  
2176 ventricular volume in man. I. Validation and peak systolic ejection rate in health and disease.  
2177 *Circulation* **49**, 729-738 (1974).

2178 42 Pellikka, P. A. *et al.* Variability in Ejection Fraction Measured By Echocardiography, Gated  
2179 Single-Photon Emission Computed Tomography, and Cardiac Magnetic Resonance in  
2180 Patients With Coronary Artery Disease and Left Ventricular Dysfunction. *JAMA Netw*  
2181 *Open* **1**, e181456 (2018).

2182 43 Ghorbanzadeh, O. *et al.* Evaluation of Different Machine Learning Methods and Deep-  
2183 Learning Convolutional Neural Networks for Landslide Detection. *Remote Sensing* **11**, 196  
2184 (2019).

2185 44 Bland, J. M. & Altman, D. G. Statistical Methods for Assessing Agreement between Two  
2186 Methods of Clinical Measurement. *Lancet* **1**, 307-310 (1986).

2187 45 Matheijssen, N. A. *et al.* Assessment of left ventricular volume and mass by cine magnetic  
2188 resonance imaging in patients with anterior myocardial infarction intra-observer and inter-  
2189 observer variability on contour detection. *Int. J. Card. Imaging* **12**, 11-19 (1996).

2190 46 Fritzsche, R. G., Switzer, T. W., Hodgkinson, B. J. & Coyle, E. F. Stroke volume decline  
2191 during prolonged exercise is influenced by the increase in heart rate. *J Appl Physiol* **86**,  
2192 799-805 (1999).

2193 47 Pashaei, V. *et al.* Flexible Body-Conformal Ultrasound Patches for Image-Guided  
2194 Neuromodulation. *IEEE Trans Biomed Circuits Syst* **14**, 305-318 (2020).

2195 48 Kenny, J. S. *et al.* A novel, hands-free ultrasound patch for continuous monitoring of  
2196 quantitative Doppler in the carotid artery. *Sci. Rep.* **11**, 7780 (2021).

2197 49 Sung, F. *et al.* in *Proc. IEEE Comput. Soc. Conf. Comput. Vis. Pattern Recognit.* 1199-  
2198 1208.

2199 50 Kaelbling, L. P., Littman, M. L. & Moore, A. W. Reinforcement learning: A survey. *J. Artif.*  
2200 *Intell. Res.* **4**, 237-285 (1996).

- 2201 51 Lin, M. Y., Hu, H. J., Zhou, S. & Xu, S. Soft wearable devices for deep-tissue sensing. *Nat.*  
2202 *Rev. Mater.*, 1-20 (2022).
- 2203 52 Jeong, S. H. *et al.* Liquid alloy printing of microfluidic stretchable electronics. *Lab Chip*  
2204 **12**, 4657-4664 (2012).
- 2205 53 Kramer, R. K., Majidi, C. & Wood, R. J. Masked Deposition of Gallium-Indium Alloys for  
2206 Liquid-Embedded Elastomer Conductors. *Adv. Funct. Mater.* **23**, 5292-5296 (2013).
- 2207 54 Ladd, C., So, J. H., Muth, J. & Dickey, M. D. 3D printing of free standing liquid metal  
2208 microstructures. *Adv. Mater.* **25**, 5081-5085 (2013).
- 2209 55 Tabatabai, A., Fassler, A., Usiak, C. & Majidi, C. Liquid-phase gallium-indium alloy  
2210 electronics with microcontact printing. *Langmuir* **29**, 6194-6200 (2013).
- 2211 56 Cheng, S. & Wu, Z. Microfluidic electronics. *Lab Chip* **12**, 2782-2791 (2012).
- 2212 57 Sempionatto, J. R. *et al.* An epidermal patch for the simultaneous monitoring of  
2213 haemodynamic and metabolic biomarkers. *Nat. Biomed. Eng.* **5**, 737-748 (2021).
- 2214 58 Liu, S., Shah, D. S. & Kramer-Bottiglio, R. Highly stretchable multilayer electronic circuits  
2215 using biphasic gallium-indium. *Nat. Mater.* **20**, 851-858 (2021).
- 2216 59 Ma, Z. *et al.* Permeable superelastic liquid-metal fibre mat enables biocompatible and  
2217 monolithic stretchable electronics. *Nat. Mater.* **20**, 859-868 (2021).
- 2218 60 Lopes, P. A., Santos, B. C., de Almeida, A. T. & Tavakoli, M. Reversible polymer-gel  
2219 transition for ultra-stretchable chip-integrated circuits through self-soldering and self-  
2220 coating and self-healing. *Nat. Commun.* **12**, 4666 (2021).
- 2221 61 Mi, X. H., Qin, L., Liao, Q. W. & Wang, L. K. Electromechanical coupling coefficient and  
2222 acoustic impedance of 1-1-3 piezoelectric composites. *Ceram. Int.* **43**, 7374-7377 (2017).
- 2223 62 Wang, Z. *et al.* A flexible ultrasound transducer array with micro-machined bulk PZT.  
2224 *Sensors (Basel)* **15**, 2538-2547 (2015).
- 2225 63 Hong, C.-H. *et al.* Lead-free piezoceramics – Where to move on? *J. Materiomics* **2**, 1-24  
2226 (2016).
- 2227 64 Zhu, B. P. *et al.* Sol-gel derived PMN-PT thick films for high frequency ultrasound linear  
2228 array applications. *Ceram. Int.* **39**, 8709-8714 (2013).
- 2229 65 Li, X. *et al.* 80-MHz intravascular ultrasound transducer using PMN-PT free-standing film.  
2230 *IEEE Trans. Ultrason. Ferroelectr. Freq. Control* **58**, 2281-2288 (2011).
- 2231 66 Zhu, B. *et al.* Lift-off PMN-PT Thick Film for High Frequency Ultrasonic Biomicroscopy.  
2232 *J. Am. Ceram. Soc.* **93**, 2929-2931 (2010).
- 2233 67 Shahriari, S. & Garcia, D. Meshfree simulations of ultrasound vector flow imaging using  
2234 smoothed particle hydrodynamics. *Phys. Med. Biol.* **63**, 205011 (2018).
- 2235 68 Sun, X., Li, Y. & Liu, H. in *2017 8th International IEEE/EMBS Conference on NER* 122-  
2236 125 (IEEE).
- 2237 69 AlMohimeed, I., Turkistani, H. & Ono, Y. in *2013 IEEE Int. Ultrason. Symp.* 1137-1140  
2238 (IEEE).
- 2239 70 Bowen, C. R., Bradley, L. R., Almond, D. P. & Wilcox, P. D. Flexible piezoelectric

2240 transducer for ultrasonic inspection of non-planar components. *Ultrasonics* **48**, 367-375  
2241 (2008).

2242 71 Farus, L. Wearable ultrasound array for point-of-care imaging and patient monitoring.  
2243 *Medicine Meets Virtual Reality 22: NextMed/MMVR22* **220**, 241 (2016).

2244 72 Bhuyan, A. *et al.* in *2011 IEEE Int. Ultrason. Symp.* 1060-1063 (IEEE).

2245 73 Roy, K. *et al.* in *2020 IEEE Int. Ultrason. Symp.* 1-4 (IEEE).

2246 74 Kato, Y. *et al.* Large-Area Flexible Ultrasonic Imaging System With an Organic Transistor  
2247 Active Matrix. *T Electron Dev* **57**, 995-1002 (2010).

2248 75 Peng, C., Chen, M., Sim, H. K., Zhu, Y. & Jiang, X. in *2020 IEEE 15th International  
2249 Conference on NEMS*, 143-146 (IEEE).

2250 76 Wang, F. *et al.* Flexible Doppler ultrasound device for the monitoring of blood flow velocity.  
2251 *Sci. Adv.* **7**, eabi9283 (2021).

2252 77 Chen, J., Liu, W., Wu, D. & Ye, H. Laser Micromachined Flexible Ultrasound Line Array  
2253 and Subplanar Multimodal Imaging Applications. *IEEE Open Journal of Trans. Ultrason.  
2254 Ferroelectr. Freq. Control* **2**, 131-139 (2022).

2255 78 Safavi, K. C. *et al.* Variation exists in rates of admission to intensive care units for heart  
2256 failure patients across hospitals in the United States. *Circulation* **127**, 923-929 (2013).

2257 79 Dar, O. & Cowie, M. R. Acute heart failure in the intensive care unit: epidemiology. *Crit.  
2258 Care Med.* **36**, S3-8 (2008).

2259 80 de Mendonca, A. *et al.* Acute renal failure in the ICU: risk factors and outcome evaluated  
2260 by the SOFA score. *Intensive Care Med.* **26**, 915-921 (2000).

2261 81 Yildiz, M. *et al.* Left ventricular hypertrophy and hypertension. *Prog. Cardiovasc. Dis.* **63**,  
2262 10-21 (2020).

2263 82 Bhella, P. S. *et al.* Impact of lifelong exercise "dose" on left ventricular compliance and  
2264 distensibility. *J. Am. Coll. Cardiol.* **64**, 1257-1266 (2014).

2265 83 Moss, R. L. & Fitzsimons, D. P. **90** 11-13 (Am Heart Assoc, 2002).

2266 84 Allan, P. L. *Clinical Doppler Ultrasound* (Elsevier Health Sciences, 2006).

2267 85 Gennisson, J. L., Deffieux, T., Fink, M. & Tanter, M. Ultrasound elastography: principles  
2268 and techniques. *Diagn Interv Imaging* **94**, 487-495 (2013).

2269 86 Soepriatna, A. H., Damen, F. W., Vlachos, P. P. & Goergen, C. J. Cardiac and respiratory-  
2270 gated volumetric murine ultrasound. *Int. J. Cardiovasc. Imaging* **34**, 713-724 (2018).

2271 87 Bercoff, J. Ultrafast ultrasound imaging. *Ultrasound Medical*, 3-24 (2011).

2272 88 Christensen-Jeffries, K. *et al.* Super-resolution Ultrasound Imaging. *Ultrasound Med. Biol.*  
2273 **46**, 865-891 (2020).

2274 89 Cotero, V. *et al.* Noninvasive sub-organ ultrasound stimulation for targeted  
2275 neuromodulation. *Nat. Commun.* **10**, 952 (2019).

2276 90 Woudenberg, N. V. *et al.* in *Simulation, image processing, and ultrasound systems for  
2277 assisted diagnosis and navigation* 74-81 (Springer, 2018).

2278 91 Rothberg, J. M. *et al.* Ultrasound-on-chip platform for medical imaging, analysis, and



- 2279 collective intelligence. *Proc. Natl. Acad. Sci. U. S. A.* **118**, e2019339118 (2021).
- 2280 92 Hou, C. *et al.* Optimized Backing Layers Design for High Frequency Broad Bandwidth  
2281 Ultrasonic Transducer. *IEEE Trans. Biomed. Eng.* **69**, 475-481 (2022).
- 2282 93 Kim, H. *et al.* High-Attenuation Backing Layer for Miniaturized Ultrasound Imaging  
2283 Transducer. *IEEE Trans. Ultrason. Ferroelectr. Freq. Control* **69**, 1960-1969 (2022).
- 2284 94 Connors, A. F. The Effectiveness of Right Heart Catheterization in the Initial Care of  
2285 Critically III Patients. *JAMA*: **276**, 889-897 (1996).
- 2286 95 Darmon, P. L., Hillel, Z., Mogtader, A., Mindich, B. & Thys, D. Cardiac output by  
2287 transesophageal echocardiography using continuous-wave Doppler across the aortic valve.  
2288 *Anesthesiology* **80**, 796-805; discussion 725A (1994).
- 2289 96 Kanaya, N., Hirata, N., Kurosawa, S., Nakayama, M. & Namiki, A. Differential effects of  
2290 propofol and sevoflurane on heart rate variability. *Anesthesiology* **98**, 34-40 (2003).
- 2291 97 Enriquez, A. *et al.* Use of Intracardiac Echocardiography in Interventional Cardiology:  
2292 Working With the Anatomy Rather Than Fighting It. *Circulation* **137**, 2278-2294 (2018).
- 2293 98 Angelone, A. & Coulter, N. A., Jr. Respiratory Sinus Arrhythmia: A Frequency Dependent  
2294 Phenomenon. *J. Appl. Physiol.* **19**, 479-482 (1964).
- 2295 99 Nagga, K., Dong, H. J., Marcusson, J., Skoglund, S. O. & Wressle, E. Health-related factors  
2296 associated with hospitalization for old people: comparisons of elderly aged 85 in a  
2297 population cohort study. *Arch. Gerontol. Geriatr.* **54**, 391-397 (2012).
- 2298 100 Serdyuk, S. *et al.* Cardiac arrhythmias and sudden unexpected death in epilepsy: Results  
2299 of long-term monitoring. *Heart Rhythm* **18**, 221-228 (2021).
- 2300 101 Jelinek, M. V. & Lown, B. Exercise stress testing for exposure of cardiac arrhythmia. *Prog.*  
2301 *Cardiovasc. Dis.* **16**, 497-522 (1974).
- 2302 102 Vourvouri, E. C., Poldermans, D., Deckers, J. W., Parharidis, G. E. & Roelandt, J. R.  
2303 Evaluation of a hand carried cardiac ultrasound device in an outpatient cardiology clinic.  
2304 *Heart* **91**, 171-176 (2005).
- 2305 103 Nemati, E., Deen, M. J. & Mondal, T. A Wireless Wearable ECG Sensor for Long-Term  
2306 Applications. *IEEE Commun. Mag.* **50**, 36-43 (2012).
- 2307 104 Paradkar, N. & Chowdhury, S. R. in *2017 39th Annual International Conference of the*  
2308 *IEEE EMBC*, 113-116 (IEEE).
- 2309 105 Solosenko, A., Petrenas, A., Marozas, V. & Sornmo, L. Modeling of the  
2310 photoplethysmogram during atrial fibrillation. *Comput. Biol. Med.* **81**, 130-138 (2017).
- 2311 106 Lee, G., Sanders, P. & Kalman, J. M. Catheter ablation of atrial arrhythmias: state of the  
2312 art. *Lancet* **380**, 1509-1519 (2012).
- 2313 107 Lip, G. Y. & Hee, F. L. Paroxysmal atrial fibrillation. *QJM* **94**, 665-678 (2001).
- 2314 108 Kerr, C. R. *et al.* Progression to chronic atrial fibrillation after the initial diagnosis of  
2315 paroxysmal atrial fibrillation: results from the Canadian Registry of Atrial Fibrillation. *Am.*  
2316 *Heart J.* **149**, 489-496 (2005).
- 2317 109 Schor, S. S., Elsom, K. A., Elsom, K. O. & Dunn, J. P. An Evaluation of the Periodic Health

2318 Examination: A Study of Factors Discriminating between Survival and Death from  
2319 Coronary Heart Disease. *Ann. Intern. Med.* **61**, 1006-1014 (1964).

2320 110 Thygesen, K., Alpert, J. S., White, H. D. & Joint, E. S. C. A. A. H. A. W. H. F. T. F. f. t. R.  
2321 o. M. I. Universal definition of myocardial infarction. *J. Am. Coll. Cardiol.* **50**, 2173-2195  
2322 (2007).

2323 111 Xu, S. *et al.* Soft microfluidic assemblies of sensors, circuits, and radios for the skin.  
2324 *Science* **344**, 70-74 (2014).

2325 112 Alruwaili, F., Cluff, K., Griffith, J. & Farhoud, H. Passive Self Resonant Skin Patch Sensor  
2326 to Monitor Cardiac Intraventricular Stroke Volume Using Electromagnetic Properties of  
2327 Blood. *IEEE J. Transl. Eng. Health Med.* **6**, 1900709 (2018).

2328 113 Dagdeviren, C. *et al.* Conformal piezoelectric energy harvesting and storage from motions  
2329 of the heart, lung, and diaphragm. *Proc. Natl. Acad. Sci. U. S. A.* **111**, 1927-1932 (2014).

2330 114 Van den Oever, H. L., Murphy, E. J. & Christie-Taylor, G. A. USCOM (Ultrasonic Cardiac  
2331 Output Monitors) lacks agreement with thermodilution cardiac output and  
2332 transoesophageal echocardiography valve measurements. *Anaesth. Intensive Care* **35**, 903-  
2333 910 (2007).

2334 115 Edler, I. & Lindstrom, K. The history of echocardiography. *Ultrasound Med. Biol.* **30**,  
2335 1565-1644 (2004).

2336 116 Karamitsos, T. D., Francis, J. M., Myerson, S., Selvanayagam, J. B. & Neubauer, S. The  
2337 role of cardiovascular magnetic resonance imaging in heart failure. *J. Am. Coll. Cardiol.*  
2338 **54**, 1407-1424 (2009).

2339 117 Goo, H. W. *et al.* Computed tomography for the diagnosis of congenital heart disease in  
2340 pediatric and adult patients. *Int. J. Cardiovasc. Imaging* **21**, 347-365; discussion 367 (2005).

2341 118 Greenwood, J. P. *et al.* Cardiovascular magnetic resonance and single-photon emission  
2342 computed tomography for diagnosis of coronary heart disease (CE-MARC): a prospective  
2343 trial. *Lancet* **379**, 453-460 (2012).

2344 119 Machac, J. in *Seminars in nuclear medicine* 17-36 (Elsevier, 2005).

2345 120 Jenkins, M. W., Watanabe, M. & Rollins, A. M. Longitudinal Imaging of Heart  
2346 Development With Optical Coherence Tomography. *IEEE J. Sel. Top. Quantum Electron.*  
2347 **18**, 1166-1175 (2012).

2348 121 Coote, J. H. Recovery of heart rate following intense dynamic exercise. *Exp. Physiol.* **95**,  
2349 431-440 (2010).

2350 122 Simonson, E. *et al.* Cardiovascular Stress (Electrocardiographic Changes) Produced by  
2351 Driving an Automobile. *Am. Heart J.* **75**, 125 (1968).

2352 123 Sutherland, G. R. *et al.* Quantitation of left-ventricular asynergy by cardiac ultrasound. *Am.*  
2353 *J. Cardiol.* **86**, 4G-9G (2000).

2354 124 Berger, A. Magnetic resonance imaging. *BMJ* **324**, 35 (2002).

2355 125 Hamilton, J., Franson, D. & Seiberlich, N. Recent advances in parallel imaging for MRI.  
2356 *Prog. Nucl. Magn. Reson. Spectrosc.* **101**, 71-95 (2017).

- 2357 126 Garvey, C. J. & Hanlon, R. Computed tomography in clinical practice. *BMJ* **324**, 1077-  
2358 1080 (2002).
- 2359 127 Kalisz, K. *et al.* Artifacts at Cardiac CT: Physics and Solutions. *Radiographics* **36**, 2064-  
2360 2083 (2016).
- 2361 128 Khalil, M. M., Tremoleda, J. L., Bayomy, T. B. & Gsell, W. Molecular SPECT Imaging:  
2362 An Overview. *Int J Mol Imaging* **2011**, 796025 (2011).
- 2363 129 Cherry, S. R. & Dahlbom, M. *PET: Physics, Instrumentation, and Scanners*, 1-117  
2364 (Springer, 2006).
- 2365 130 Song, T. A., Chowdhury, S. R., Yang, F. & Dutta, J. Super-Resolution PET Imaging Using  
2366 Convolutional Neural Networks. *IEEE Trans Comput Imaging* **6**, 518-528 (2020).
- 2367 131 Guobao, W. High Temporal-Resolution Dynamic PET Image Reconstruction Using a New  
2368 Spatiotemporal Kernel Method. *IEEE Trans. Med. Imaging* **38**, 664-674 (2019).
- 2369 132 Chen, C. C., Shen, T. Y., Peterson, C. B., Hung, G. U. & Pan, T. Comparison of ejection  
2370 fraction calculation between CT and SPECT at high heart rate: A dynamic cardiac phantom  
2371 study. *J. Nucl. Cardiol.* **28**, 311-316 (2021).
- 2372 133 Newman, P. G. & Rozycki, G. S. The history of ultrasound. *Surg. Clin. North Am.* **78**, 179-  
2373 195 (1998).
- 2374 134 Carovac, A., Smajlovic, F. & Junuzovic, D. Application of ultrasound in medicine. *Acta*  
2375 *Inform. Med.* **19**, 168-171 (2011).
- 2376 135 Hasegawa, H. in *AIP Conf. Proc.* 020015 (AIP Publishing LLC).
- 2377 136 Williams, D. The physics of ultrasound. *Intensive Care* **13**, 264-268 (2012).
- 2378 137 Viessmann, O. M., Eckersley, R. J., Christensen-Jeffries, K., Tang, M. X. & Dunsby, C.  
2379 Acoustic super-resolution with ultrasound and microbubbles. *Phys. Med. Biol.* **58**, 6447-  
2380 6458 (2013).
- 2381 138 Joy, J., Cooke, I. & Love, M. Is ultrasound safe? *The Obstetrician & Gynaecologist* **8**, 222-  
2382 227 (2006).
- 2383 139 FDA, U. Marketing Clearance of diagnostic ultrasound systems and transducers—  
2384 guidance for Industry and Food and Drug Administration Staff. *Rockville, MD: FDA*  
2385 (2019).
- 2386 140 Stewart, P. A., Tonge, H. M. & Wladimiroff, J. W. Arrhythmia and structural abnormalities  
2387 of the fetal heart. *Br. Heart J.* **50**, 550-554 (1983).
- 2388 141 Dantas, R. G., Costa, E. T. & Leeman, S. Ultrasound speckle and equivalent scatterers.  
2389 *Ultrasonics* **43**, 405-420 (2005).
- 2390 142 Lanata, A., Scilingo, E. P., Francesconi, R., Varone, G. & De Rossi, D. in *2006 IEEE*  
2391 *Sensors*, 489-492 (IEEE).
- 2392 143 Smith, S. W., Pavy, H. R. & von Ramm, O. T. High-speed ultrasound volumetric imaging  
2393 system. I. Transducer design and beam steering. *IEEE Trans. Ultrason. Ferroelectr. Freq.*  
2394 *Control* **38**, 100-108 (1991).
- 2395 144 Yen, J. T. & Smith, S. W. Real-time rectilinear volumetric imaging. *IEEE Trans. Ultrason.*

- 2396 *Ferroelectr. Freq. Control* **49**, 114-124 (2002).
- 2397 145 Demore, C. E. M., Joyce, A. W., Wall, K. & Lockwood, G. R. Real-Time Volume Imaging  
2398 Using a Crossed Electrode Array. *Control* **56**, 1252-1261 (2009).
- 2399 146 Yen, J. T. Beamforming of sound from two-dimensional arrays using spatial matched filters.  
2400 *J. Acoust. Soc. Am.* **134**, 3697-3704 (2013).
- 2401 147 Kim, K.-S. & Song, T.-K. in *IEEE Ultrasonics Symposium, 2004*. 1409-1412 (IEEE).
- 2402 148 Fernandez, A. T. *et al.* Synthetic elevation beamforming and image acquisition capabilities  
2403 using an 8/spl times/128 1.75 D array. *IEEE Trans. Ultrason. Ferroelectr. Freq. Control*  
2404 **50**, 40-57 (2003).
- 2405 149 Yan, S., Guo, P. & Zhu, Q. in *Proceedings of the IEEE 27th* 61-62 (IEEE).
- 2406 150 Dahl, J. J., McAleavey, S. A., Pinton, G. F., Soo, M. S. & Trahey, G. E. Adaptive imaging  
2407 on a diagnostic ultrasound scanner at quasi real-time rates. *IEEE Trans. Ultrason.*  
2408 *Ferroelectr. Freq. Control* **53**, 1832-1843 (2006).
- 2409 151 Ferree, T. C., Luu, P., Russell, G. S. & Tucker, D. M. Scalp electrode impedance, infection  
2410 risk, and EEG data quality. *Clin. Neurophysiol.* **112**, 536-544 (2001).
- 2411 152 Sánchez, C. C., Glover, P., Power, H. & Bowtell, R. Calculation of the electric field  
2412 resulting from human body rotation in a magnetic field. *Phys. Med. Biol.* **57**, 4739 (2012).
- 2413 153 Stuchly, M. A. & Zhao, S. K. Magnetic field-induced currents in the human body in  
2414 proximity of power lines. *IEEE Trans. Power Delivery* **11**, 102-109 (1996).
- 2415 154 Mitchell, C. *et al.* Guidelines for Performing a Comprehensive Transthoracic  
2416 Echocardiographic Examination in Adults: Recommendations from the American Society  
2417 of Echocardiography. *J. Am. Soc. Echocardiogr.* **32**, 1-64 (2019).
- 2418 155 Uribarri, A., Bueno, H., Yotti, R. & Perez-David, E. Acute heart failure as presentation of  
2419 left-ACAOS. *Eur. Heart J.* **34**, 2787 (2013).
- 2420 156 Austeng, A., Nilsen, C.-I. C., Jensen, A. C., Næsholm, S. P. & Holm, S. in *2011 IEEE*  
2421 *International Ultrasonics Symposium* 2448-2451 (IEEE).
- 2422 157 Stanziola, A. *et al.* Motion Artifacts and Correction in Multipulse High-Frame Rate  
2423 Contrast-Enhanced Ultrasound. *IEEE Trans. Ultrason. Ferroelectr. Freq. Control* **66**, 417-  
2424 420 (2019).
- 2425 158 Prabhu, S. J., Kanal, K., Bhargava, P., Vaidya, S. & Dighe, M. K. Ultrasound artifacts:  
2426 classification, applied physics with illustrations, and imaging appearances. *Ultrasound Q*  
2427 **30**, 145-157 (2014).
- 2428 159 Kallel, F., Bertrand, M. & Meunier, J. Speckle Motion Artifact under Tissue Rotation.  
2429 *Control* **41**, 105-122 (1994).
- 2430 160 Kirberger, R. M. Imaging Artifacts in Diagnostic Ultrasound - a Review. *Vet. Radiol.*  
2431 *Ultrasound* **36**, 297-306 (1995).
- 2432 161 Cattermole, G. N. *et al.* The normal ranges of cardiovascular parameters measured using  
2433 the ultrasonic cardiac output monitor. *Physiol Rep* **5**, e13195 (2017).
- 2434 162 Nagel, E. *et al.* Noninvasive diagnosis of ischemia-induced wall motion abnormalities with

- 2435 the use of high-dose dobutamine stress MRI: comparison with dobutamine stress  
 2436 echocardiography. *Circulation* **99**, 763-770 (1999).
- 2437 163 Picano, E., Pibarot, P., Lancellotti, P., Monin, J. L. & Bonow, R. O. The emerging role of  
 2438 exercise testing and stress echocardiography in valvular heart disease. *J. Am. Coll. Cardiol.*  
 2439 **54**, 2251-2260 (2009).
- 2440 164 Argiento, P. *et al.* Exercise stress echocardiography for the study of the pulmonary  
 2441 circulation. *Eur. Respir. J.* **35**, 1273-1278 (2010).
- 2442 165 Lang, R. M. *et al.* Recommendations for cardiac chamber quantification by  
 2443 echocardiography in adults: an update from the American Society of Echocardiography  
 2444 and the European Association of Cardiovascular Imaging. *J. Am. Soc. Echocardiogr.* **28**, 1-  
 2445 39 e14 (2015).
- 2446 166 Koh, A. S. *et al.* A comprehensive population-based characterization of heart failure with  
 2447 mid-range ejection fraction. *Eur. J. Heart Fail.* **19**, 1624-1634 (2017).
- 2448 167 Kim, Y. S., Park, M. J., Rhim, H., Lee, M. W. & Lim, H. K. Sonographic analysis of the  
 2449 intercostal spaces for the application of high-intensity focused ultrasound therapy to the  
 2450 liver. *AJR Am. J. Roentgenol.* **203**, 201-208 (2014).
- 2451 168 Turakhia, M. P., McManus, D. D., Whooley, M. A. & Schiller, N. B. Increase in end-  
 2452 systolic volume after exercise independently predicts mortality in patients with coronary  
 2453 heart disease: data from the Heart and Soul Study. *Eur. Heart J.* **30**, 2478-2484 (2009).
- 2454 169 Jordan, J. H. *et al.* Early Myocardial Strain Changes During Potentially Cardiotoxic  
 2455 Chemotherapy May Occur as a Result of Reductions in Left Ventricular End-Diastolic  
 2456 Volume: The Need to Interpret Left Ventricular Strain With Volumes. *Circulation* **135**,  
 2457 2575-2577 (2017).
- 2458 170 Lock, J. E., Block, P. C., McKay, R. G., Baim, D. S. & Keane, J. F. Transcatheter closure  
 2459 of ventricular septal defects. *Circulation* **78**, 361-368 (1988).
- 2460 171 Stout, K. K. & Verrier, E. D. Acute valvular regurgitation. *Circulation* **119**, 3232-3241  
 2461 (2009).
- 2462 172 Cafarelli, A., Miloro, P., Verbeni, A., Carbone, M. & Menciassi, A. Speed of sound in  
 2463 rubber-based materials for ultrasonic phantoms. *J. Ultrasound* **19**, 251-256 (2016).
- 2464 173 Waters, K. R., Hughes, M. S., Mobley, J., Brandenburger, G. H. & Miller, J. G. On the  
 2465 applicability of Kramers-Kronig relations for ultrasonic attenuation obeying a frequency  
 2466 power law. *J. Acoust. Soc. Am.* **108**, 556-563 (2000).
- 2467 174 [http://www.factor2.com/v/vspfiles/msds\\_2015/a-4717tech%20F2.pdf](http://www.factor2.com/v/vspfiles/msds_2015/a-4717tech%20F2.pdf)
- 2468 175 McDonagh, T. A. *et al.* Corrigendum to: 2021 ESC Guidelines for the diagnosis and  
 2469 treatment of acute and chronic heart failure: Developed by the Task Force for the diagnosis  
 2470 and treatment of acute and chronic heart failure of the European Society of Cardiology  
 2471 (ESC) With the special contribution of the Heart Failure Association (HFA) of the ESC.  
 2472 *Eur. Heart J.* **42**, 4901 (2021).
- 2473 176 Konstam, M. A. & Abboud, F. M. Ejection Fraction: Misunderstood and Overrated

2474 (Changing the Paradigm in Categorizing Heart Failure). *Circulation* **135**, 717-719 (2017).  
 2475 177 Bosch, X. & Theroux, P. Left ventricular ejection fraction to predict early mortality in  
 2476 patients with non-ST-segment elevation acute coronary syndromes. *Am. Heart J.* **150**, 215-  
 2477 220 (2005).  
 2478 178 Curtis, J. P. *et al.* The association of left ventricular ejection fraction, mortality, and cause  
 2479 of death in stable outpatients with heart failure. *J. Am. Coll. Cardiol.* **42**, 736-742 (2003).  
 2480 179 Vincent, J. L. Understanding cardiac output. *Crit. Care* **12**, 174 (2008).  
 2481 180 Ehlers, K. C., Mylrea, K. C., Waterson, C. K. & Calkins, J. M. Cardiac output  
 2482 measurements. A review of current techniques and research. *Ann. Biomed. Eng.* **14**, 219-  
 2483 239 (1986).  
 2484 181 Jakovljevic, D. G., Trenell, M. I. & MacGowan, G. A. Bioimpedance and bioactance  
 2485 methods for monitoring cardiac output. *Best Pract. Res. Clin. Anaesthesiol.* **28**, 381-394  
 2486 (2014).  
 2487 182 Marik, P. E. Noninvasive cardiac output monitors: a state-of-the-art review. *J. Cardiothorac.*  
 2488 *Vasc. Anesth.* **27**, 121-134 (2013).  
 2489 183 Juncos, L. I. & Juncos, L. A. in *Clinical Decisions in Nephrology, Hypertension and Kidney*  
 2490 *Transplantation* Chapter 18, 175-182 (Springer, 2013).  
 2491 184 Kakihana, Y., Ito, T., Nakahara, M., Yamaguchi, K. & Yasuda, T. Sepsis-induced  
 2492 myocardial dysfunction: pathophysiology and management. *J Intensive Care* **4**, 22 (2016).  
 2493 185 Degroot, W. J. & Leonard, J. J. Hyperthyroidism as a High Cardiac Output State. *Am. Heart*  
 2494 *J.* **79**, 265-& (1970).  
 2495 186 Fowler, N. O. & Holmes, J. C. Blood viscosity and cardiac output in acute experimental  
 2496 anemia. *J. Appl. Physiol.* **39**, 453-456 (1975).  
 2497 187 Bamira, D. & Picard, M. in *Encyclopedia of Cardiovascular Research and Medicine* 35-  
 2498 45 (Elsevier, 2018).  
 2499 188 Devereux, R. B. *et al.* Congestive heart failure despite normal left ventricular systolic  
 2500 function in a population-based sample: the Strong Heart Study. *Am. J. Cardiol.* **86**, 1090-  
 2501 1096 (2000).  
 2502 189 Villari, B. *et al.* Influence of collagen network on left ventricular systolic and diastolic  
 2503 function in aortic valve disease. *J. Am. Coll. Cardiol.* **22**, 1477-1484 (1993).  
 2504 190 Borlaug, B. A. & Redfield, M. M. Diastolic and systolic heart failure are distinct  
 2505 phenotypes within the heart failure spectrum. *Circulation* **123**, 2006-2013; discussion 2014  
 2506 (2011).  
 2507 191 Little, R. C. & Little, W. C. Cardiac preload, afterload, and heart failure. *Arch. Intern. Med.*  
 2508 **142**, 819-822 (1982).  
 2509 192 Critchley, L. A., Lee, A. & Ho, A. M. A critical review of the ability of continuous cardiac  
 2510 output monitors to measure trends in cardiac output. *Anesth. Analg.* **111**, 1180-1192 (2010).  
 2511 193 Wesseling, K. H., Jansen, J. R., Settels, J. J. & Schreuder, J. J. Computation of aortic flow  
 2512 from pressure in humans using a nonlinear, three-element model. *J. Appl. Physiol.* (1985)

2513 74, 2566-2573 (1993).

2514 194 Reuter, D. A. *et al.* Usefulness of left ventricular stroke volume variation to assess fluid  
2515 responsiveness in patients with reduced cardiac function. *Crit. Care Med.* **31**, 1399-1404  
2516 (2003).

2517 195 Jhanji, S., Dawson, J. & Pearse, R. M. Cardiac output monitoring: basic science and clinical  
2518 application. *Anaesthesia* **63**, 172-181 (2008).

2519 196 Piculjan, A., Sustic, M., Brumini, G., Kuharic, J. & Sustic, A. Reliability of B-line  
2520 quantification by different-level observers and a software algorithm using point-of-care  
2521 lung ultrasound. *J. Clin. Monit. Comput.* **34**, 1259-1264 (2020).

2522 197 Huang, Q., Lan, J. & Li, X. Robotic Arm Based Automatic Ultrasound Scanning for Three-  
2523 Dimensional Imaging. *IEEE Trans. Ind. Inf.* **15**, 1173-1182 (2019).

2524 198 Argueta, E. E. & Paniagua, D. Thermodilution Cardiac Output: A Concept Over 250 Years  
2525 in the Making. *Cardiol. Rev.* **27**, 138-144 (2019).

2526 199 Bottiger, B. W. *et al.* Continuous versus intermittent thermodilution cardiac output  
2527 measurement during orthotopic liver transplantation. *Anaesthesia* **52**, 207-214 (1997).

2528 200 Norris, S. L., King, E. G., Grace, M. & Weir, B. Thermodilution cardiac output--an in vitro  
2529 model of low flow states. *Crit. Care Med.* **14**, 57-59 (1986).

2530 201 Baan, J. *et al.* Continuous stroke volume and cardiac output from intra-ventricular  
2531 dimensions obtained with impedance catheter. *Cardiovasc. Res.* **15**, 328-334 (1981).

2532 202 Rumberger, J. A. *et al.* in *Mayo Clin. Proc.* 860-870 (Elsevier, 1999).

2533 203 Timmins, A. C., Giles, M., Nathan, A. W. & Hinds, C. J. Clinical validation of a  
2534 radionuclide detector to measure ejection fraction in critically ill patients. *Br. J. Anaesth.*  
2535 **72**, 523-528 (1994).

2536 204 Swamy, G., Kuiper, J., Gudur, M. S., Olivier, N. B. & Mukkamala, R. Continuous left  
2537 ventricular ejection fraction monitoring by aortic pressure waveform analysis. *Ann. Biomed.*  
2538 *Eng.* **37**, 1055-1068 (2009).

2539 205 Critchley, L. A. & Critchley, J. A. A meta-analysis of studies using bias and precision  
2540 statistics to compare cardiac output measurement techniques. *J. Clin. Monit. Comput.* **15**,  
2541 85-91 (1999).

2542 206 Lester, S. J., Ryan, E. W., Schiller, N. B. & Foster, E. Best method in clinical practice and  
2543 in research studies to determine left atrial size. *Am. J. Cardiol.* **84**, 829-832 (1999).

2544 207 Giustiniano, E., Padua, E., Negri, K., Bragato, R. M. & Cecconi, M. Echocardiography  
2545 during Prone-Position Mechanical Ventilation in Patients with COVID-19: A Proposal for  
2546 a New Approach. *J. Am. Soc. Echocardiogr.* **33**, 905-906 (2020).

2547 208 Harris, M. & Chung, F. Complications of general anesthesia. *Clin. Plast. Surg.* **40**, 503-513  
2548 (2013).

2549 209 Devereaux, P. J. *et al.* Characteristics and short-term prognosis of perioperative myocardial  
2550 infarction in patients undergoing noncardiac surgery: a cohort study. *Ann. Intern. Med.* **154**,  
2551 523-528 (2011).

2552 210 Priebe, H. J. Preoperative cardiac management of the patient for non-cardiac surgery: an  
2553 individualized and evidence-based approach. *Br. J. Anaesth.* **107**, 83-96 (2011).

2554 211 McLeod, G. *et al.* Echocardiography in Congenital Heart Disease. *Prog. Cardiovasc. Dis.*  
2555 **61**, 468-475 (2018).

2556 212 Smith, C. D., Weber, C. J. & Amerson, J. R. Laparoscopic adrenalectomy: new gold  
2557 standard. *World J. Surg.* **23**, 389-396 (1999).

2558 213 Ronneberger, O., Fischer, P. & Brox, T. in *Medical Image Computing and Computer-*  
2559 *Assisted Intervention – MICCAI 2015*, 234-241 (Springer, 2015).

2560 214 Long, J., Shelhamer, E. & Darrell, T. in *Proceedings of the IEEE conference on CVPR*  
2561 3431-3440 (2015).

2562 215 Oktay, O. *et al.* Attention u-net: Learning where to look for the pancreas. *arXiv preprint*  
2563 *arXiv:1804.03999* (2018).

2564 216 Zhou, Z., Rahman Siddiquee, M. M., Tajbakhsh, N. & Liang, J. in *Deep Learning in*  
2565 *Medical Image Analysis and Multimodal Learning for Clinical Decision Support* 3-11  
2566 (Springer, 2018).

2567 217 Weng, Y., Zhou, T. B., Li, Y. J. & Qiu, X. Y. NAS-Unet: Neural Architecture Search for  
2568 Medical Image Segmentation. *IEEE Access* **7**, 44247-44257 (2019).

2569 218 Al-Haija, Q. A. & Adebajo, A. in *2020 IEEE International IOT, IEMTRONICS* 1-7 (IEEE).

2570 219 Mao, Y. X. *et al.* Efficient Low-Cost Ship Detection for SAR Imagery Based on Simplified  
2571 U-Net. *IEEE Access* **8**, 69742-69753 (2020).

2572 220 Wahr, D. W., Wang, Y. S. & Schiller, N. B. Left ventricular volumes determined by two-  
2573 dimensional echocardiography in a normal adult population. *J. Am. Coll. Cardiol.* **1**, 863-  
2574 868 (1983).

2575 221 Rezatofghi, H. *et al.* in *Proceedings of the IEEE/CVF conference on CVPR* 658-666 (2019).

2576 222 Smistad, E. & Østvik, A. in *2017 IEEE Int. Ultrason. Symp.* 1-4 (IEEE).

2577 223 Leclerc, S. *et al.* Deep Learning for Segmentation Using an Open Large-Scale Dataset in  
2578 2D Echocardiography. *IEEE Trans. Med. Imaging* **38**, 2198-2210 (2019).

2579 224 Chen, C. *et al.* Deep Learning for Cardiac Image Segmentation: A Review. *Front.*  
2580 *Cardiovasc. Med.* **7**, 25 (2020).

2581 225 Yamashita, R., Nishio, M., Do, R. K. G. & Togashi, K. Convolutional neural networks: an  
2582 overview and application in radiology. *Insights into Imaging* **9**, 611-629 (2018).

2583 226 Zhou, S. K., Le, H. N., Luu, K., H, V. N. & Ayache, N. Deep reinforcement learning in  
2584 medical imaging: A literature review. *Med. Image Anal.* **73**, 102193 (2021).

2585 227 Sun, L. *et al.* Few-shot medical image segmentation using a global correlation network  
2586 with discriminative embedding. *Comput. Biol. Med.* **140**, 105067 (2022).

2587 228 Shattuck, D. P., Weinshenker, M. D., Smith, S. W. & von Ramm, O. T. Explososcan: a  
2588 parallel processing technique for high speed ultrasound imaging with linear phased arrays.  
2589 *J. Acoust. Soc. Am.* **75**, 1273-1282 (1984).

2590 229 <https://multimedia.3m.com/mws/media/662350/3m-electrically-conductive-adhesive->



2591 [transfer-tape-9703.pdf](#)  
2592 230 [https://www.3m.com/3M/en\\_US/p/d/b00036780/](https://www.3m.com/3M/en_US/p/d/b00036780/)  
2593 231 <https://multimedia.3m.com/mws/media/661270/3m-xyz-axis-electrically-conductive-tape-9713.pdf>  
2594  
2595 232 [https://www.3m.com/3M/en\\_US/p/d/b10179639/](https://www.3m.com/3M/en_US/p/d/b10179639/)  
2596 233 <https://multimedia.3m.com/mws/media/373700/3m-emi-copper-foil-shielding-tape-1181-data-sheet-78-8127-9953-0-b.pdf>  
2597  
2598 234 [https://www.3m.com/3M/en\\_US/p/d/b40067945/](https://www.3m.com/3M/en_US/p/d/b40067945/)  
2599 235 <https://github.com/divamgupta/image-segmentation-keras>  
2600 236 <https://github.com/divamgupta/image-segmentation-keras>  
2601 237 <https://github.com/divamgupta/image-segmentation-keras>  
2602 238 [https://github.com/LeeJunHyun/Image\\_Segmentation](https://github.com/LeeJunHyun/Image_Segmentation)  
2603 239 <https://github.com/MrGiovanni/UNetPlusPlus>  
2604 240 <https://github.com/divamgupta/image-segmentation-keras>  
2605 241 <https://github.com/divamgupta/image-segmentation-keras>  
2606 242 <https://github.com/divamgupta/image-segmentation-keras>  
2607